Methodology for Pyrolysis-induced Thermal Runaway Analysis in Li-ion Batteries

by

Mahmoud M. Ramadan

B.S., Chemical Engineering
Ohio University (2020)

Submitted to the Department of Mechanical Engineering and
Institute for Data, Systems, and Society
in partial fulfillment of the requirements for the degrees of

Master of Science in Mechanical Engineering

and

Master of Science in Technology and Policy

at the

MASSACHUSETTS INSTITUTE OF TECHNOLOGY

September 2023

Authored by: Mahmoud M. Ramadan
Department of Mechanical Engineering and
Institute for Data, Systems, and Society
August 4, 2023

Certified by: Ahmed F. Ghoniem
Ronald C. Crane (1972) Professor of Mechanical Engineering
Thesis Supervisor

Certified by: Elsa Olivetti
Professor of Materials Science and Engineering
Thesis Supervisor

Accepted by: Nicolas Hadjiconstantinou
Professor of Mechanical Engineering
Graduate Officer, Department of Mechanical Engineering

Accepted by: Frank R. Field III
Senior Research Engineer, Sociotechnical Systems Research Center
Interim Director, Technology and Policy Program

Methodology for Pyrolysis-induced Thermal Runaway Analysis in Li-ion Batteries

by

Mahmoud M. Ramadan

Submitted to the Department of Mechanical Engineering
and
Institute for Data, Systems, and Society
on August 4, 2023, in partial fulfillment of the
requirements for the degrees of
Master of Science in Mechanical Engineering
and
Master of Science in Technology and Policy

Abstract

As the adoption of lithium-ion batteries (LIBs) grows due to the demand for high-energy density storage solutions, ensuring their safety becomes paramount. Thermogravimetric Analysis (TGA) and Differential Scanning Calorimetry (DSC), which have traditionally been tools in polymer thermal analysis since the 1950s, have seen increasing use in LIB thermal research in recent decades. However, applying these techniques to LIBs poses challenges due to the multifaceted composition of LIBs and its sensitivity to environmental conditions. This research aims to overcome the inherent limitations of TGA and DSC when applied to LIBs by introducing a robust, standardized experimental protocol to ensure accuracy and consistency. Employing TGA and DSC concurrently and using sealed crucibles with pinholes, we present a comprehensive thermal profile of next-generation LiFSI-based electrolytes, revealing behaviors that differ based on solvent choice. Our analysis discerned distinct thermal properties between LiFSI-carbonate and LiFSI-ether electrolytes. Specifically, carbonate-based electrolytes displayed a pronounced exothermic peak at 350°C, indicative of significant decomposition reactions. In contrast, the LiFSI-ether electrolyte exhibited an exothermic reaction at 210°C, followed by an endothermic event near 300°C. Such variances in thermal behavior emphasize the profound influence of solvent selection on the thermal profiles of electrolyte solutions. A techno-economic assesment on sodium-ion batteries is also presented.

Thesis Supervisor: Ahmed F. Ghoniem
Title: Ronald C. Crane (1972) Professor of Mechanical Engineering

Thesis Supervisor: Elsa Olivetti
Title: Professor of Materials Science and Engineering

Acknowledgments

First and foremost, I would like to thank my advisor Prof. Ahmed Ghoneim for being a great mentor and for his unwavering support and invaluable guidance. Prof. Ghoneim's patience, flexibility, and support for my decisions have been instrumental in shaping my interdisciplinary approach to learning, and for that, I am forever grateful. I consider myself incredibly privileged to have had such an exceptional advisor by my side.

As my TPP advisor, Prof. Elsa Olivetti provided exceptional guidance in the techno-economic modeling portion of my thesis. I would like to thank her and Dr. Kevin Huang for their support.

Prof. Betar Gallant and her group have been very instrumental in facilitating the sample fabrication process that was used in the thermal behavior portion of the thesis.

I am incredibly lucky to have supportive and great friends, both at MIT and beyond. Thank you Majed Almubarak, Salem Ghurab, Dr. Monica Burdick, and Dr. Alyssa Bernstein.

I am immensely grateful to Chaplain Nada El-Alami for her spiritual guidance, compassion, and wisdom, which have left a lasting impact on my life, providing solace, strength, and a greater understanding of my own journey.

To my beloved family, my parents, Hayfa and Mohamad,and my sister, Rend, I am eternally grateful for your endless love and support, as well as the countless sacrifices you have made. I also wish to express deep gratitude to my late grandfather Faouzi Saad. He has been my source of inspiration through his exceptional dedication to public service. He has shown me the enduring value of contributing to society and the lasting impact it can make. His legacy of public service continues to motivate me and guide my aspirations.

I thank God for all His blessings.

Contents

List of Figures

List of Tables

Chapter 1

Introduction

1.1 Motivation

As the demand for high-energy density batteries continues to increase and as LIBs become more widespread, greater safety concerns have to be addressed by characterizing and understanding the nature of LIB failures, and engineering solutions to mitigate the problems.

The major limitation to the implementation of higher energy density batteries is safety. The major safety concern in lithium-based batteries is thermal runaway-caused fire and explosion. Greater safety concerns have to be addressed by characterizing and understanding the nature of lithium-based batteries failures more than just from a phenomenological level. In severe cases, localized heating in the cell can initiate thermal runaway followed by the decomposition of some cell components; thereby, releasing hydrocarbons and possibly oxygen that have the propensity to combust, leading to difficult-to-control or distinguish fires.

Thermogravimetric Analysis (TGA) and Differential Scanning Calorimetry (DSC) are techniques that have been traditionally and extensively used in polymer thermal analysis, dating back to the early 1950s. TGA is often used to determine the thermal stability of polymers, their decomposition temperatures, and the amount of filler content. It operates by continuously measuring the mass of a sample as it is heated over time, which allows the determination of the temperatures at which the polymer

undergoes thermal degradation and other weight loss events. DSC measures the heat flow into or out of a sample as it is heated, cooled, or held at constant temperature. It provides insights into the thermal transitions of a polymer, such as transition, melting, and crystallization temperatures and heat capacities.

In the past two decades, the TGA and DSC have started becoming employed in lithium-ion battery (LIB) thermal research. In some instances, researchers in the LIB community have employed TGA and DSC techniques without adequately addressing the limitations, assumptions, or specific considerations inherent in these analysis protocols when applied to LIBs. Given the complexity of LIBs, comprising multiple components with distinct thermal properties, TGA and DSC results can be challenging to interpret accurately. A crucial limiting factor is the sensitivity of LIB materials to air and moisture. LIB sample exposure to air or moisture can cause oxidation reactions or reactions with water that lead to the formation of other compounds and change the thermal properties of the materials being analyzed. Unlike polymers, which are often single-component systems, LIBs are composed of several distinct materials (the cathode, anode, separator, electrolyte, and possibly other additives). Each of these has its own set of thermal properties, and their interactions can make the analysis more complex. The thermal events observed in TGA and DSC can be due to one or more of these components, or their interactions, making the results harder to deconvolute.

Stringent measures must be in place when employing TGA and DSC for LIB analysis, underscoring the need for appropriate handling, procedural adherence, and equipment maintenance. Given that the TGA and DSC were originally designed and developed in the context of polymer analysis — which primarily involves phase changes and not vigorous reactions—it is also crucial to stress the importance of the aforementioned considerations when these techniques are applied to LIB samples. It is essential to fully understand and clearly state the assumptions made, limitations encountered, and the rigorousness of the experimental protocols followed. Additionally, critical evaluation of the results, considering the complex nature of LIBs, is paramount to avoid misleading conclusions.

1.2 Objective

The objective of this research is to investigate the inherent limitations and challenges associated with applying TGA and DSC techniques to the study of the thermal behavior of LIBs. As a part of this investigation, we intend to identify the key areas where these techniques may fall short or lead to misleading conclusions when used for LIB thermal analysis. This will involve a review of existing literature on the thermal behavior of LIB components, along with systematic experimental studies to understand the nuances and implications of applying TGA and DSC to LIBs.

The second facet of this research is aimed at developing a robust, standardized, and reproducible experimental protocol for conducting TGA and DSC analyses on LIBs. This protocol will incorporate stringent controls to protect against the potential pitfalls identified in the investigation. It will also provide clear guidelines for sample preparation, instrument calibration, data acquisition, and interpretation of results. In doing so, we aim to enhance the quality of data derived from these techniques and ensure their reliability when used in the context of LIB thermal analysis. This approach will, ultimately, contribute to a deeper understanding of LIBs, aiding the design of safer, more efficient batteries and facilitating the advancement of energy storage technologies.

Chapter 2

Background

LIBs are a class of rechargeable batteries that have been widely used in consumer electronics. LIBs were first commercialized by Sony in 1991 for use in camera devices and have become popular ever since. Lithium being the lightest metal make LIBs one of the highest-energy-density rechargeable batteries. LIBs are key candidates in the large-scale transition from traditional internal-combustion engine (ICE)-based vehicles to electric vehicles (EVs) and for energy storage applications for intermittent energy.

The main difference between an EV and a gasoline vehicle is the LIB which is the heart of the EV. The price of LIB has been dropping continuously for the past few decades from over $8,000/kWh in 1992, to $1,100/kWh in 2010, to $140/kWh today[71] (Figure 2-1). In order to achieve cost competitiveness with gasoline vehicles, the average price of an EV battery pack must decrease to $100/kWh[54]. Recent studies predict that the U.S. can achieve this decrease by 2024-2026 using existing battery chemistries[55]. With price parity projected to occur in the next 2-4 years, the increase in availability of second-hand EVs, and the advantage of economies of scale, the price of EVs is inevitably going to compete with gasoline vehicles.

As the demand for LIBs continues to increase, the importance of their safe use, reuse, and recycling becomes paramount. These batteries are energy dense, capable of storing around 200 Wh/kg, and are composed of highly reactive electrodes and flammable organic-based electrolytes. The interaction between the battery's compo-

nents, particularly the anode, cathode, and electrolyte, is exothermic. When subject to disruptions, including overcharging, mechanical damage, or short-circuiting, these batteries are at risk of thermal runaway. This process begins with the onset of heating from factors like overcharging or internal short circuits. As temperatures rise, the Solid Electrolyte Interface decomposes, initiating exothermic reactions. Once the heat produced outpaces the battery's ability to dissipate it, thermal runaway begins to occur.

The frequency of LIB failures remains relatively low; nonetheless, incidents involving LIBs, especially during transportation, highlight their potential risks. Factors leading to LIB thermal runaway are generally classified into mechanical failures, electrical failures, or thermal abuse, with internal short circuits being a predominant cause. For safe operation and longevity, understanding the mechanisms of thermal runaway and the interactions between the LIB components at elevated temperatures is essential.

2.1 Principle Behind LIB

The main principle behind the rechargeable nature of LIBs is the reversible lithium-ion (Li^+) transport during charging and discharging. Electrode materials should have the ability to intercalate Li^+ (store Li^+ between its layers). During charging, Li^+ travels from the cathode and are intercalated into the anode; when discharging, Li^+ de-intercalates from the anode and transfers into the cathode (see Figure 2-2). LIBs are typically composed of graphite anodes and transition metal oxide cathodes, both of which have the ability to intercalate Li^+. Ideally, the electrolyte should be ionically conductive of Li^+ and chemically inert towards the electrodes.

The majority of commercial LIBs use carbon graphite as the active material for the anode and a lithium transition-metal oxide for the cathode. The major difference between a LIB and lithium-metal battery (LMB) is the use of a piece of lithium metal at the anode in LMBs, which increases energy density. The three main classes for the lithium-transition metal oxides are layered ($LiMO_2$), spinel (LiM_2O_4), and complex

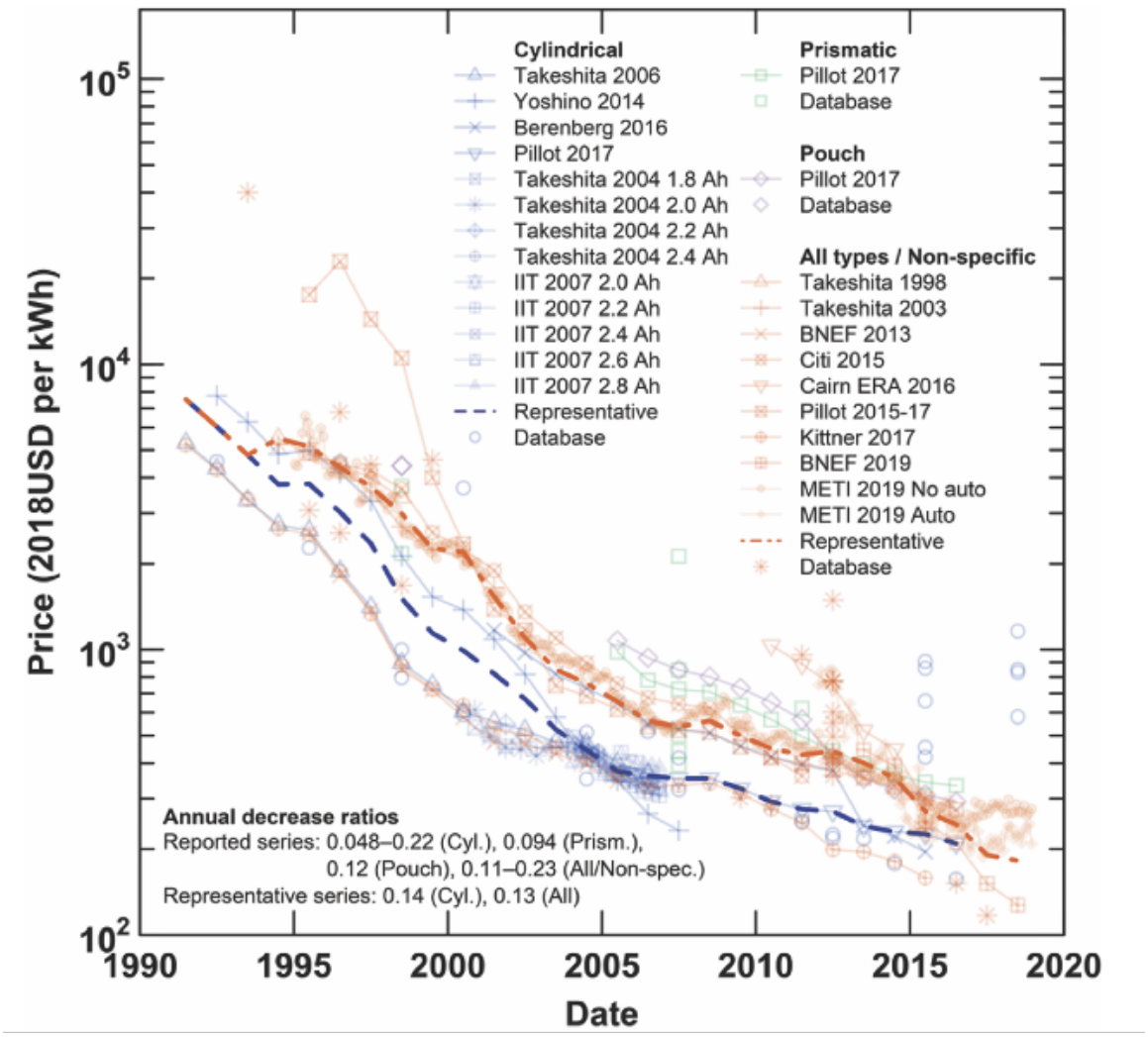

Figure 2-1: LIB cell prices from 1990 till 2020. Adapted from [72].

phosphates ($LiMPO_4$), (where M=Co, Mn, Ni, Al, Fe). More recent commercialized batteries have included blends of different types of oxides that are manganese based, such as NCM (Lithium Nickel Cobalt Manganese Oxide; $Li_xNi_yCo_zMn_aO2$) and LMO (Lithium Manganese Oxide; $Li_xMn_yO_z$), due to the lower cost of manganese.

Almost all LIB electrolytes are composed of different blends of organic carbonate solvents, including ethylene carbonate (EC) which has a cyclic structure, or linear structured carbonates such as dimethyl carbonate (DMC), diethyl carbonate (DEC), and ethylmethyl carbonate (EMC), due to their electrochemical stability and their compatible chemical and physical properties. Upon the contact of the cathode with the organic solvents, and when a potential is applied to the anode, a thin (<100 nm)

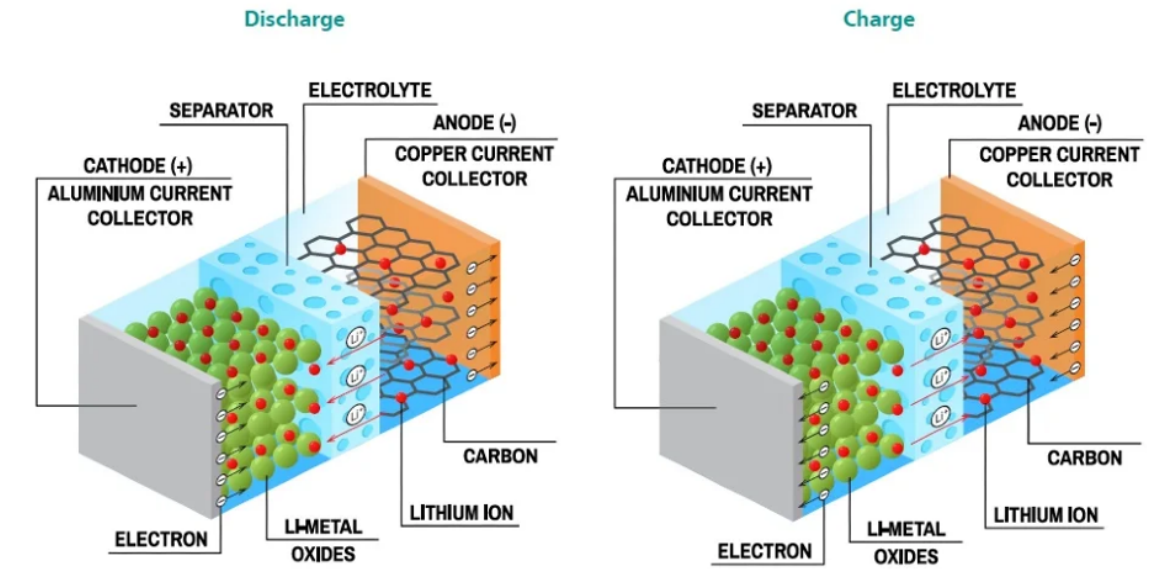

Figure 2-2: Lithium-ion movement during charging and discharging.

layer called solid-electrolyte-interface (SEI) is instantaneously formed on the electrode surfaces due to the decomposition of Li and organics. The SEI acts as a passivation layer that prevents further decomposition and interactions between the solvent and electrodes by blocking electron transfer through it, while remaining permeable towards Li^+. The composition of the SEI varies based on the electrolyte chemistry and can contain stable inorganic compounds such as Li_2CO_3 and Li_2O, as well as flammable organic constituents such as lithium alkylcarbonate. The SEI is understood to be responsible for suppressing continuing side reactions between graphite and the electrolyte and is responsible for preserving the electrochemical efficiency of the cell. A schematic of the SEI is presented in Figure 2-3.

Organic solvents have the ability to form SEIs that preserve electrochemical efficiency by preventing further electrochemical reactions between the Li and solvent. However, organic solvents are highly flammable and make the LIB only operational over a certain temperature range. Any disruption to normal operations such as a mechanical abuse or overcharging, that causes the battery to operate outside of its temperature window, may lead the battery to overheat and fail through thermal runaway. Non-flammable solvents are not practical substitutes to organic solvents

and have low efficiencies, mainly due to their inability to form such SEIs to prevent unwanted interactions involving Li.

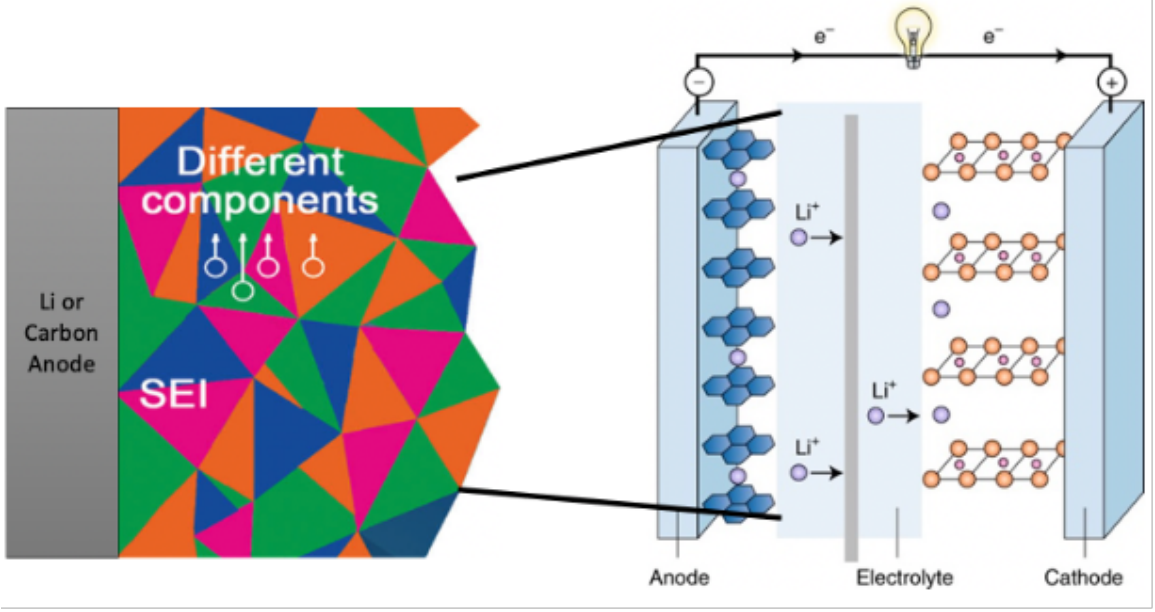

Figure 2-3: Representation of solid-electrolyte-interface. Adapted from [29].

2.2 Materials Usage in LIB

The cathodes of LIBs consist of metal oxides that include nickel, cobalt, manganese, and lithium. Cobalt and nickel are usually classified as "critical" materials. Typical EV batteries can have up to 45 pounds of cobalt[13]. More than two-thirds of the world's cobalt comes from Congo[4].

The DOE is currently funding research that aims to reduce reliance on cobalt for LIBs due to economic and security concerns[13]. Some EV manufactures have already started adopting $LiFePO_4$ (LFP) cathode chemistries that do not use cobalt for low-range vehicles[14]. The move to LFP will reduce cost and dependency on cobalt. However, they are less energy dense than cobalt-based cathodes, such as nickel manganese cobalt oxide (NMC) cathodes, which are still used for long-range vehicles. Therefore, it may be crucial to invest in research aiming to develop high energy density batteries without the need for cobalt.

Graphite is the anode material used in LIBs. China is the world's leading producer of graphite, accounting for over 60% of global graphite production[5]. China also has the second-largest graphite reserves worldwide.

About 95% of global lithium extraction comes from Australia, Chile, Argentina, and China. While Australia, through hard-rock mines, and Chile, through evaporation ponds, are the main sources of the world's lithium, China is the biggest lithium processor and LIB producer[11]. In 2020, China produced 77% of LIBs in the world. China is also leading the world in EV adoption, placing a mandate on automakers that penalizes manufacturers that don't meet EV production quotas. Figure 2-4 presents the geographical distribution, or lack thereof, of the global EV battery supply chain.

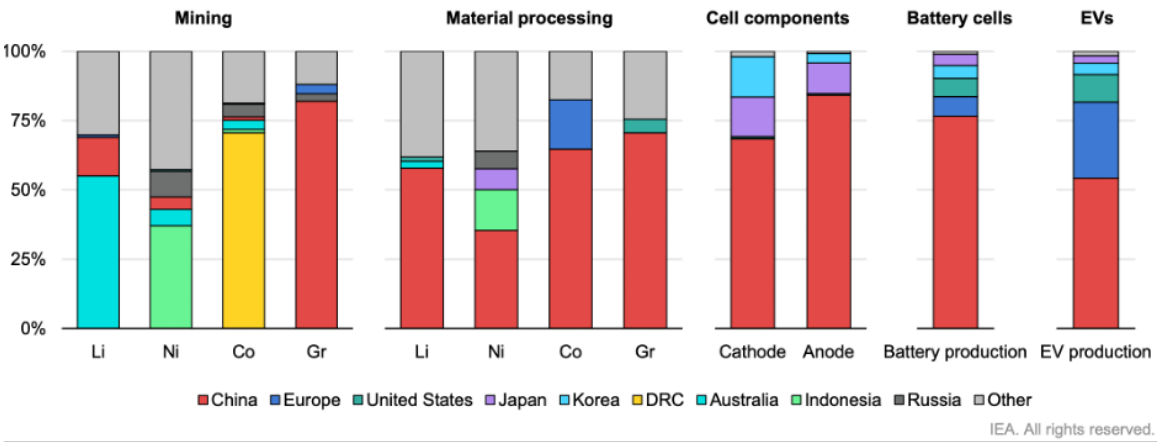

Figure 2-4: Geographical distribution of the global EV battery supply chain. Reproduced from [20].

2.3 Current U.S. Policy Interests Towards LIBs and EVs

Since 1991, the Department of Energy (DOE) Vehicle Technologies Office (VTO) has formed cooperative R&D agreements with the United States Advanced Battery Consortium (USABC), whose membership includes The Big Three U.S. automakers: Ford, General Motors, and Chrysler. The main mission of the USABC is to support nickel–metal hydride batteries, LIBs, and lithium-metal batteries for use in plug-in hybrid electric vehicles. In 2016, the DOE launched the Battery 500 Consortium among universities and DOE National Labs, which aims to develop battery technologies capable of delivering 500 Wh/kg of energy, more than twice the capacities of the state-of-the-art LIBs. The DOE has set targets for EV batteries to cost less than $100/kWh (and ultimately $80/kWh), to increase the driving range to 300 miles, and to have a charging time of 15 minutes or less.

In 2021, the DOE released the National Blueprint for Lithium Batteries, which seeks to strengthen and secure the lithium-based battery materials and technology supply-chain and production in the U.S. Additionally, the DOE Loan Programs Office received authority to disperse $17.7 billion in loans to support the manufacturing of

advanced technology vehicles, which includes EVs and LIBs. BloombergNEF projects that the transition to EVs and clean energy globally may require as much as $173 trillion in energy supply and infrastructure investment over the next three decades[16]. The study projects lithium and nickel demand will increase by five times this year's levels, whereas the demand for cobalt would increase 70%.

In November 2021, H.R.3684 - Infrastructure Investment and Jobs Act (the "Bipartisan Infrastructure Act") was passed and included $7 billion in support of the manufacturing and recycling of advanced batteries and battery materials as part of the American Battery Material Initiative.

In August 2022, H.R. 4346 – The CHIPS and Science Act of 2022 (CHIPS) was signed into law. The bill authorizes $81 billion to the National Science Foundation (NSF) over a five-year period, of which, $20 billion will be allocated to the newly formed NSF Technology, Innovation, and Partnerships (TIP) Directorate. The DOE Basic Energy Sciences Program appropriated $120 million per year for the next five years for electrochemical energy storage (batteries) R&D. The bill significantly removes DOE restrictions and prohibitions on the use of funds allocated by the Energy Policy Act of 2005 for commercial application of energy technology allowing for more private sector investments.

In August 2022, H.R.5376 - Inflation Reduction Act of 2022 (IRA) was signed into law. A major implication to EVs is a tax credit of up to $7,500 for new EVs and $4,000 for used EVs . The EVs must be assembled in North America and should not have reached a 200,000 unit sales cap (therefore, Tesla is excluded). Over the next 10 years, the Inflation Reduction Act will grant $161 billion in clean electricity tax credits and $37 billion in clean manufacturing tax credits for energy storage, solar, wind, geothermal, hydrogen, and hydropower technologies (which includes their supply chains and critical materials acquisitions). The IRA also places a 15% book-income minimum tax on corporations with an annual net income over $1 billion.

2.3.1 Demand for LIB

While LIBs have been used in consumer electronics as early as in the 1990s, they have started being adopted in EVs in the early 2010s (Figure 2-5), with the introduction of the first set of all electric zero tailpipe emissions EVs with Nissan LEAF and Tesla[17]. Full hybrid EVs (FHEVs) and mild hybrid EVs (MHEVs) have historically used nickel metal hydride (NiMH) batteries for energy storage, but have started adopting LIBs constituting the entire market for MHEVs and about half the market for FHEVs[70].

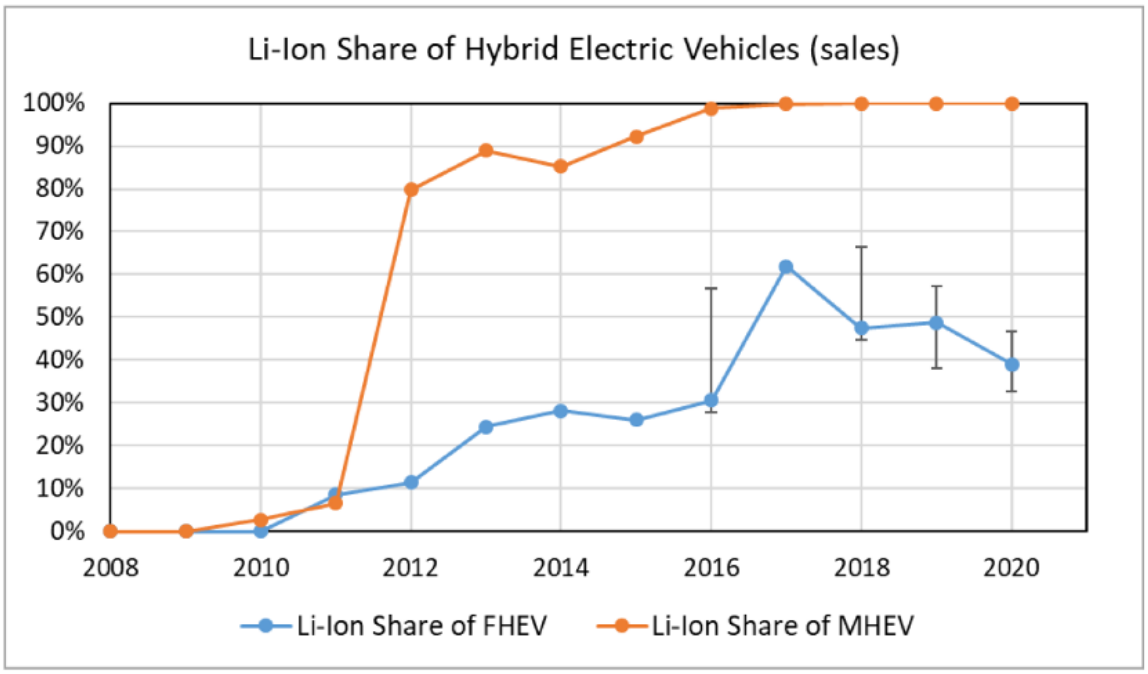

Figure 2-5: Share of LIBs in the hybrid EV market[70].

According to the DOE National Blueprint for Lithium Batteries, by 2028, the U.S. will have a LIB demand of 320 GWh but have 148 GWh of LIB production capacity based on the public commitments of companies. In the same projection, China will be producing 631 GWh of LIBs in 2028. The U.S. market for LIBs is currently valued at over $70 billion and is projected to be around $278 billion by 2030, with a compound annual growth rate of 19%[9]. The projections for worldwide demand of EV LIB at a global scale are shown in Figure 2-6. Figure 2-7 displays the cumulative sales of EVs and the corresponding market proportions.

The U.S. manufacturing capacity as a percentage of global manufacturing capacity

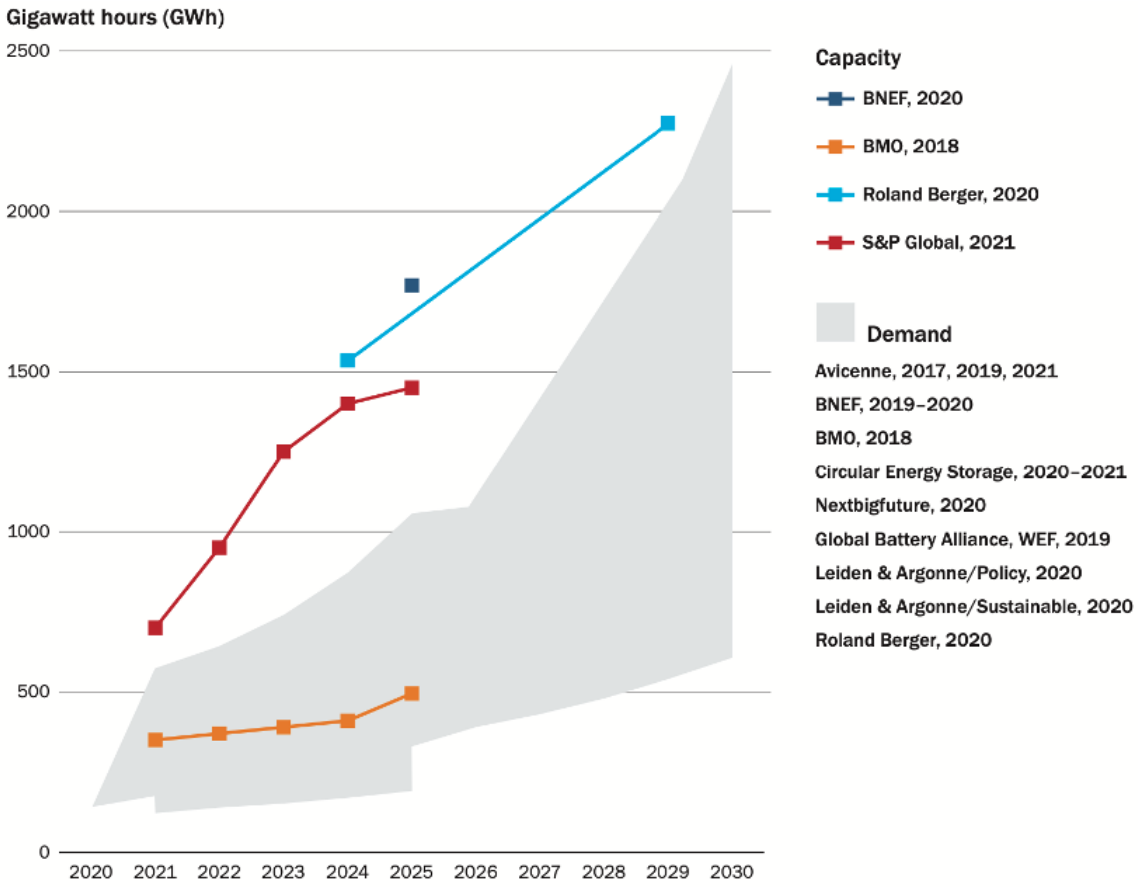

Figure 2-6: Global EV LIB demand projections. Reproduced from [19].

produces 0% of cathodes, 10% of anodes, and 2% of electrolyte solution for LIBs[19]. In an assessment of the U.S. LIB manufacturing industry, the National Blueprint for Lithium Batteries has identified major threats to be the limited number of domestic cell manufacturers and the vulnerability to supply disruptions. The report also identifies major opportunities to be the expected rapid growth of the EV market (and hence the LIB market) along with job creation, economic growth, and a boost to the U.S. auto industry.

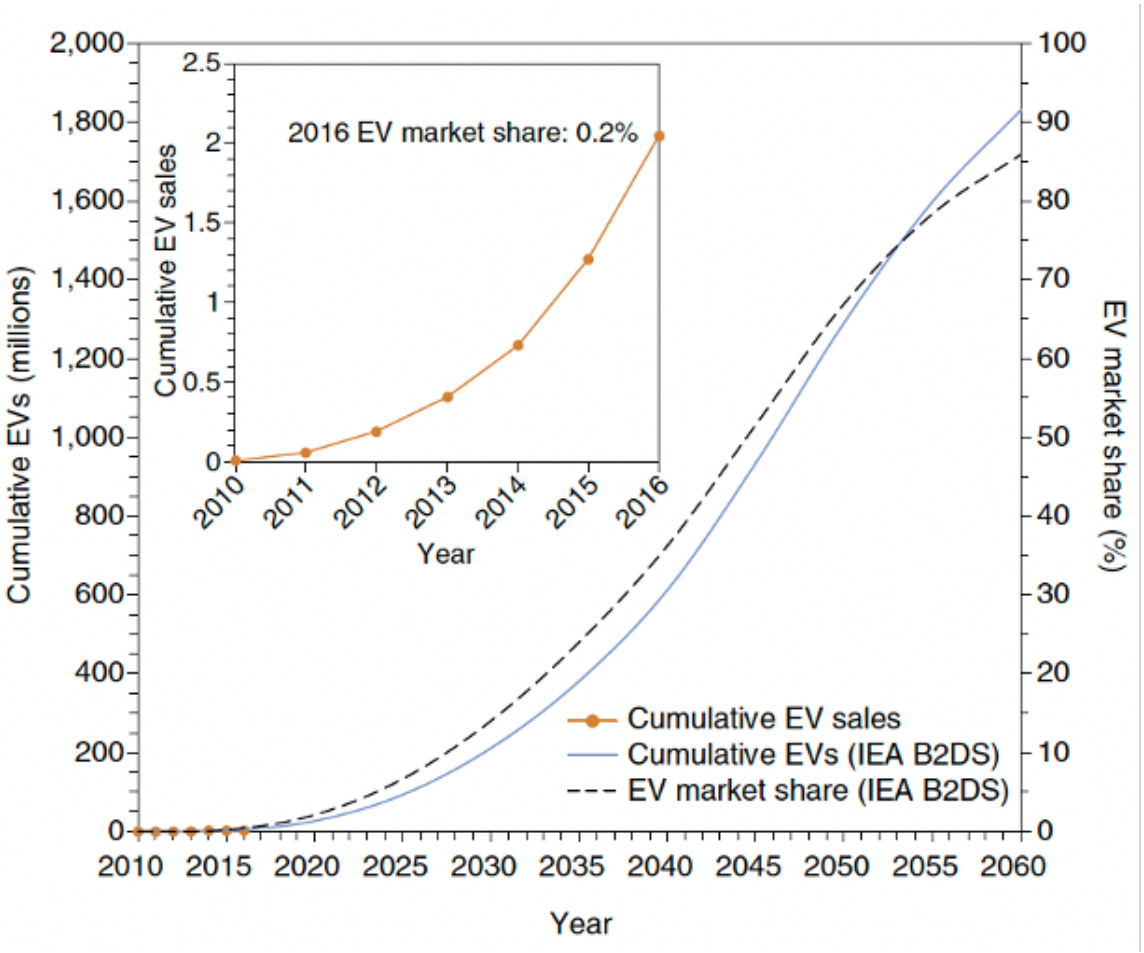

Figure 2-7: Cumulative EV sales and EV market share[28].

2.3.2 LIB Recycling Processes

LIB components are heterogeneous and consist of numerous organic and inorganic materials. LIBs consist of metallic (steel and aluminum) and plastic covers and casings, cathodes consisting typically of tertiary metal oxides, graphite anode, organic-based electrolytes, polymer separators, and other inorganic additives added to the solvent. Cobalt followed by high-purity nickel have been identified by the DOE and the U.S. Geological Survey (USGS) to be critical metals for energy storage technologies, especially given their scarcity. Nowadays, the main goal of LIB recycling is to recover the valuable constituents, primarily cobalt and nickel. Lithium is also valuable, however, its recovery has not yet been economically feasible.

The composition of LIB waste depends on the recycling process. LIB recycling involves both physical and chemical processes. The typical stages in LIB (and in batteries in general) are mechanical treatment, hydrometallurgical treatment, thermal pretreatment, and pyrometallurgical treatment (Figure 2-8).

In mechanical treatment, the first step is to discharge the battery, given that high energy-density LIBs are susceptible to undergoing thermal runaway. After discharging, LIBs have to be disassembled to segregate components into those that cannot be recycled and those that can be recycled, which is further divided by those that can be recycled at a typical recycling facility (such as the steel, aluminum, and plastic casings) and those that require a battery recycling facility (such as the anode and cathode active materials). The disassembly of LIBs is one of the most time- and labor-intensive processes, given that the process is currently not automated and has to be conducted manually due to the variability in LIB design depending on the manufacturer.

The disassembly process is followed by thermal treatment which starts with the evaporation of the electrolyte from the battery components; this is done by subjecting the battery components to heat (the solvent is organic-based therefore heating temperatures are well below 100°C). The cathode is then heated in a furnace typically around a temperature of 150°C for 1 h[34]. The anode is also incinerated at temperatures around 800°C[34].

After heating, the battery components are then crushed and grinded, followed by sieving to obtain finer particle size and filter out the desired cathode and anode active material from polymer separators and metallic meshes (current collectors). The resulting powder is referred to as "black mass". Facilities typically use magnetic separation to separate out steel pieces, and some facilities have been testing the separation of aluminum foil using ultrasound separation. The black mass, which is composed of the cathode and anode active material, consists of the most valuable constituents (cobalt, nickel, lithium).

Pyrometallurgy, hydrometallurgy, or a combination of the processes are widely adopted to recycle spent LIBs.

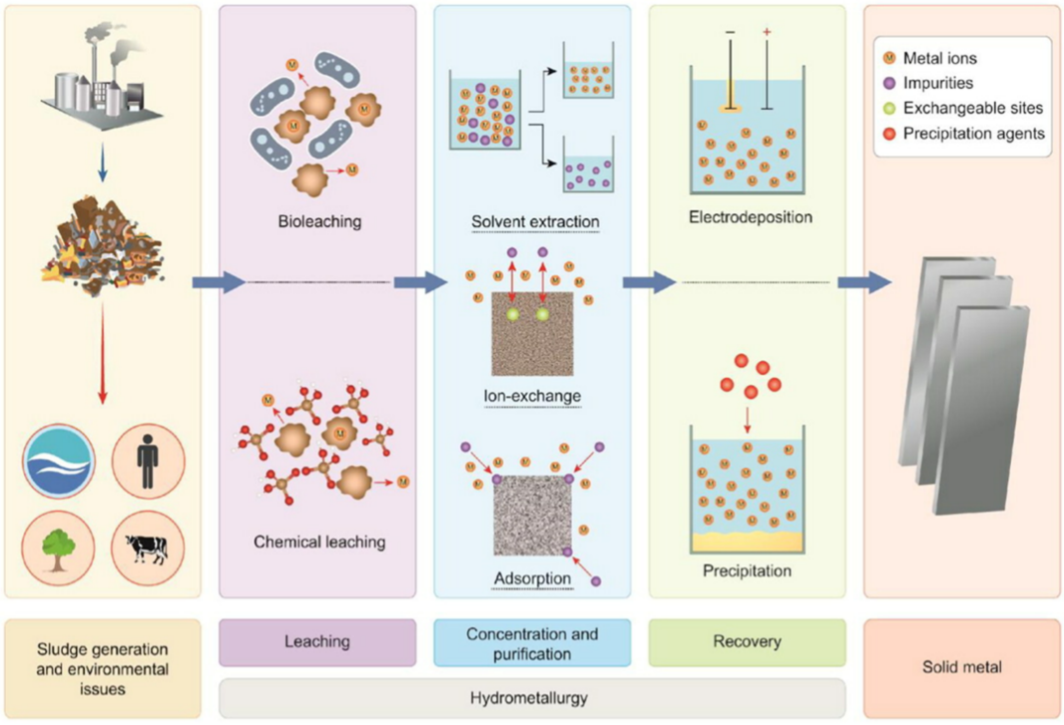

Figure 2-8: Hydrometallurgy involves leaching, solvent extraction, reduction, and precipitation. Reproduced from [69].

In hydrometallurgy, the inorganic acids typically used in leaching are hydrochloric acid (HCl) and sulfuric acid ($H2SO_4$)[34].

Following leaching, the desired metals are recovered from the leaching solution using solvent extraction or co-precipitation. Cyanex 272, D2EHPA, and PC-88A are commonly used extractants to recover cobalt and nickel[34]. Lithium is typically recovered using precipitation, using the difference in the solubility in different metals by altering the pH and temperature of the solution.

Pyrometallurgical processes involve elevating the temperatures of the blackmass to remove organic material from and causes reactions in the cathode and anode materials (in the blackmass) to allow them to be soluble in solutions to enable metal recovery.

2.3.3 Importance of LIB Reuse and Recycle After Usage in EV, with Highlight on Safety

In the U.S., upstream battery recyclers such as Criba often focus on converting the spent batteries (which includes spent LIBs) to blackmass. The blackmass, which is not a thermally explosive hazard, is easier to ship. Upstream recycling involves mechanically crushing and then thermally treating the batteries to obtain blackmass. While in principle, the processes are not complex, the biggest bottle neck faced by those recyclers is the manual disassembly of the batteries, and therefore, they have to balance between how further to keep disassembling and when to crush. Manual EV battery disassembly is required due to the variability in battery design. Different EV manufacturers design battery management systems in significantly different ways. This makes the labor involved in EV LIB recycling one of the biggest cost drivers.

Major upstream recyclers, such as Cirba, are not yet solely focusing on recycling LIBs, and typically recycle all types of batteries. Batteries are recycled based on types (nickel-metal-hydride batteries are recycled separately from LIBs, separately from lead–acid batteries), but all LIBs can be converted into blackmass together, and do not have to segregated based on particular LIB cathode chemistry (Nickel Manganese Cobalt (NMC) and Lithium Iron Phosphate (LFP)). The input to these facilities varies from recalled batteries to damaged batteries, spent batteries, and battery scrap from manufacturers. One recycler company interviewed, Cirba, charges to recycle LFP-based LIBs but purchases NMC-based LIBs to then recycle. This is because NMC-based LIBs contain the valuable cobalt and nickel which can then be sold in blackmass form for profit. Similarly, LIB recyclers are not incentivized to recycle cell phones as the amount of critical material is on the microgram scale and not profitable.

Due to the very large and exemplary U.S. recycling infrastructure to low value goods such as plastics, cardboard, and municipal waste, it will not be significantly difficult to expand to LIB recycling. Currently, lead acid batteries are the most widely recycled batteries in the U.S.

Waste informatics and population informatics can be leveraged to determine the need of EV batteries recycling facilities in a given geographic location. Given that EV batteries can be explosive, smaller recycling plant sizes are more beneficial as they can be distributed and require less transportation to ship an EV LIB to a recycling facility, hence bringing down the costs. In addition to economic benefits, LIB recycling has environmental benefits given that the greenhouse gas emissions circumvented from mining of raw materials is about 3 kg-CO_2-equiv/kg-Co and 15 kg-CO_2-equiv/kg-Li[6].

The major evidence of a defective battery that has an increased risk of fire is the swelling of the battery. Cirba works with Kulr Technology to transport such defective batteries. These dangerous batteries are isolated during shipment and during processing since they can undergo thermal runaway and cause an explosion. Cirba provides recycling kits and kiosks for consumers to place small batteries found in consumer electronics that they want to recycle. Additionally, Cirba has its own fleet of vehicles to specifically transport batteries that cannot be shipped using conventional carriers, typically large battery packs and modules. Interviewees have noted that labor costs are an issue, especially given that for high voltage packs, skilled labor is required to disassemble them by hand. Interviewees have attributed safety concerns as a major factor that has not allowed for large-scale automation of LIB recycling processes.

2.4 Major Thermal Safety Concerns in LIBs

LIBs are energy dense, store a large amount of energy (about 200 Wh/kg), possess two highly reactive electrodes, one strongly reducing and the other highly oxidizing, and has a highly flammable organic-based electrolyte. Moreover, the interplay between the anode-electrolyte-cathode is exothermic. The cathode transition-metal oxides in a LIB have lattice oxygen which can be released at high temperatures greater than 200°C[48]. The LIB electrolytes are organic-based and flammable. The anode contains intercalated Li^+ in LIBs or Li-metal in LMBs. Therefore, enclosed in a battery is an oxidizer (cathode) and fuels (electrolyte and anode). Disruptions to

normal operations can lead to an ignition source, which can then complete the fire triangle and lead to fires.

The flammable nature of organic solvents makes LIBs only operational over a limited temperature range. Any disruption to normal operations such as a mechanical abuse, short-circuiting, or overcharging, could lead to thermal runaway. As the temperature increases, the solvent starts to decompose, releasing oxygen, hydrocarbons, and other flammable organics. When enough oxygen is produced in the cell, and at a sufficiently high temperature, the flammable gases burn, causing fires. Even if the interior components of the battery are not exposed to outside air (i.e., battery casing is not shattered yet), the solvent can act as a fuel and the internally produced oxygen can act as the oxidizer, which burn in a process resembling oxy-combustion (combustion in pure oxygen, as opposed to in air).

The thermal runaway mechanism is a very dynamic process with many interactions between the electrodes and electrolytes and their constituent chemicals. The onset of heating is the first step in thermal runaway, which can be a result of overcharging (voltage of battery exceeds the set point), internal short circuits, or mechanical damages or disruptions. Internal short circuits typically occur when lithium dendrites form under high current density. Lithium dendrites may start accumulating on the electrodes and eventually pierce the separator, ultimately resulting in internal short circuits. The effects of joule heating are negligible compared to the interactions that may occur due to anode-cathode cross talk[48]. As heat starts to accumulate in the cell, the SEI starts dissolving into the electrolyte and decomposing, leading to further interactions between the electrolyte and the anode. The degradation of the SEI at around 80-120°C is regarded as the major factor in initiating thermal runaway. Gases start evolving from the organic phases present in the electrolyte and SEI, and at temperatures close to 200-250°C, the cathode starts decomposing and releases lattice oxygen[48]. The thermal runaway occurs when there is continuous heat release (due to battery chemistry) that is greater than the dissipation of heat by the system.

2.5 Reasons for LIB Thermal Runaway

The LIB fail rate has been estimated to be 1 in 40 million[31]. According to the Federal Aviation Administration Office of Security and Hazardous Materials Safety, in the U.S., there have 412 incidents involving LIBs during air or cargo transportation from 2014 till 2022 (Figure 2-9). Tesla claimed that during the 2012-2021 period, there was roughly one Tesla EV fire for every 210 million miles traveled.

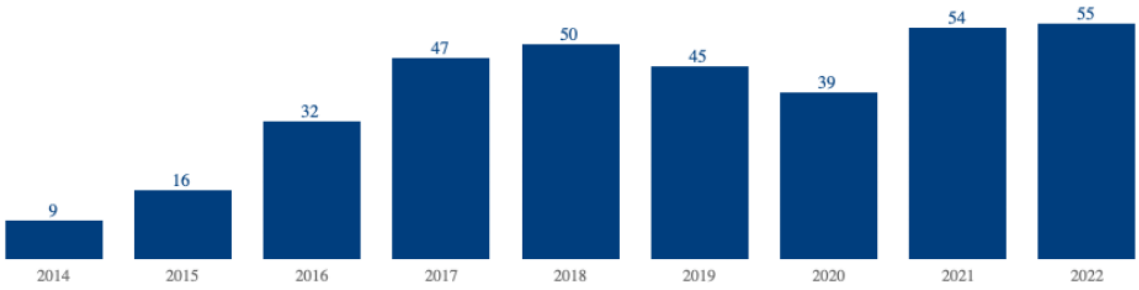

Figure 2-9: Lithium battery incidents in air or cargo transportation in the U.S. over the past 9 years[7].

According to data from insurance companies, the National Transportation Safety Board, and the Bureau of Transportation Statistics, hybrid vehicles (which have an ICE and an electric-powered motor) had the most fires with 3,475 fires per 100,000 vehicles followed by ICE vehicles and EVs with 1,530 fires per 100,000 and 25 fires per 100,000 respectively[60]. However, even with that, there have been tragic deaths related to EV fires.

The reasons for LIB thermal runaway can succinctly categorized as mechanical failure, electrical failure, or thermal abuse. Mechanical failure is due to crushing or piercing of the battery, design or manufacturing defects, faulty parts such as separators, or any mechanical deformation that occurs (such as due to a crash). Electrical failures are more common and include overcharging, overdischarging, faulty wiring, internal short circuits, dendrite formation, and external short circuits. Abnormal use of the battery may lead to electrical failures. Thermal failures occur when the LIB is subjected to high temperatures which can lead to over-heating. Typically, mechanical failures or thermal abuses lead to internal short circuiting which ultimately leads to thermal runaway. Internal short circuits are the predominant reason for thermal

runaway in LIBs[47].

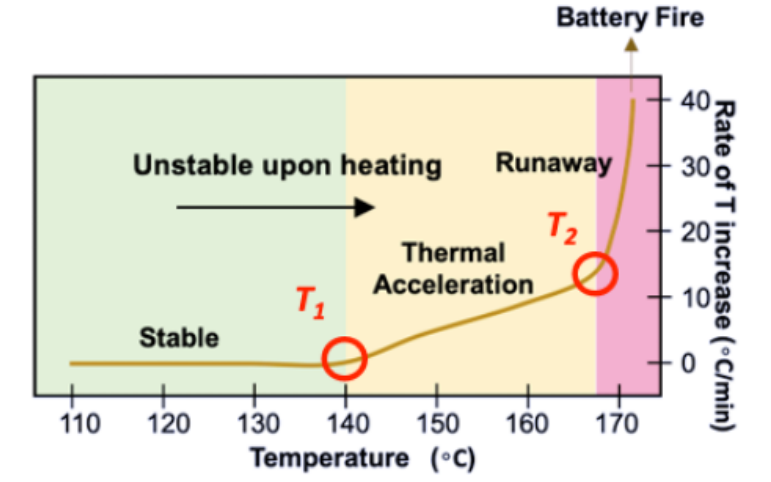

Figure 2-10: Calorimetry of a LIB where T_1 is the the onset-temperature and T_2 is the thermal runaway point.

Under normal operation of LIBs, electrochemical interactions within the cell lead to reversible and irreversible heat generation. However, thermal runaway occurs when the heat generation exceeds the heat dissipation of the LIB, with the accumulated heat increasing the temperature up to a point of no return, defined as the thermal runaway point (Figure 2-10). The thermal runaway point has been defined in literature as either a heat increase rate of 1°C/min or 10°C/min.

The mechanical failure, electrical failure, or thermal abuse are factors that initiate thermal runway. As the temperature increases due to these factors, the SEI starts decomposing and becoming soluble in the electrolyte, exposing the anode to the electrolyte. Exothermic reactions and interactions between the anode and electrolyte increase the temperature of battery. At elevated temperatures, the metal oxide cathode releases lattice oxygen into the cell and the cathode-electrolyte interface decomposes allowing for reactions between the cathode and electrolyte and the cathode and anode. The thermal responses of individual battery constituents are analyzed to understand the mechanism in which the batteries undergo thermal runaway and to determine trigger reactions. The onset-temperature (T_1) and thermal runaway point (T_2) depend on the specific battery chemistry and are determined using calorimetric means (discussed in subsequent chapters). Figure 2-11 illustrates the interactions of

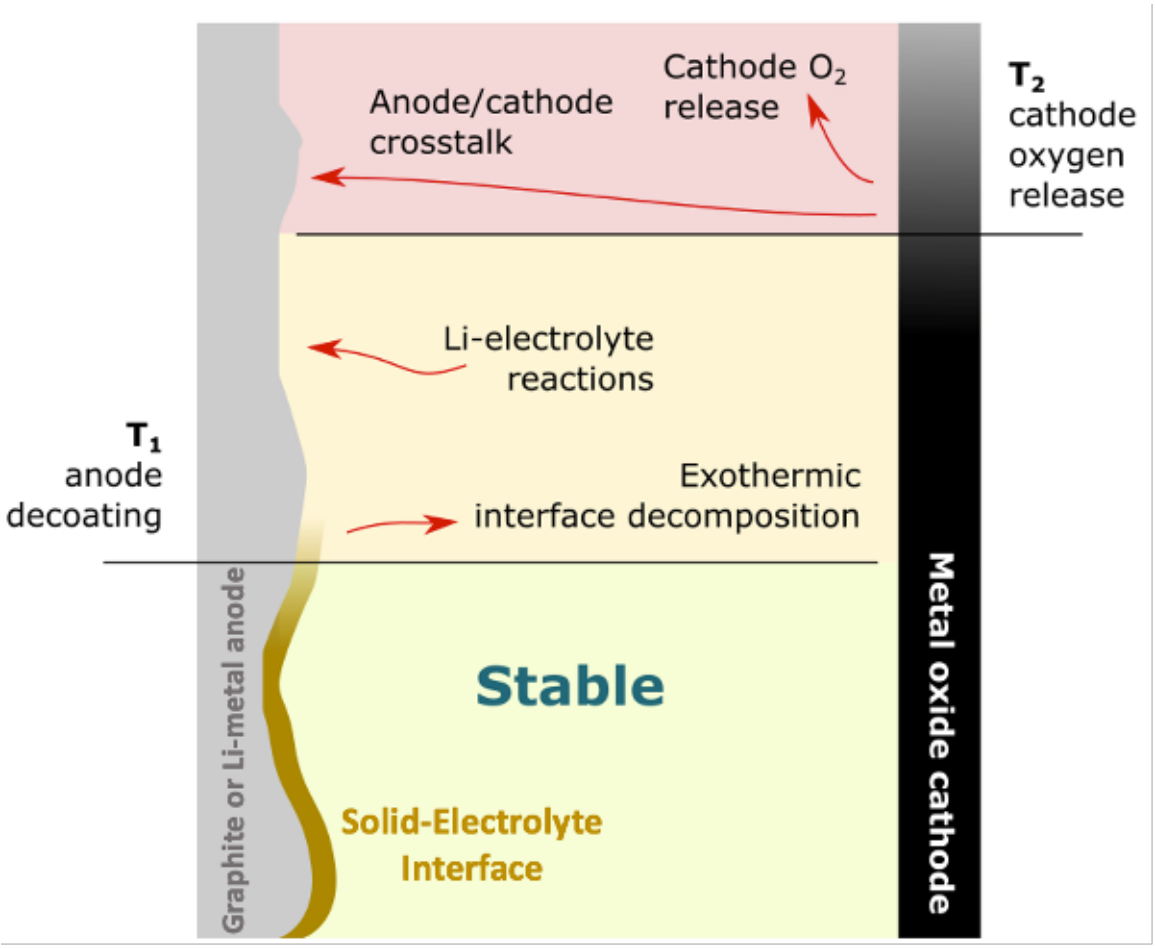

Figure 2-11: Schematic of LIB interactions at elevated temperatures.

LIB components under high-temperature conditions.

2.6 Phenomenological Approaches to Understanding LIB Safety

Phenomenological behavior of LIBs are important in understanding LIB safety and its operational limitations. Major phenomenological based approaches include bomb calorimetry where the battery or cell are heated in an enclosed chamber with temperature sensors and multimeters to measure the voltages and currents as the cell heats up (Figure 2-12).

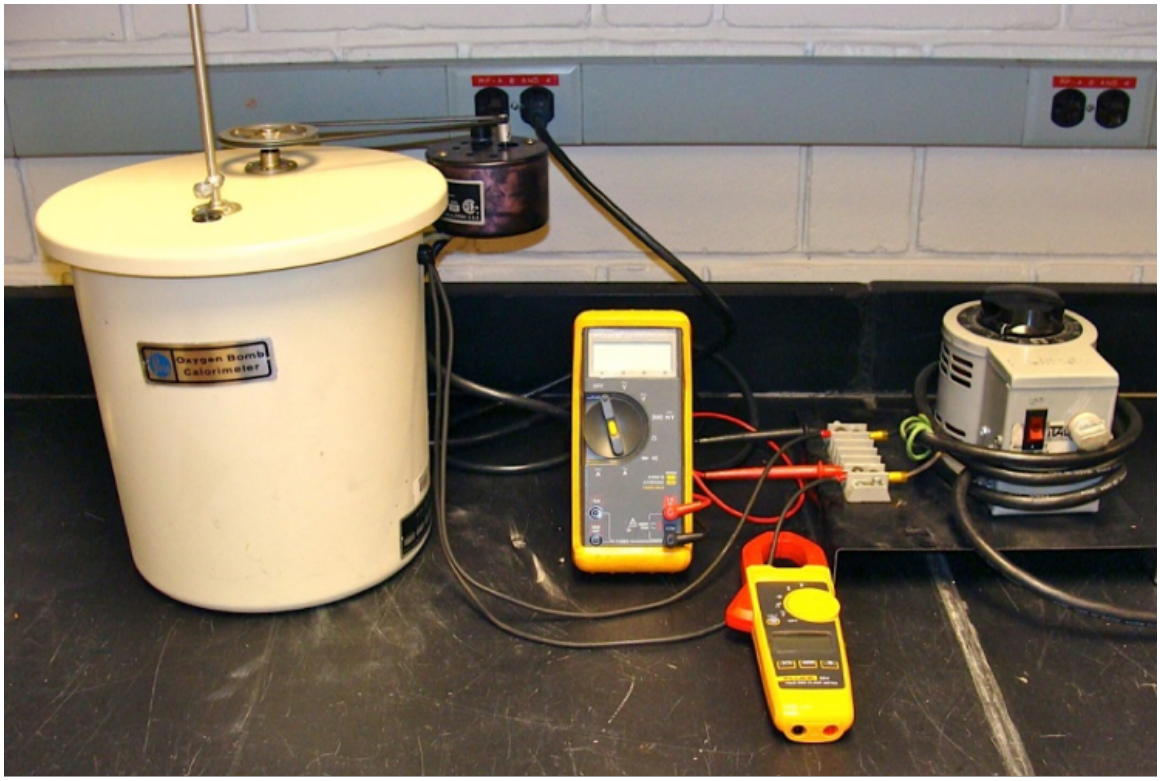

Figure 2-12: Bomb calorimetry setup to measure the temperature profile of battery heating. Reproduced from [39].

Nail penetration tests are safety test that subjects the battery to an internal short circuit by piercing a nail through the battery (see Figures 2-13 and 2-14). Parameters that are usually tested during such experiment are nail diameter, insertion depth, position of insertion, and speed of the nail insertion. Phenomenological behavior observed are vigorousness and the behavior of the flame or explosion, shattering of the battery casing, and maximum temperature of the testing chamber. In some setups, if appropriate temperature sensors and probes are installed, the heat release and temperature profile can be obtained from the nail test being conducted. Nail penetration tests are sometimes used to compare the "flammability" of cells of different chemistries (as shown in Figure 2-13).

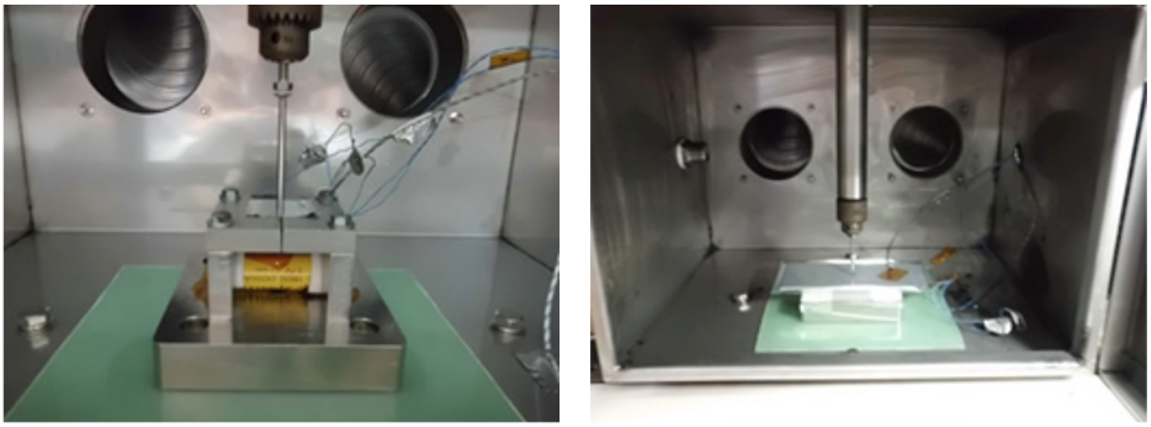

Figure 2-13: Nail penetration test conducted on 18650 cylindrical cell (left) and pouch cell (right). Reproduced from [2].

Electrolyte flame tests are conducted by saturating a separator, usually a polyethylene separator, with the electrolyte of interest and subjecting the saturated separator to a flame (Figure 2-15). The flammability of the electrolyte is an important factor that can be used to further understand the electrolyte-anode-cathode reactions.

Figure 2-14: Nail penetration test for 18650 cells. Top: blank before nail test. Middle: unique electrolyte blend that is concluded to be "less explosive" Bottom: commercial carbonate-based electrolyte blend that is concluded to be "more explosive". Reproduced from [67].

.

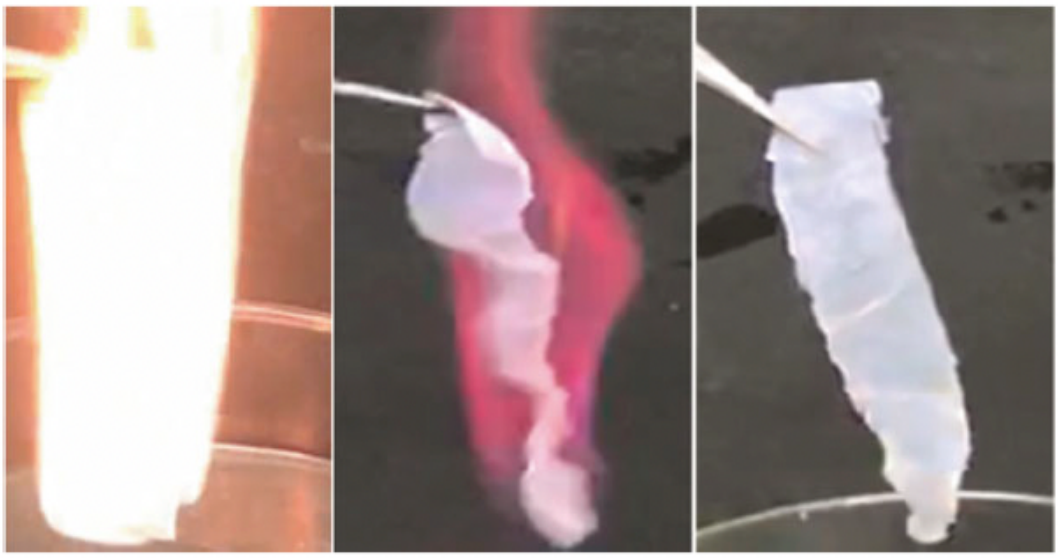

Figure 2-15: Different electrolytes subjected to a flame test, from "most flammable" on the left to "not flammable" on the right. Reproduced from [39].

Chapter 3

Equipment and Methods

LIBs are energy dense and can "explode" dynamically. To understand the thermal behavior of LIBs at elevated temperatures, it is more useful to also understand the thermal responses of individual components of LIBs than to solely analyze the thermal response of the full cell. The numerous pieces of equipment used to analyze thermal behavior have usually been applied to study polymers. Only recently in the past 20 years have these equipment been utilized to study LIBs. In this chapter, we will examine the most commonly used pieces of equipment: the thermal gravimetric analyzer (TGA), differential scanning calorimeter (DSC), and briefly the accelerating rate calorimeter (ARC).

The TGA measures the mass of a sample as a function of temperature. In the comprehensive overview of the TGA, the foundational principles, along with the apparatus's setup and configurations, are presented. The discussion further explores potential inaccuracies in TGA readings, emphasizing concerns such as buoyancy and thermal expansion. Different methods used to extract physical and chemical changes from TGA data are also presented.

The DSC measures heat flow across varying temperature spectra. The mechanisms of the DSC are detailed, explaining how it measures endothermic or exothermic heat flows and can be employed to detect phase changes like melting that do not involve mass loss. DSC techniques in the context of analyzing the heat transfer properties of LIB components are discussed. Within an insulated DSC furnace chamber, the sample

and reference crucible can either be enclosed, sealed under vacuum, or configured to allow the flow of purge gases. Unlike the TGA that can be used to directly collect mass-temperature data, before the execution of a sample run, the DSC has to undergo signal corrections and calibrations. DSC signal correction is used to eliminate any DSC noise signals that arise from the crucible that holds the sample. DSC signal calibration is vital to convert raw signals into units of heat flow, using calibration-grade materials such as sapphire with known heat capacities. DSC can offer insights about the heat transfer properties of a sample, and can be utilized in assessing the degree of phase conversion.

3.1 Thermal Gravimetric Analyzer (TGA)

3.1.1 TGA Fundamentals

The thermal gravimetric analyzer (TGA) (also used to describe the technique of the equipment, thermal gravimetric analysis - TGA) is an equipment that measures the mass of a sample as a function of temperature, through a controlled temperature program and controlled environment. The temperature range typically starts at room temperature and the maximum temperature varies among commercial TGAs, and can reach 1200°C or more. For LIB analysis, temperature ranges above 500°C become of less value to study since it is well above the point of thermal runway where the failure and damage has occurred. A picture of the TGA model used in the Ghoniem Group is shown in Figure 3-1.

The sample is loaded into a pan that is then enclosed in a furnace chamber. The material of the pan of choice depends on the properties of the sample and any interaction it may have with the pan. For LIB components, we have used platinum pans since they are more inert and less reactive than ceramic pans (different pans are shown in Figure 3-2). Pan volumes vary from 100 to 500 μL. The pan is hung on a thermobalance that can handle weighing a sample as it heats or cools. The sample pan and the thermobalance are also connected to an empty identical internal pan made

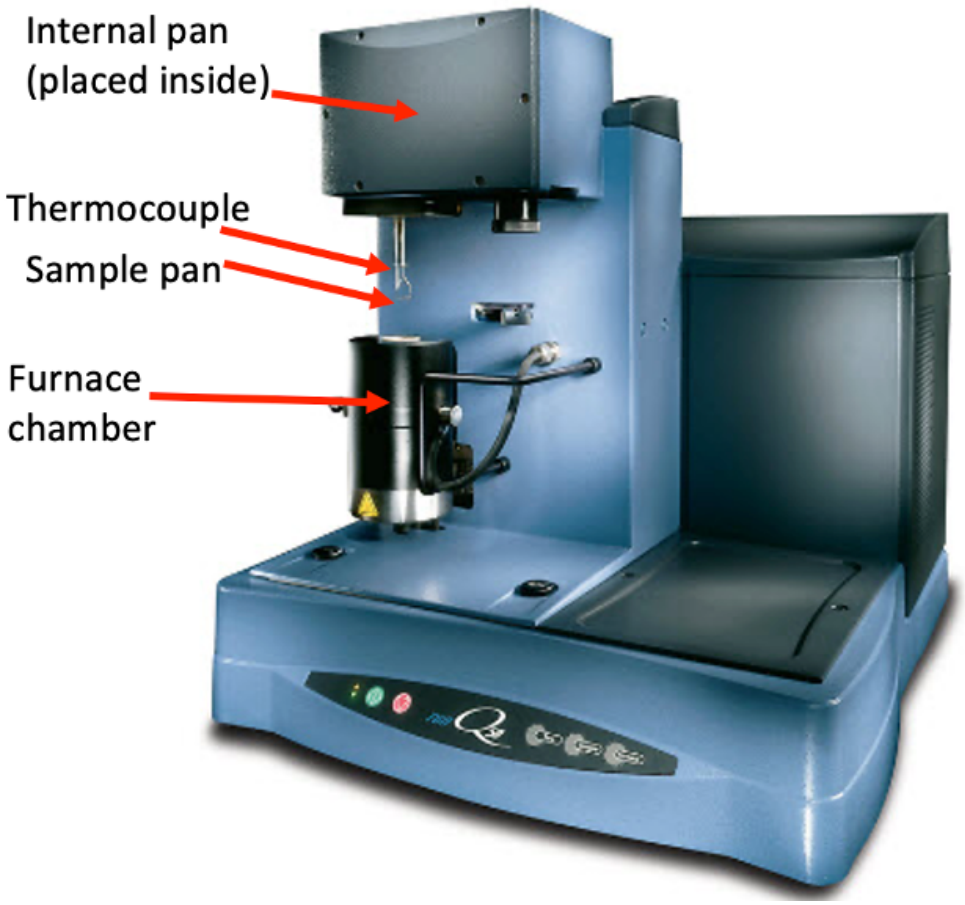

Figure 3-1: TA Instruments Q50 Thermogravimetric Analyzer.

of the same material type that is placed inside the TGA machine (not in the furnace where the sample pan is placed). The sample pan is first placed empty (without the sample) and calibrated against the internal pan ("zeroed"). Following this, the sample is placed inside the sample pan and is loaded into the furnace chamber for the TGA experiment to begin. The furnace chamber has purge gas flowing through it to maintain a certain environment surrounding the sample; gases can be inert, oxidizing, or reducing, depending on the experiment and sample being conducted. Given that LIB components are moisture and oxygen sensitive, argon was used as the sample environment gas. To minimize the effect of any buoyancy effect, the internal balance gas inlet was set at the same flowrate as the argon; however, nitrogen gas was used for the internal gas inlet since it is cheaper than argon.

Figure 3-3 is a schematic of the internal components of a TGA. TGAs can typically

Figure 3-2: TA Instrument sample pans: platinum (top), aluminum (middle), and ceramic (bottom).

handle sample masses of up to 1.00g; however, the sample mass is usually confined by the volume and dimensions of the pan in use.

3.1.2 TGA Errors

Errors that can occur in TGA measurements are the thermal expansion or contraction of the thermobalance components during temperature change, thermal conductivity, electronic sensor sensitivity loss, atmospheric turbulence in the environment of the furnace chamber, and chemical reactions and condensation within the TGA pan[53]. The TGA pan hooks (downward "V" shaped) can be bent and such bending may affect the accuracy of the mass measurement if the thermobalance is not in contact with the hook exactly at the center of the hook.

Buoyancy is the upward force exerted by the purge gas on the sample. The purge

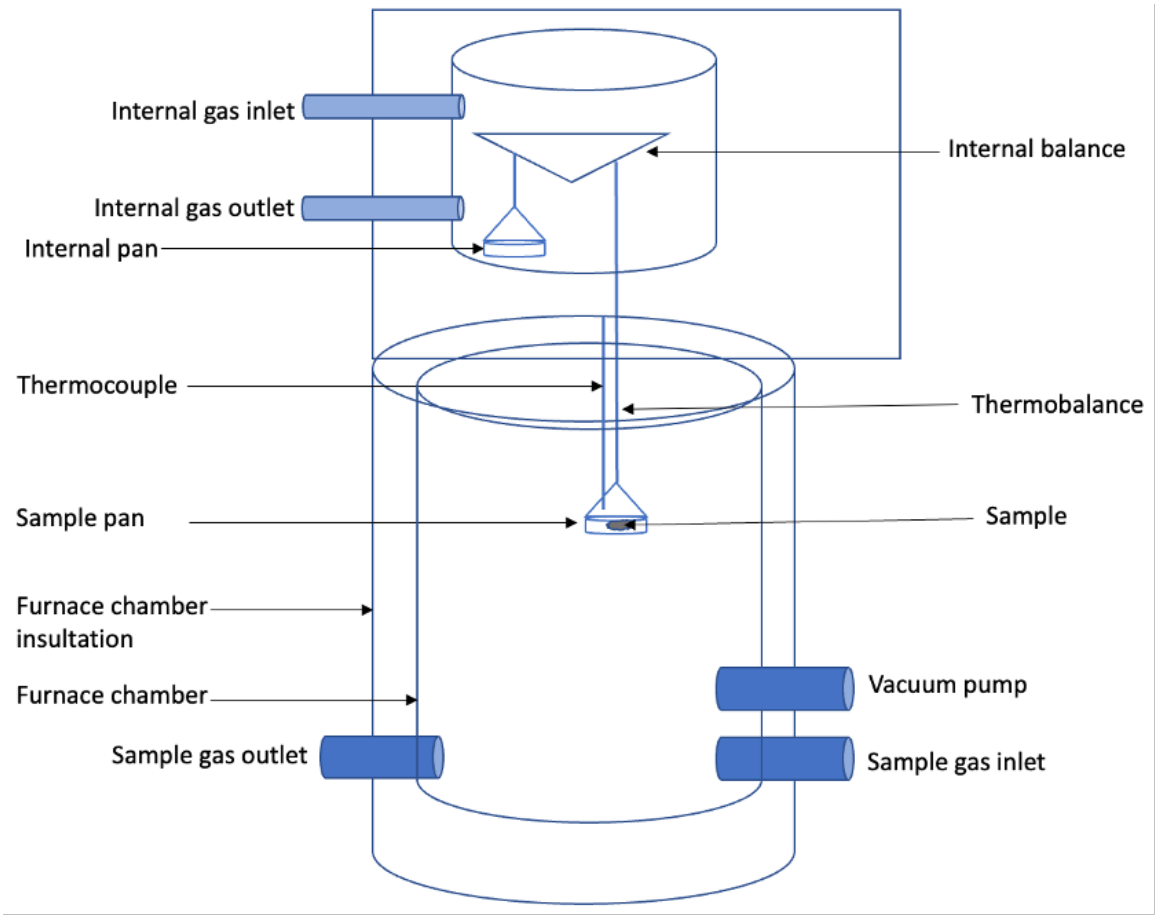

Figure 3-3: Schematic of internal components of TGA.

gas may exert an upward force on the sample, exhibiting a buoyancy effect which can alter (increase) the true mass of the sample. As the temperature increases in the furnace chamber, the purge gas density decreases. Depending on the sample dimension and shape, this gas density decrease may result in an apparent sample mass gain. If a buoyancy effect is observed, a possible solution to overcome it is to run an empty sample pan TGA experiment with the same temperature profile and same purge gas (and purge gas flowrate). This buoyancy correction run can then be subtracted from the actual run. Another less common method to correct for buoyancy is to run an inert sample with similar shape dimensions as the sample of interest in order to obtain noise of the TGA run.

3.1.3 Physical and Chemical Properties from TGA Experiments

TGA measurements can give information on evaporation, thermal decomposition, and phase transition. TGA data are useful since it can identify critical temperature domains. An example of a TGA output is shown in Figure 3-4.

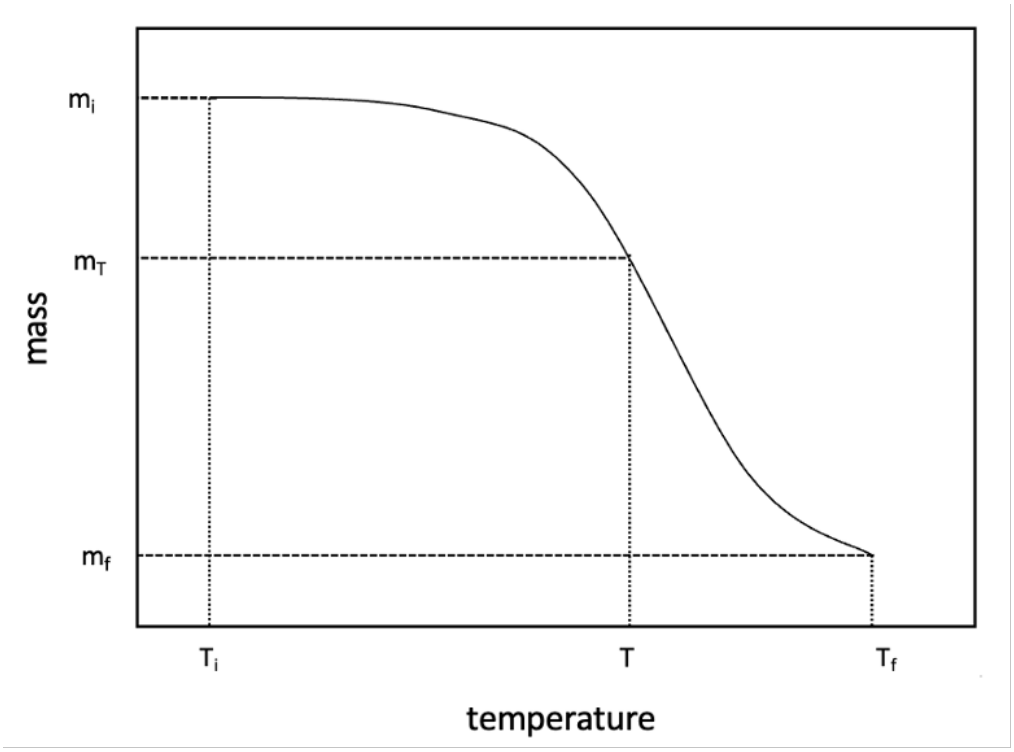

Figure 3-4: TGA heating plot of mass as a function of temperature.

The extent of conversion (α) can be determined from the TGA measurement as follow

$$\alpha = \frac{m_T - m_i}{m_f - m_i} \tag{3.1}$$

where m_T is the mass at temperature T, m_i is the initial mass, and m_T is the final mass of the sample for a given interval. The conversion-temperature curve can be plotted to understand the kinetics of the thermal degradation process.

The rate equation of a single-step reaction can be expressed as

$$\frac{d\alpha}{dt} = k(T)f(\alpha) \tag{3.2}$$

where $k(T)$ is the reaction rate constant and $f(\alpha)$ is the reaction model. Similarly, multi-step reactions or processes can be expressed as

$$\frac{d\alpha}{dt} = k_1(T)f_1(\alpha) + k_2(T)f_2(\alpha) \tag{3.3}$$

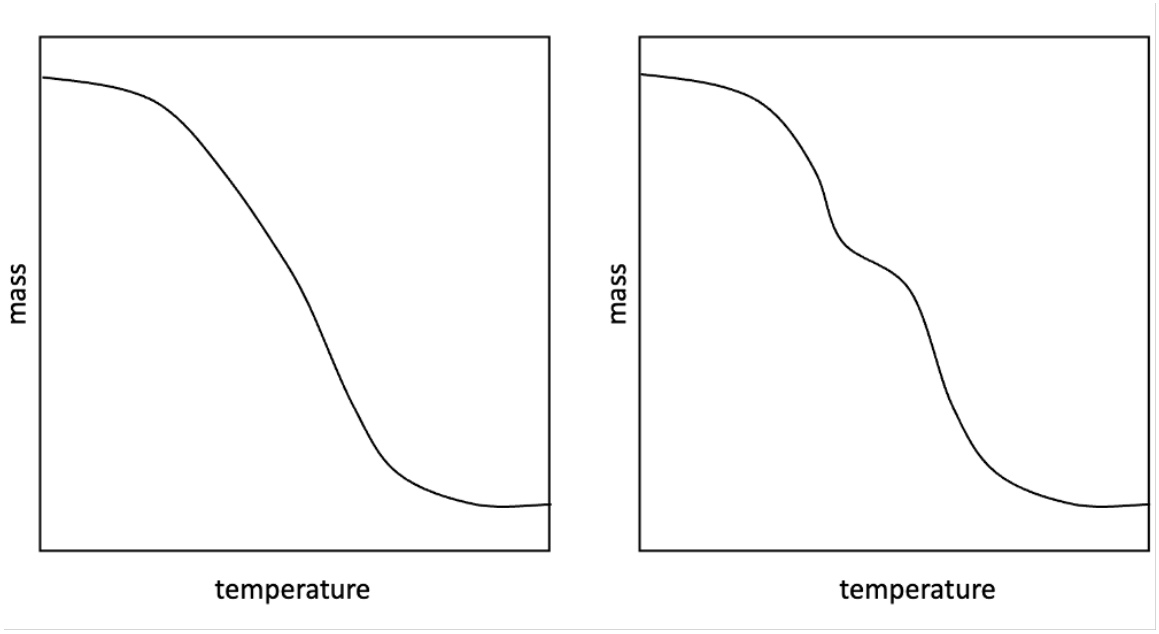

Figure 3-5: TGA profile of a single-step mass loss (left) and two-step mass loss (right).

Multi-step reactions or processes have different TGA profile shapes in comparison to single-step reactions, as shown in Figure 3-5.

The reaction rate constant is dependent on the temperature of the process, and can be typically modeled with the Arrhenius equation

$$k(T) = A\exp\left(\frac{-E_a}{RT}\right) \tag{3.4}$$

where A is a pre-exponential factor, E_a is the activation energy for the reaction, T is the absolute temperature in Kelvin, and R is the universal gas constant.

The rate equation for a single-step reaction can be expressed as

$$\frac{d\alpha}{dt} = A \exp\left(\frac{-E_a}{RT}\right) f(\alpha) \tag{3.5}$$

The reaction models, $f(\alpha)$, are typically expressed using different forms of power - law models. The choice of power-law model typically depends on the conversion dependence of the reaction rate (of time).

Accelerating models are those whose rate steadily increases with the extent of conversion and decelerating reaction models are those whose rate steadily decreases with the extent of conversion. A maximum conversion rate $\frac{d\alpha}{dt}$ observed between zero conversion ($\alpha = 0$) and complete conversion ($\alpha = 1$) is classified as autocatalytic conversion. Figure 3-6 show the shapes of conversion vs. time curves of decelerating, accelerating, and autocatalytic reaction models.

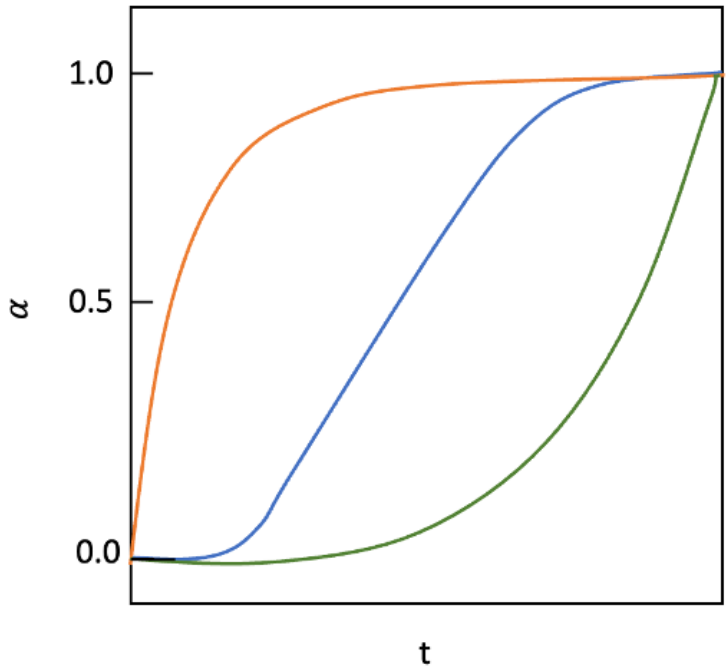

Figure 3-6: Conversion vs. time curves (characteristic curves) for isothermal runs for reactions models that are decelerating (orange), accelerating (green), and autocatalytic (blue).

3.2 Differential Scanning Calorimeter (DSC)

3.2.1 DSC Fundamentals

Figure 3-7: Netzsch 404 F3 DSC.

Differential scanning calorimetry (DSC) is a commonly used thermal analysis technique to determine the heat flow of a sample, whether endothermic or exothermic, across a temperature regime. The DSC model used in our work is shown in Figure 3-7 and a schematic of its internal components is shown in Figure 3-8. The heat required to raise the temperature of a sample is measured against the heat required to raise the temperature of a reference sample, as a function of temperature. The temperature range typically starts at room temperature and the maximum temperature varies among commercial DSCs, and can reach 1600°C or more, which is typically more than

what commercial TGAs can reach. As mentioned, temperature ranges above 500°C become of less value to study LIBs as that is well above the point of thermal runway.

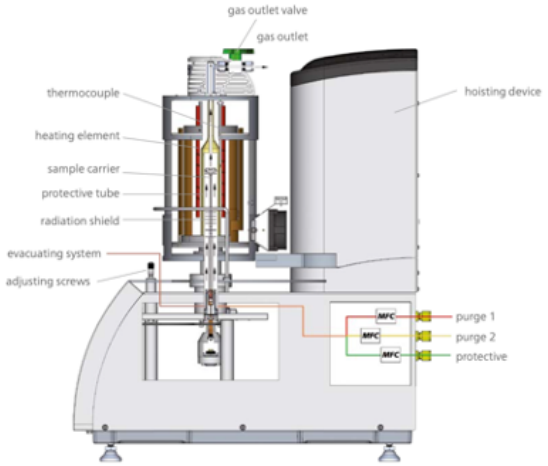

Figure 3-8: Schematic of Netzsch 404 F3 DSC. Adapted from netzsch.com.

DSC is used to measure the heat flow (heat gained or released) of a sample by heating the DSC chamber and measuring the temperature signals of the sample crucible and an empty reference crucible (see Figure 3-9 and Figure 3-10). DSC is used to study thermal decompositions and reactions of cell components (through heat flow profiles that indicate endothermicity and exothermicity). Unlike the TGA, which can only measure mass loss, a DSC can also detect constant mass interactions or phenomena such as melting (solid to liquid phase change), which does not involve mass loss.

Temperature is the only measured signal in a DSC. The heat flow is calculated from the differences in changes of temperature between a sample crucible and a reference crucible. DSC signals are more complex in analyzing than TGA signals, which only require "zeroing" the sample pan before placing the sample and obtaining mass signals. DSC signal processing require two major steps: DSC signal corrections and DSC signal calibrations.

As the furnace provides heat to the two crucibles, the sample temperature will be slightly lower than the reference temperature and reference temperature due to

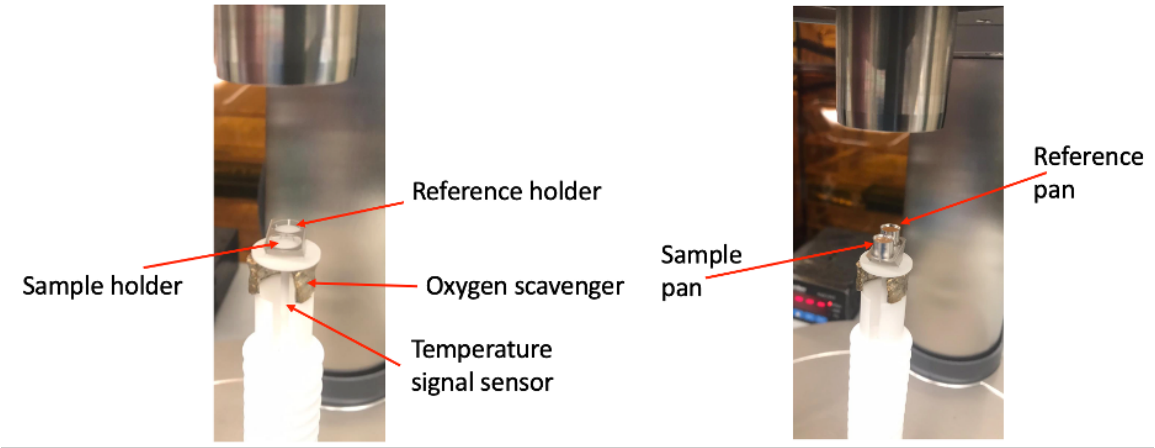

Figure 3-9: DSC apparatus sample holders.

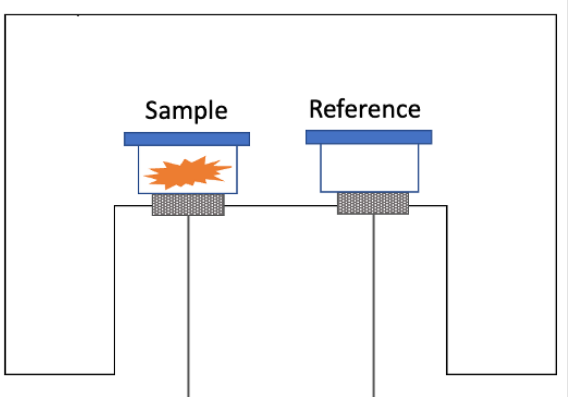

Figure 3-10: Schematic of DSC apparatus sample holders.

thermal inertia. At the start of the heating step, there will be a lag time before the sample temperature starts increasing, as shown in Figures 3-11.

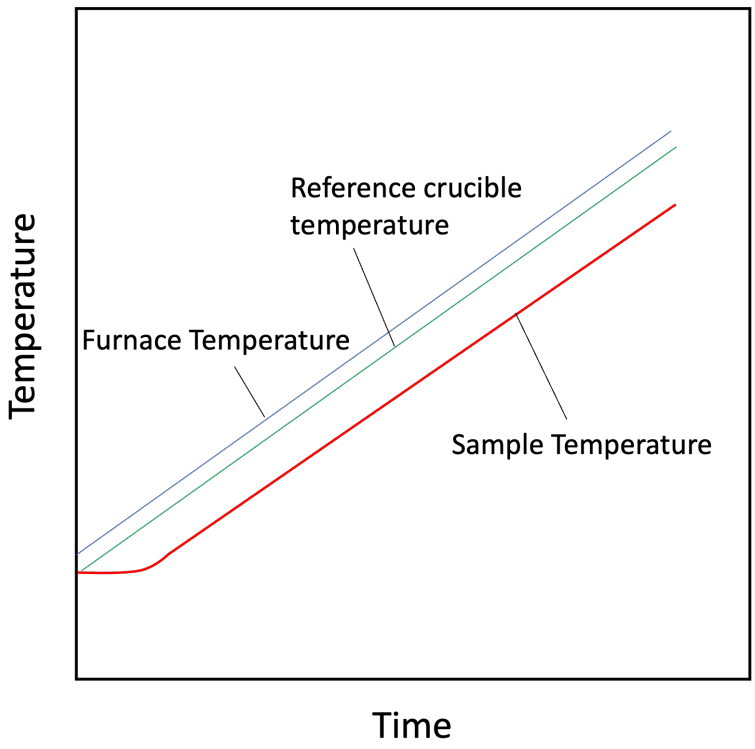

Figure 3-11: Temporal plot of temperature of furnace, reference crucible, and sample.

In the presence of an endothermic physical change such as melting or boiling, the sample temperature remains constant (kinetic energy remains constant as well) even as heat is being supplied, as the heat is used to overcome the intermolecular force of attraction between the molecules of the sample (Figure 3-12). After the physical change is complete, the temperature will resume rising as heating occurs (Figure 3-13).

In the presence of a chemical reaction, the temperature will also change depending on the endothermicity or exothermicity of the reaction.

Similar to the TGA, the material of the crucibles of choice depends on the properties of the sample and any interaction it may have with the crucibles. Unlike TGA pans which are expensive ($300 per platinum TGA pan) and not intended for single

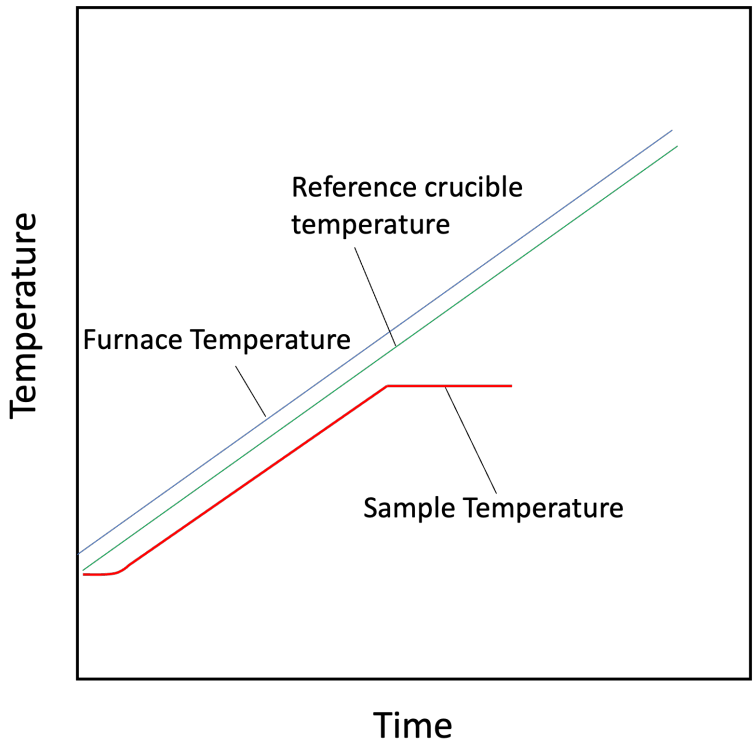

Figure 3-12: Temporal plot of temperature of furnace, reference crucible, and sample, indicating an endothermic physical change in the sample, as the temperature remains constant.

use, there are more options for DSC crucibles. DSC crucibles options include single use and multi-use crucible choices. Disposable low-pressure aluminum crucibles (Figure 3-14) were chosen for our experiments for their low cost ($3 per crucible and lid) and for the advantage of not having to clean the crucible from burned residual chemicals, given that they are single use.

DSC experiments typically examine solid and liquid state phases interactions, and not gas phase interactions. Therefore, DSC aluminum crucibles can be air-tight sealed if the sample will not gasify (and hence pressurize the sealed crucible). TGA runs are conducted on the sample of interest to determine if it will gasify at a particular temperature regime before conducting a sealed crucible DSC run on the sample. Sealed crucible DSC runs are particularly useful if the sample is sensitive to air, oxygen, or moisture. A picture of the sealing press used is shown in Figure 3-15.

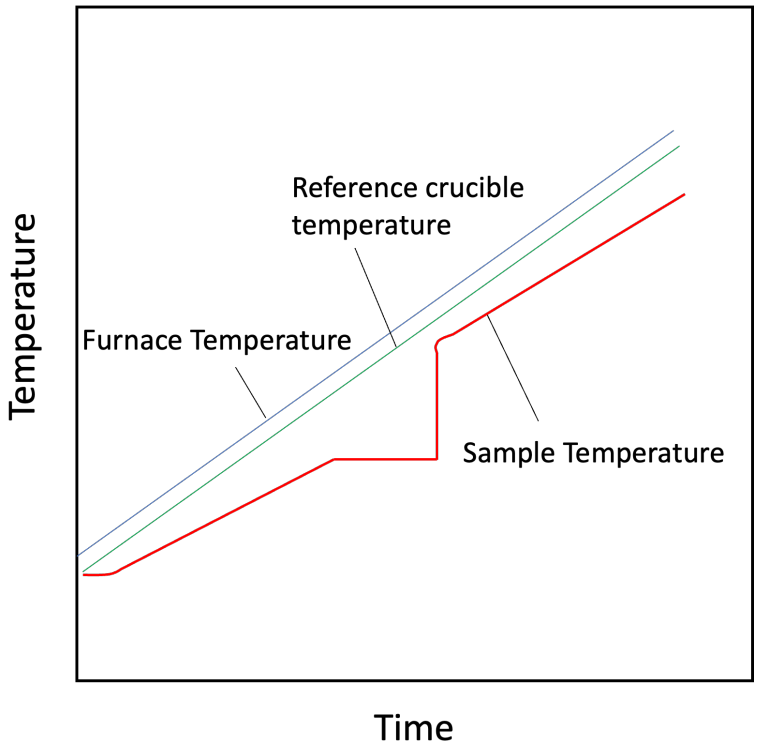

Figure 3-13: Temporal plot of temperature of furnace, reference crucible, and sample, indicating the completion of the endothermic physical change in the sample as the temperature resumes rising.

Figure 3-14: DSC aluminum crucibles and lids.

Figure 3-15: DSC sealing press for aluminum crucibles.

The sample and reference crucible are in an insulated DSC furnace chamber. The DSC furnace chamber can be enclosed, sealed under vacuum, or allow purge gases to

flow through the furnace chamber from the inlet to the exhaust (outlet).

3.2.2 DSC Signal Processing

DSC Signal Corrections

DSC signal processing require DSC signal corrections and DSC signal calibrations before a sample run can be conducted (Figure 3-16). The objective of the DSC correction experiment is to obtain DSC signals of the crucibles (noise signals), to be later subtracted from the DSC curve of a sample run. A correction experiment is run with two empty crucibles as both the reference and sample crucibles. The DSC correction step is specific to a particular heating (temperature) profile and heating rate.

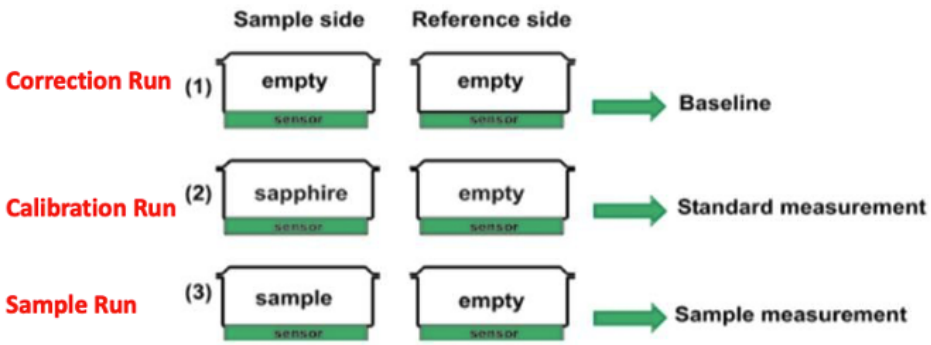

Figure 3-16: DSC measurements and processing required to obtain useful sample run signals.

In order for the DSC signal to be stable and to obtain more consistent baselines, the sample temperature control (STC) is turned off. The furnace of the DSC is large relative to the crucible size, and therefore has a large thermal inertia which can create a lag in the heating. Since the furnace is large, the heat transfer from the furnace to the sample has a lag-time. If the STC feature is turned on, the software will increase the power to the furnace since the sample will not be at the expected set point, leading to an overshoot and then relaxation of the temperature before stabilizing. With the STC turned off, the temperature of the furnace will be controlled by the thermocouple of the furnace, not the thermocouple of the sample, hence giving the

sample a more uniform heating profile.

The low-pressure sealed aluminum crucibles were subjected to six back-to-back DSC heating runs (see Figure 3-17). The furnace chamber was first loaded with the two empty low-pressure sealed aluminum crucibles (for both the sample and reference crucibles). The furnace chamber was then purged with argon gas three times. After purging with argon gas, the crucibles were subjected to six back-to-back DSC heatings. The furnace was under continuous flow of argon. The heating protocol of each of the six steps was as follows: heating rate of 5°C/min from 25°C to 375°C, followed by a cooling rate of 40°C/min back to 25°C, and finally, isothermal heating at 25°C to stabilize the baseline at a temperature at 25°C.

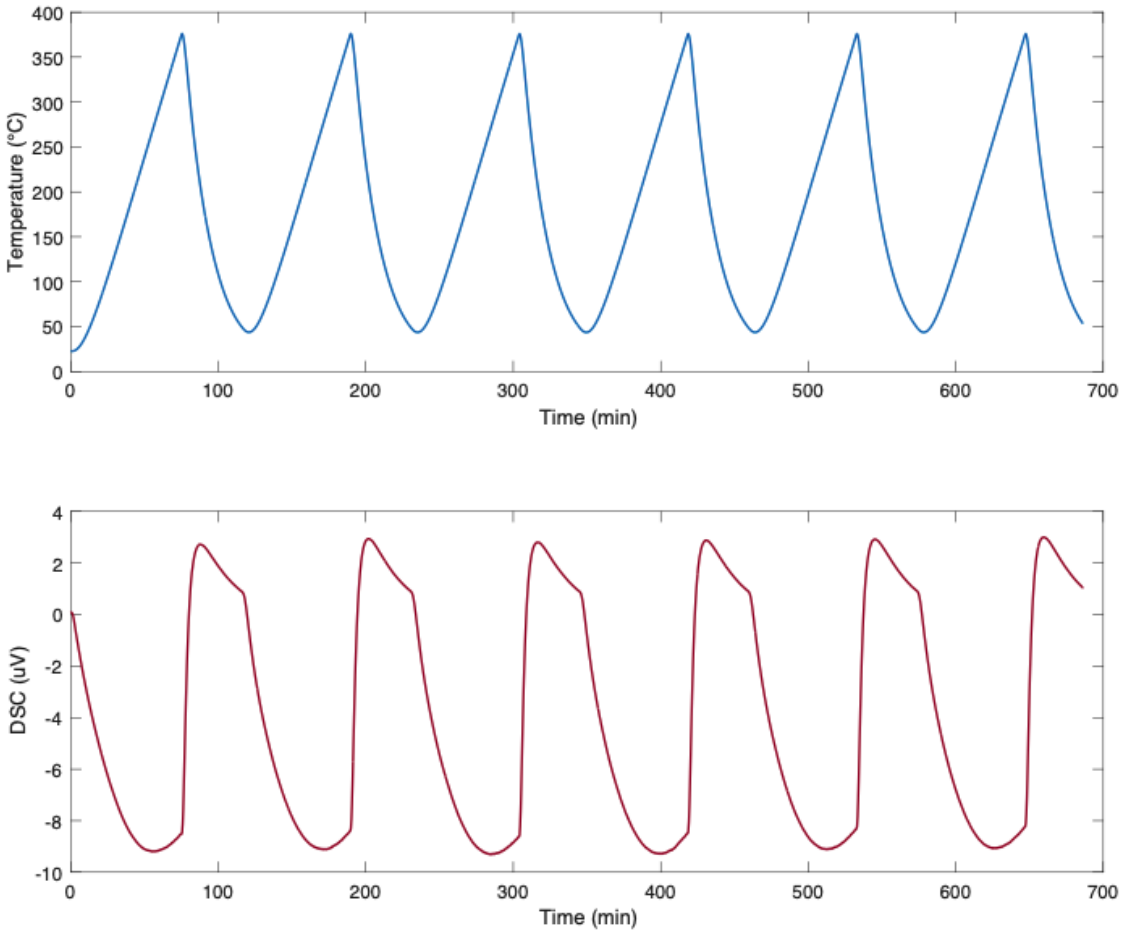

Figure 3-17: DSC correction runs with 6 back-to-back heating cycles. Temperature profile of the heating cycles (top graph) and DSC signal output of the heating cycles (bottom graph).

The signals of the heating stages were plotted in a DSC against the temperature curve as shown in Figure 3-18 and Figure 3-19. The DSC signal of the first heating is not the same as those from the remaining five heatings. This is due to small particles or impurities being present on the aluminum crucibles or in the furnace when loading. Upon heating, and with the continuous flow of argon gas, noise signals from impurities are no longer present in other runs. Other factors that can result in the first heating to not be the same include initial atmospheric pressure and humidity, or lab conditions.

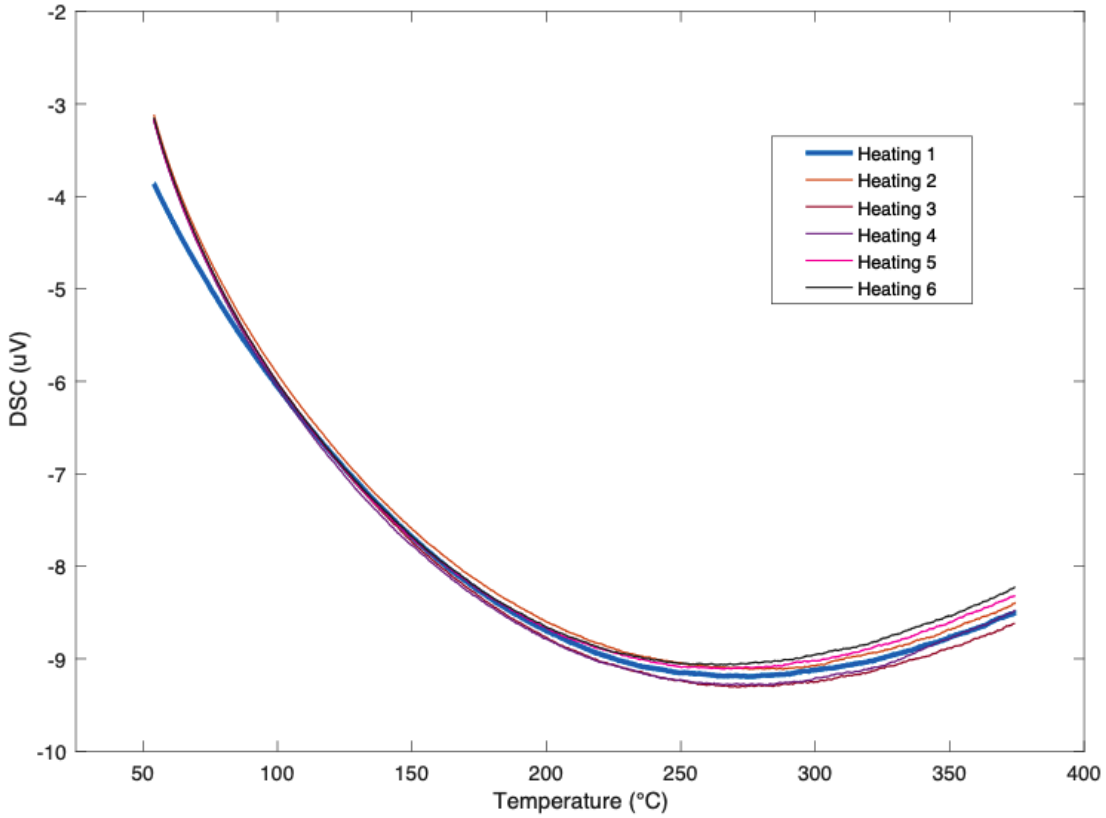

Figure 3-18: DSC correction runs with 6 back-to-back heating cycles. Temperature profile of the heating cycles (top graph) and DSC signal output of the heating cycles (bottom graph).

The average DSC signal of the remaining five heating curves is obtained and is used as a representative DSC signal correction curve to remove the effect of the aluminum crucibles, as shown in Figure 3-19.

DSC Signal Calibration

The DSC plots the difference in thermal flow between a sample and reference crucible. The DSC can also be used to determine the heat capacity of a sample. However, the objective of the DSC calibration run is to convert the raw DSC signals from µV to units of heat flow in mW. This is done by using a calibration-grade material with a well-known heat capacity. Sapphire was used for calibration since it has a well-known heat capacity.

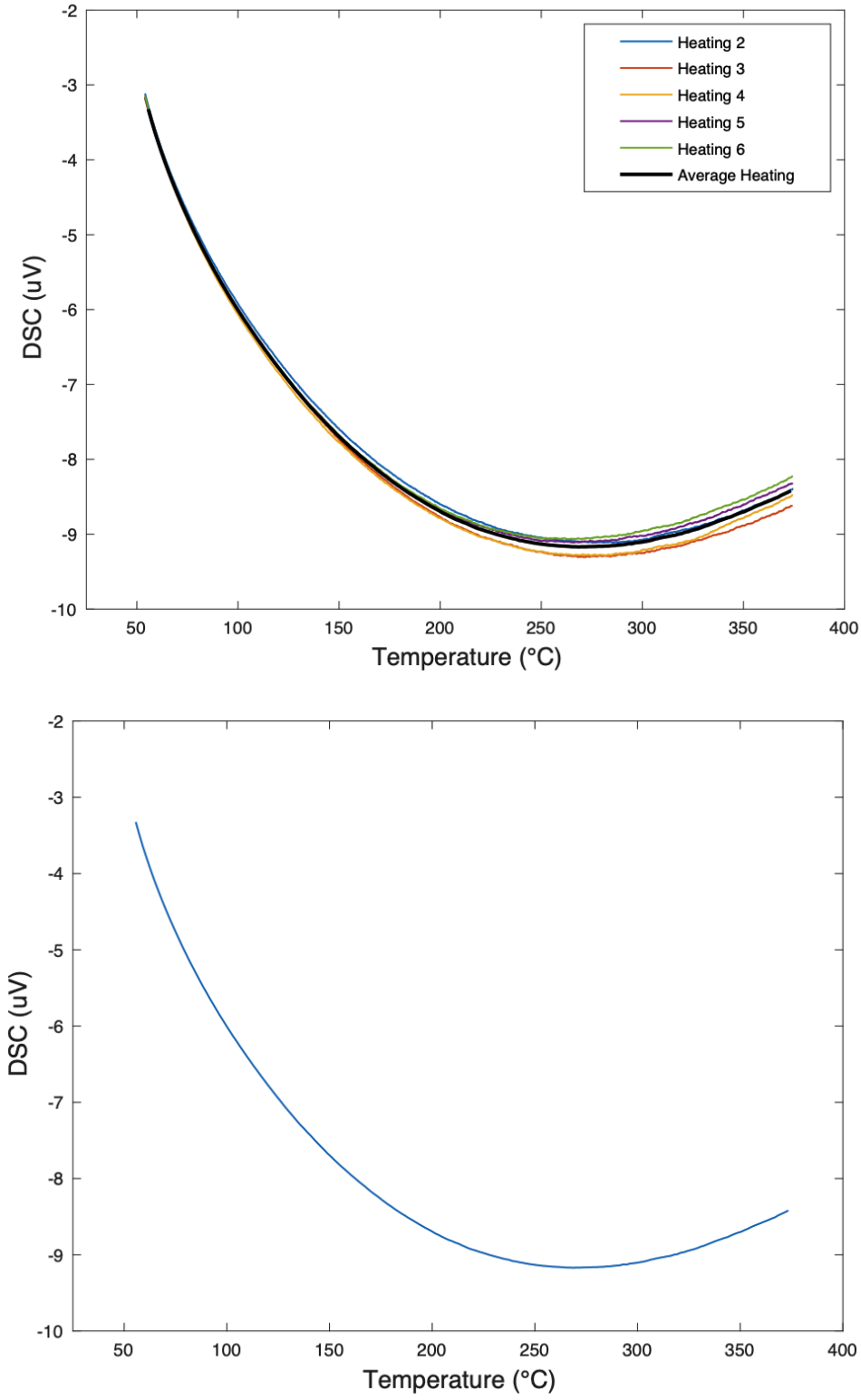

Figure 3-19: Second to sixth heating curves plotted with the average heating curve (top). (Bottom) The average heating DSC signal of empty aluminum crucibles plotted against temperature.

The mass of the sapphire was measured before the experiment was conducted, in order to normalize the signal by the mass. Sapphire was placed in sealed aluminum crucible and loaded into the DSC furnace along with an empty sealed reference crucible. In order to reduce variability, the sapphire measurement conditions have to be identical to the baseline (DSC correction run) measurement. A specific heating profile with a different correction run than presented above conducted at a larger temperature range (above 375°C, going up to 600°C) was conducted. Four back-to-back heating runs were conducted. The same heating profile was used as with the particular correction baseline run (different than what is mentioned above): heating rate of 5°C/min from 25°C to 600°C, followed by a cooling rate of 40°C/min back to 25°C, and finally, isothermal heating at 25°C to stabilize the baseline at a temperature at 25°C.

The raw DSC measurement of sapphire is corrected by subtracting the correction run (two empty crucibles) from its raw values. The resulting DSC graph is shown in Figure 3-20.

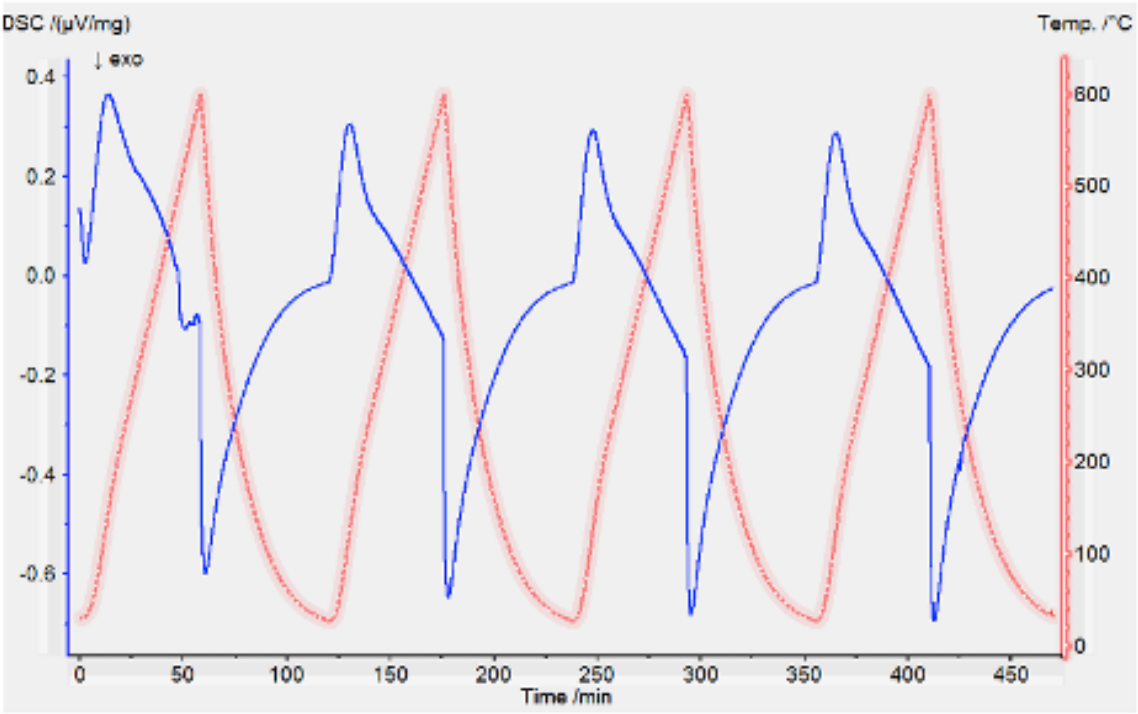

Figure 3-20: DSC measurement of sapphire, corrected for with baseline signals.

Similar to the correction runs, the first heating run involves noise and is not accounted for in the calibration curve that is constructed (Figure 3-21).

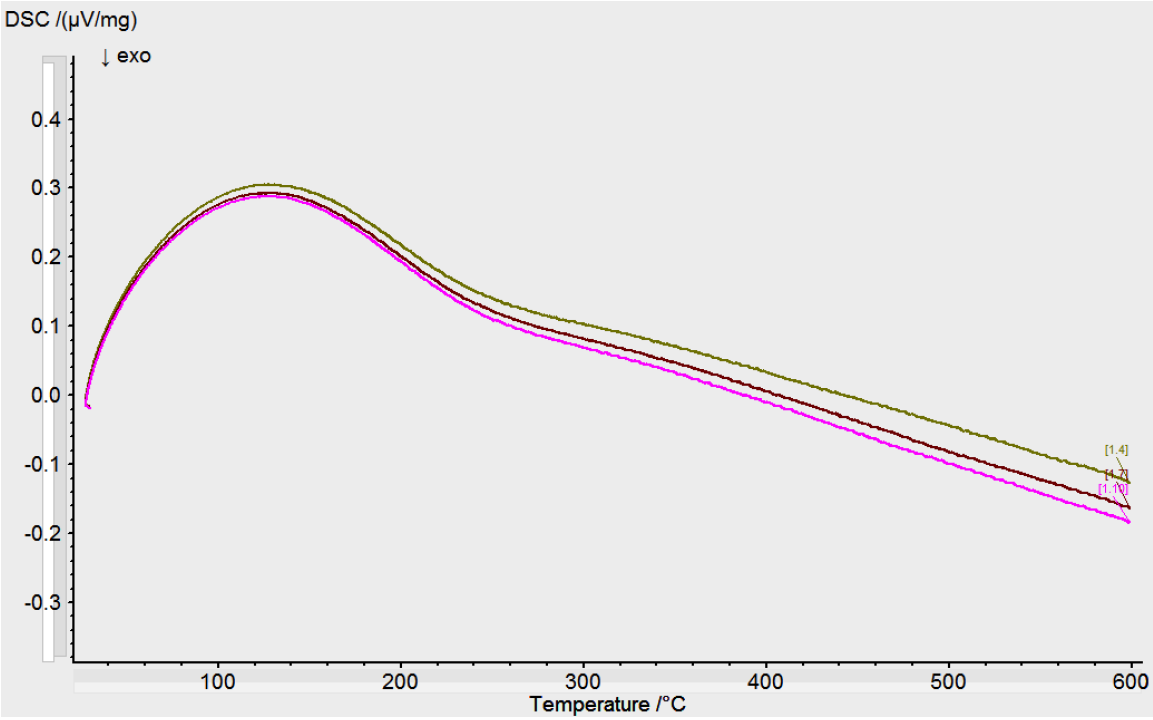

Figure 3-21: Sapphire DSC signal versus temperature (second heating in green, third heating in brown, and fourth heating in pink).

In order to obtain the calibration sensitivity (µV/ mW) curve versus temperature, the software calculated the sapphire-specific heat capacity using preset parameters for sapphire by measuring the differential of the corrected signal with respect to time at particular temperatures and dividing by the theoretical specific heat capacity of sapphire to obtain a sensitivity. The calculated sensitives at particular temperature points are plotted with their respective trend lines, as shown in Figure 3-22.

A recommended practice of obtaining *calculated* sensitivity plots for DSC measurements is removing the first two calculated sensitivity points. Moreover, as shown in Figure 3-18, the calculated sensitivity points at temperatures above 400°C diverge from the downward sloping plot. However, that is less relevant since the temperature regime of interest for LIB safety is below 400°C, therefore calculated sensitivity points above 400°C were also not included in the *calculated* sensitivity plot.

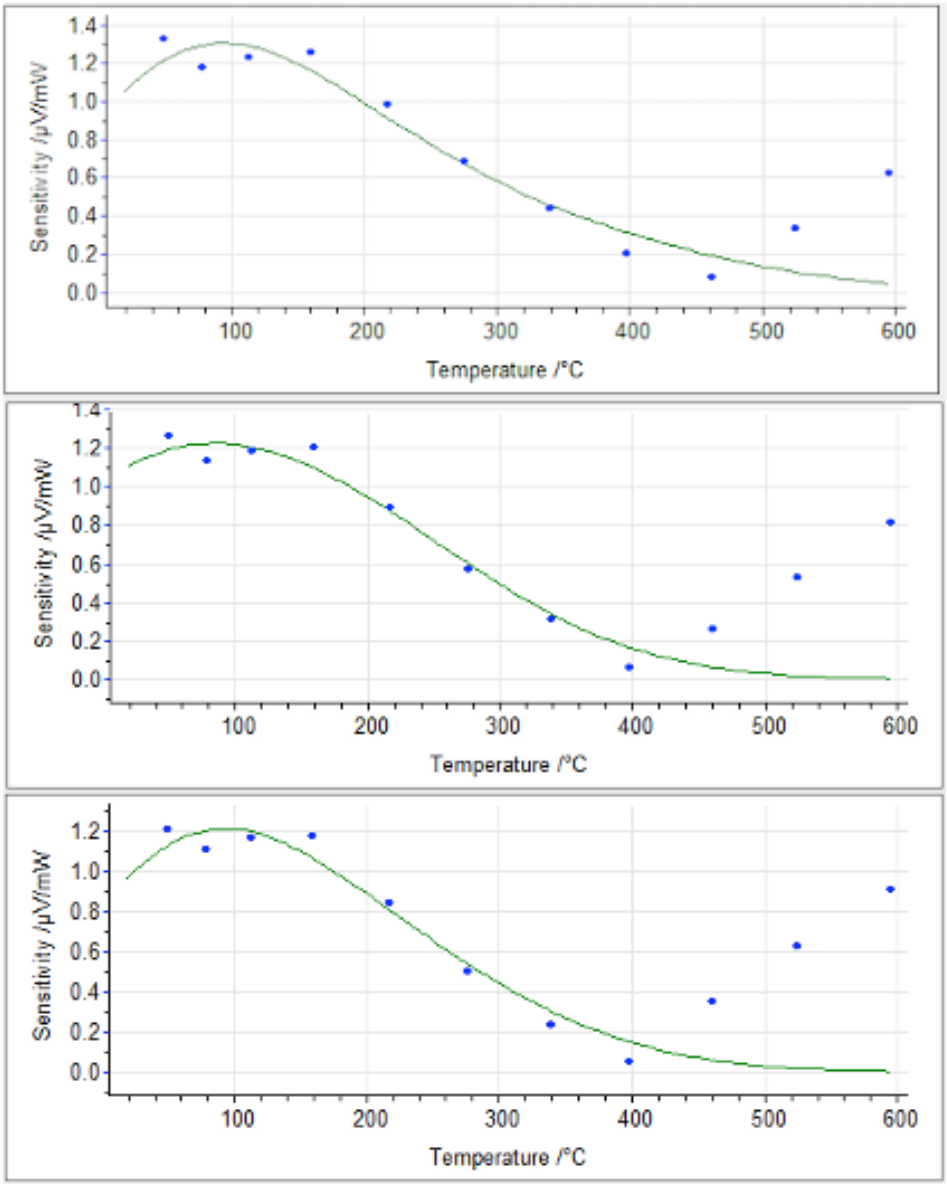

Figure 3-22: DSC sensitivity versus temperature, with calculated sensitives (blue points) and their respective trend lines (green lines) plotted. (Top) Second heating. (Middle) Third heating. (Bottom) Fourth heating.

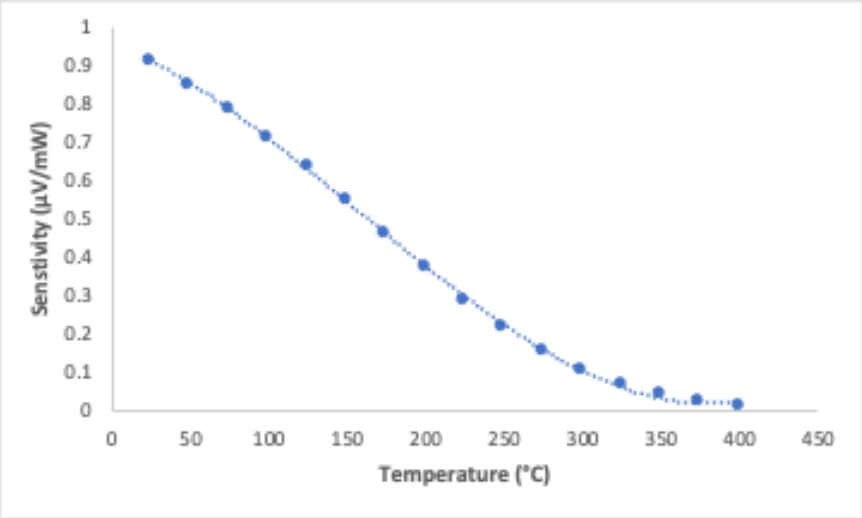

Figure 3-23: Equipment sensitivity versus temperature.

From the equipment sensitivity plot (Figure 3-23), the correct DSC signal that is in units of µV or µV/mg can be converted into units of heat flow (mW or mW/mg) by dividing by the sensitivity.

3.2.3 Physical and Chemical Properties from DSC Experiments

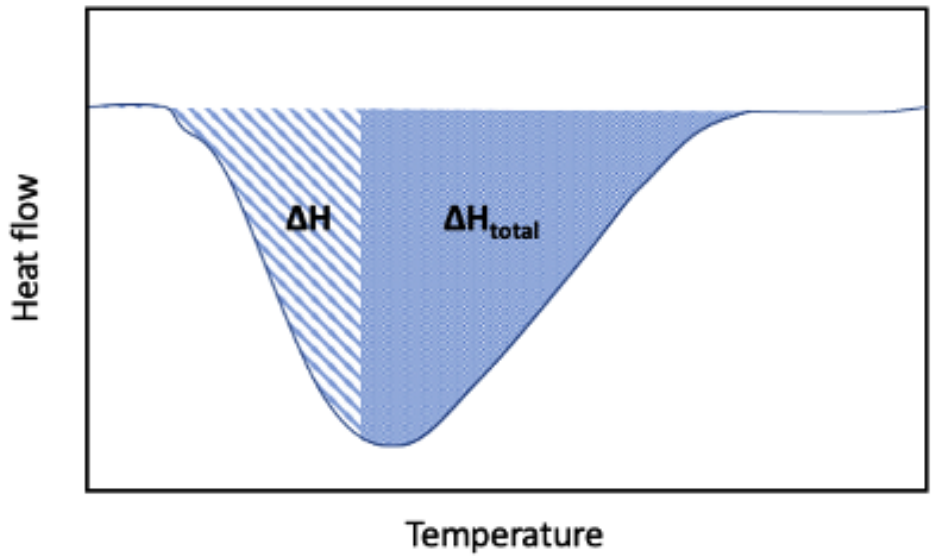

Figure 3-24: DSC heat flow versus temperature indicating a trough.

The DSC can provide useful information regarding the heat transfer of the sample - heat gained or dissipated by the sample with respect to temperature. This is done by integrating the heat flow with respect to *time* (not temperature). The area underneath the heating curve corresponds to the heat dissipated or gained. Note that it is customary in literature to plot and highlight heat flow against temperature rather than time, as that is more insightful.

Similar to the TGA, the DSC can be used to study the extent of conversion, α, of a given step by the measurement of the heat gained or dissipated (Figure 3-24).

$$\alpha = \frac{\Delta H}{\Delta H_{total}} \tag{3.6}$$

The DSC is most commonly used to study the physical behavior of glass and polymers at varying temperatures, as shown in the example plot in Figure 3-25. The DSC is less commonly used to study chemical reactions or thermal behavior of more

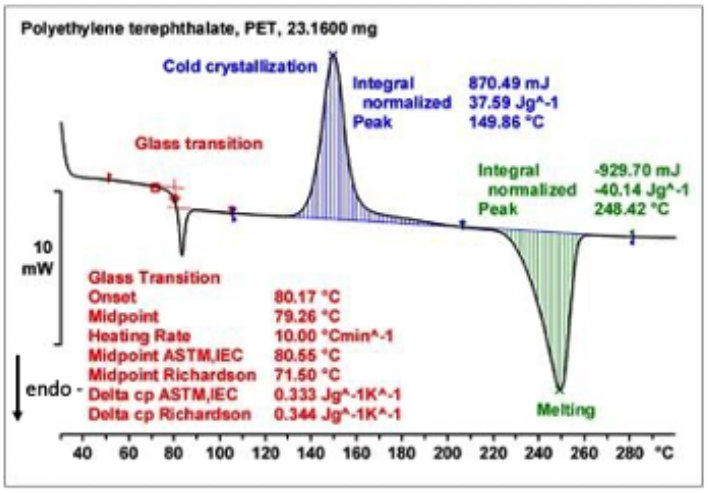

Figure 3-25: Example DSC curve showing phase change including crystallization and melting.

"dynamic" and heterogenous chemical species such as LIB components.

3.2.4 Integration of TGA and DSC

The TGA and DSC were both used to study individual cell components. DSC runs can be conducted with sealed or unsealed crucibles. In order to prevent over-pressurization, and in order to limit exposure with oxygen in the air during sample loading and unloading, a compromise was made by using sealed crucibles with a pinhole (to prevent pressure build-up).

In order to mimic the DSC furnace environment, TGA runs were conducted on samples placed in a DSC crucible (with a pinhole) that were placed in the TGA pan. To prevent reaction with oxygen, the atmosphere in both the TGA and DSC furnaces were purged with pure argon throughout the experiment. Once a mass-temperature profile is obtained in the TGA, DSC heat-flow over temperature profiles can be normalized by the actual mass in the crucibles.

3.3 Accelerating Rate Calorimeter (ARC)

An apparatus commonly used to understand the thermal safety of portable electronic devices is the accelerating rate calorimeter (ARC) (Figure 3-26). ARC is used to induce a thermal runaway on the sample and to analyze its behavior. Unlike the TGA and DSC which are used to study samples of small sizes (typically $<$ 1.00 grams), the ARC is a larger piece of equipment that can handle large sample sizes with chamber sizes that can go up to 50 x 50 cm with a working volume of 2 m^3. ARC can be used to study the thermal behavior of a full cell and even multiple batteries as opposed to DSCs and TGAs that can only be used to study cell components.

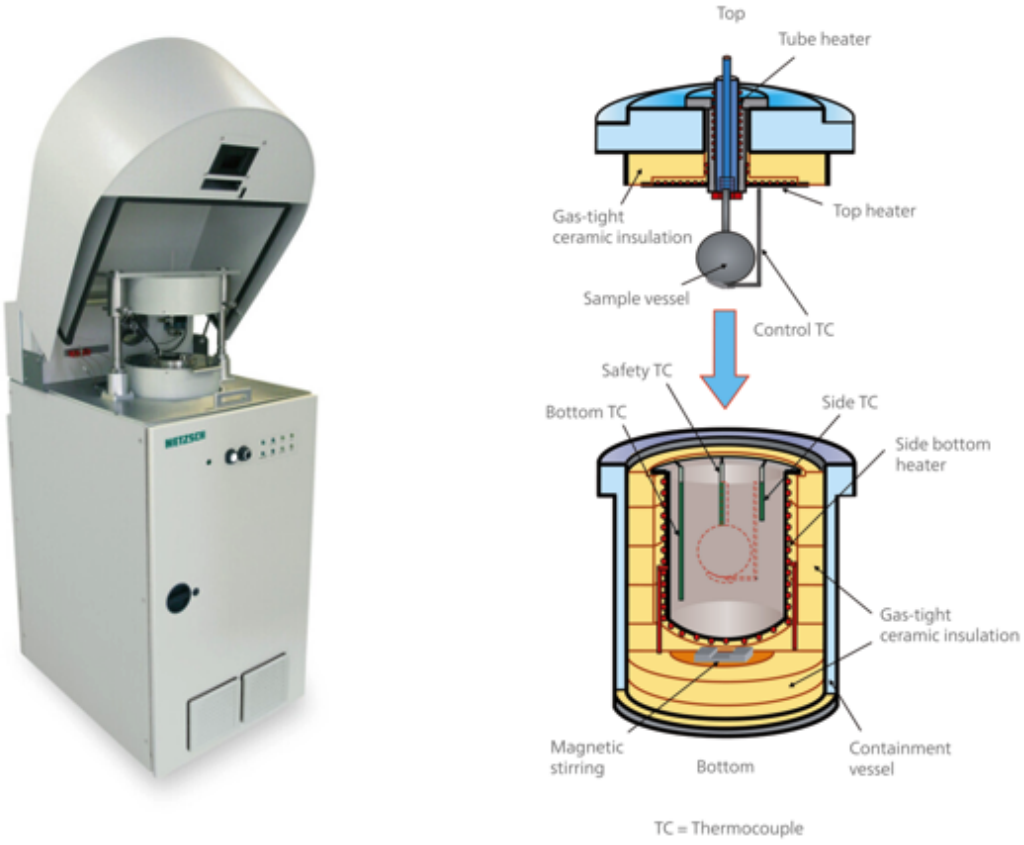

Figure 3-26: Netzsch 244 ARC and a schematic of the interior of the furnace chamber. Adapted from [1].

The first step in inducing a thermal runaway is reaching the on-set temperature of thermal runaway. Through adaptive adiabatic control, the ARC determines the on-set

temperature using a heat-wait-seek protocol that gradually increases the temperature of the chamber (typically in 5°C/min intervals), then holding the chamber under adiabatic conditions, and waiting to detect an exotherm. The wait time is either until an isothermal equilibrium is achieved or set at an intermediate wait time such as 20 min. The ARC seeks a particular self-heating temperature increase rate of the sample. If the self-heating temperature increase rate of a sample exceeds a cutoff (typically set at 1°C/min), that is defined to be the onset temperature of thermal runaway. The ARC is programmed to stop the heating of the sample and to achieve a solely adiabatic environment in the chamber. This allows the simulation of a worst case scenario where the heat released from the sample is used to further increase the temperature of the environment as there is no dissipation of the released heat. An example of an ARC temperature profile is shown in Figure 3-27.

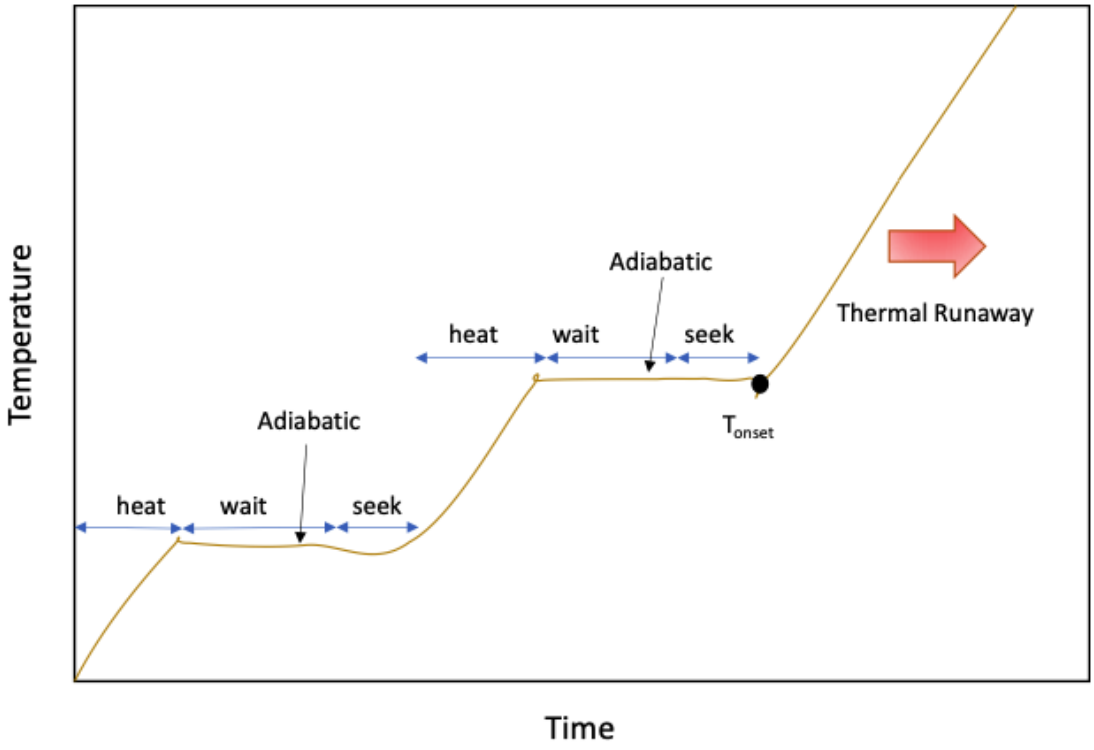

Figure 3-27: ARC temperature profile.

ARC experiments are powerful in understanding the net interactions in a cell. As shown in Figure 3-28, different components of the cell may even have a higher onset temperature than the full cell (battery) onset temperature[39]. This shows the

complexity of thermally studying system that undergoes many chemical (& electrochemical) and physical (phase) changes.

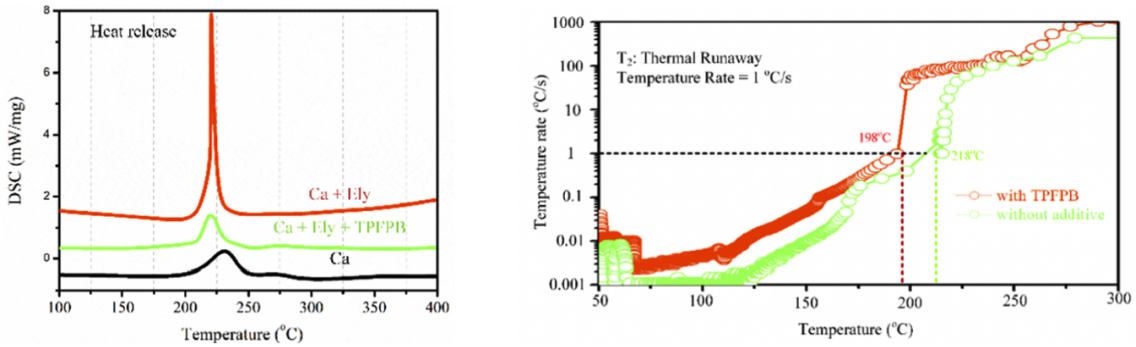

Figure 3-28: A studying comparing the thermal properties of a LIB with a "low flammability" electrolyte (1:1.9 LiFSI/DMC) and a conventional electrolyte (1M $LiPF_6$ EC:EMC) also demonstrated that the full cell interactions can be more stable (have lower onset temperature) than different components together[39].

ARC and DSC are fundamentally different techniques, and the contrast in data (for example, showing TPFPB to decrease cathode+electrolyte heat release but also decrease onset temperature) should not be alarming due to the numerous interactions (reactions) and complexity of the LIB system. These two techniques are complimentary. ARC is more insightful when conducted to determine the overall cell self-heat onset temperature, while DSC is important in understanding interactions of components of the cell. What the contrast in data shows is that it is not straightforward to enhance the overall thermal stability of a LIB due to the complexity of its interactions.

Chapter 4

Results and Discussion

LIB samples are highly sensitive to oxygen, moisture, and air, making their thermal analysis difficult. To prevent unwanted reactions, all LIB samples for thermal analyses were prepared in an argon-filled glovebox, transferred to gas-tight vials, and subjected to thermal tests in controlled environments. To understand the limitations of the equipment used, initial experiments were conducted on the well studied $LiMn_2O_4$ cathodes. TGA shows that decomposition onset temperatures shift higher with increased heating rates, and charged LMO samples decompose faster than uncharged ones, with variations in decomposition related to charge cut-off voltages. Proper drying was determined to be essential for accurate TGA results, as residual electrolytes can skew readings. Thermal analysis conducted on the SEI highlighted the significant challenges due to its reactivity, sensitivity to environmental conditions, and fragile nature. Attempts to conduct such analysis in this study proved inconclusive, underscoring the complexity of examining the SEI layer. Investigation of the well-studied $LiPF_6$ salts and their interactions at different concentrations of solvent highlighted the interplay between the boiling point elevation colligative property and the chemical reactivity.

Leveraging the knowledge learned from the experiments, we introduce a standard-

ized experimental protocol integrating TGA and DSC for in-depth LIB thermal analysis. Using sealed crucibles with pinholes, we present a comprehensive thermal profile of next-generation LiFSI-based electrolytes, revealing behaviors that differ based on solvent choice. Our analysis discerned distinct thermal properties between LiFSI-carbonate and LiFSI-ether electrolytes. Specifically, carbonate-based electrolytes displayed a pronounced exothermic peak at 350°C, indicative of significant decomposition reactions. In contrast, the LiFSI-ether electrolyte exhibited an exothermic reaction at 210°C, followed by an endothermic event near 300°C. The results showcase varied thermal behaviors when LiFSI interacts with different electrolyte systems, underlining the electrolyte's influence on a battery's thermal stability.

4.1 LIB Samples Sensitivities

LIB samples are well known to be sensitive to oxygen, moisture, and even air. Lithium is a highly reactive element. When exposed to air, it can react with oxygen, nitrogen, and even carbon dioxide in the atmosphere to form lithium oxide, lithium nitride, and lithium carbonate[41]. These reactions can degrade the performance of the battery. In the presence of moisture, lithium reacts to form lithium hydroxide and hydrogen gas. The hydrogen gas can create a fire or explosion risk[41]. Cathode materials and the organic solvents used in the electrolyte can react with moisture in the air, leading to material degradation and poorer battery performance.

Therefore, handling LIB materials has to be done meticulously and it is essential to minimize exposure to air and moisture. All LIB samples used for our thermal analyses were prepared in an argon-filled glovebox to ensure an oxygen-free environment and prevent any unwanted reactions or contamination. The glovebox provides a controlled atmosphere with low levels of moisture, oxygen, and other impurities, which is essential for maintaining the stability and integrity of the LIB components. After the LIB samples were prepared inside the glovebox, they are carefully transferred into

a gas-tight vial to preserve their chemical composition and prevent any exposure to ambient air. The use of a gas-tight vial ensures that the LIB samples remain isolated from the external environment, maintaining the inert atmosphere and preventing any undesired reactions or moisture absorption. The only exposure the samples have is during the sample loading process into the TGA or DSC where it is unavoidable to load without being in ambient air. The TGA and DSC furnaces are constantly purged with argon during all experiments.

In all TGA experiments, platinum pans were used, and argon gas was chosen as the sample gas. The flow rate of the argon gas was set at 90 mL/min. Additionally, nitrogen gas was used as the balance gas, with a flow rate of 10 mL/min. Platinum pans were chosen due to their high temperature compatibility, chemical resistance, stability, and inertness, making them suitable for withstanding the harsh conditions encountered in thermal analysis. Similarly, argon gas was chosen as the sample gas, creating an inert atmosphere in the TGA furnace and preventing undesired reactions between the sample and the atmosphere. Each unique experiment was conducted 3 times to ensure repeatability and reproducibility.

4.2 LMO Cathodes

LIB cathode active materials (CAM) can be divided into several categories, including lithium cobalt oxide (LCO), lithium manganese oxide (LMO), lithium nickel cobalt aluminum oxide (NCA), and lithium iron phosphate (LFP), among others. The reactivity of LIB CAM can be influenced by a variety of factors, including their purity, crystal structure, particle size, and exposure to moisture[43]. Impurities or defects in the CAM can promote unwanted reactions and decrease its overall stability, while larger particle sizes can lead to increased surface area and reactivity. An exposure to moisture or other oxidizing agents can accelerate the breakdown of the CAM and potentially lead to safety hazards[43].

Spinel $LiMn_2O_4$ (LMO) is a commonly used cathode active material in LIBs due to its high theoretical capacity and relatively low cost. It has a three-dimensional structure that provides a well-connected framework for the intercalation and de-intercalation of Li^+ during the discharge and charge of the battery. It has gained traction given that manganese is more abundant and less expensive than some of the other materials used in LIB cathodes, such as cobalt and nickel. When $LiMn_2O_4$ is uncharged in a LIB, Li^+ are intercalated into the crystal structure of the material, resulting in the material undergoing a phase transformation and an increase in the lattice constant of the crystal structure. When $LiMn_2O_4$ is charged, it does not contain any Li^+ within its crystal structure.

TGA experiments were conducted on LMO in order to understand the thermal decomposition as it progresses with temperature, as it is crucial for predicting and improving the safety of LIB, especially under conditions of thermal abuse. The TGA pan was calibrated ("zeroed") before the TGA pan was placed in the glovebox and the sample was loaded in it. To minimize exposure time to ambient air, inside the glovebox, the sample was loaded into the TGA pan and placed in a vial that was sealed and then transported outside the glovebox to the TGA station. Once the sample was loaded, the furnace that enclosed the sample was purged with argon gas at a flowrate of 90 ml/ min continuously throughout the experiment. Therefore, there is only a limited exposure time of the sample to air during the pan loading process. The exposure time is around 0.5 minutes.

4.2.1 LMO TGA Under Different Heating Rates

LMO cathode samples, charged to 4.8 V, were subjected to TGA under various heating rates to investigate their thermal behavior and decomposition kinetics. The starting temperature was 25°C and the final temperature was 400°C. The heating rates were 5, 10, 20, and 30°C/min. Figure 4-1 shows the heating profile and the time it takes to reach 400°C under different heating rates.

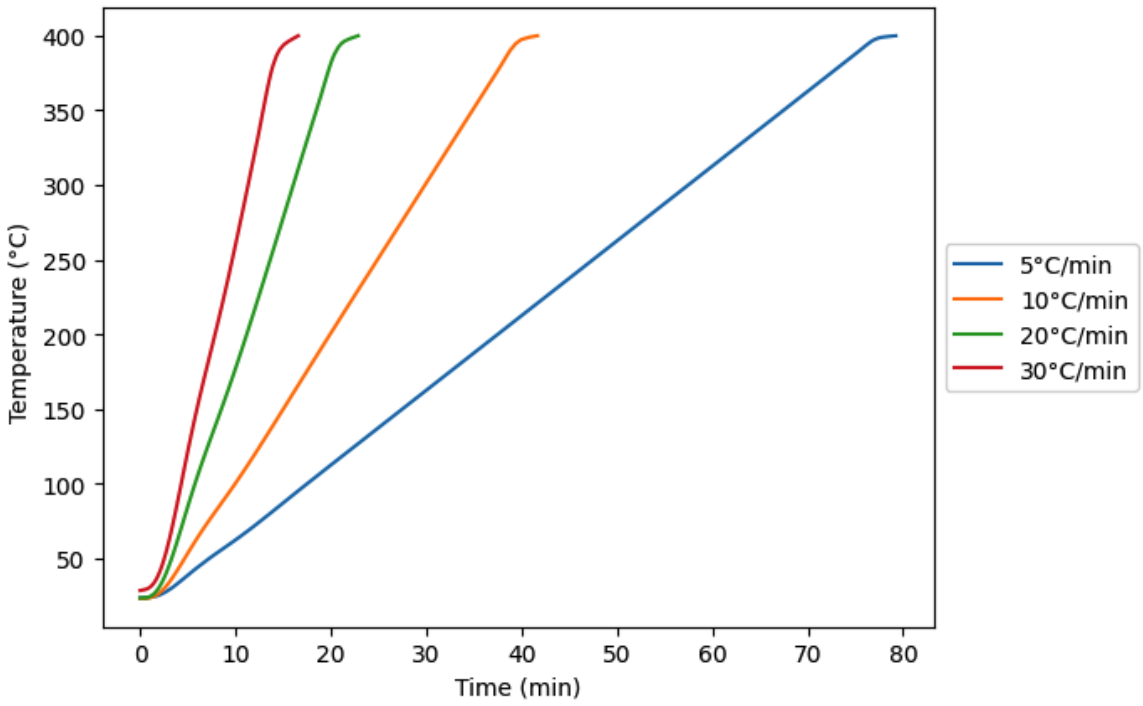

Figure 4-1: TGA heating profiles at different heating rates.

As show in in Figure 4-2, at higher heating rates, the onset of decomposition (the temperature at which decomposition begins) will shift to higher temperatures. This is due to the kinetics of the decomposition process: at higher heating rates, there is less time for the decomposition to occur at a given temperature, so it starts at a higher temperature instead.

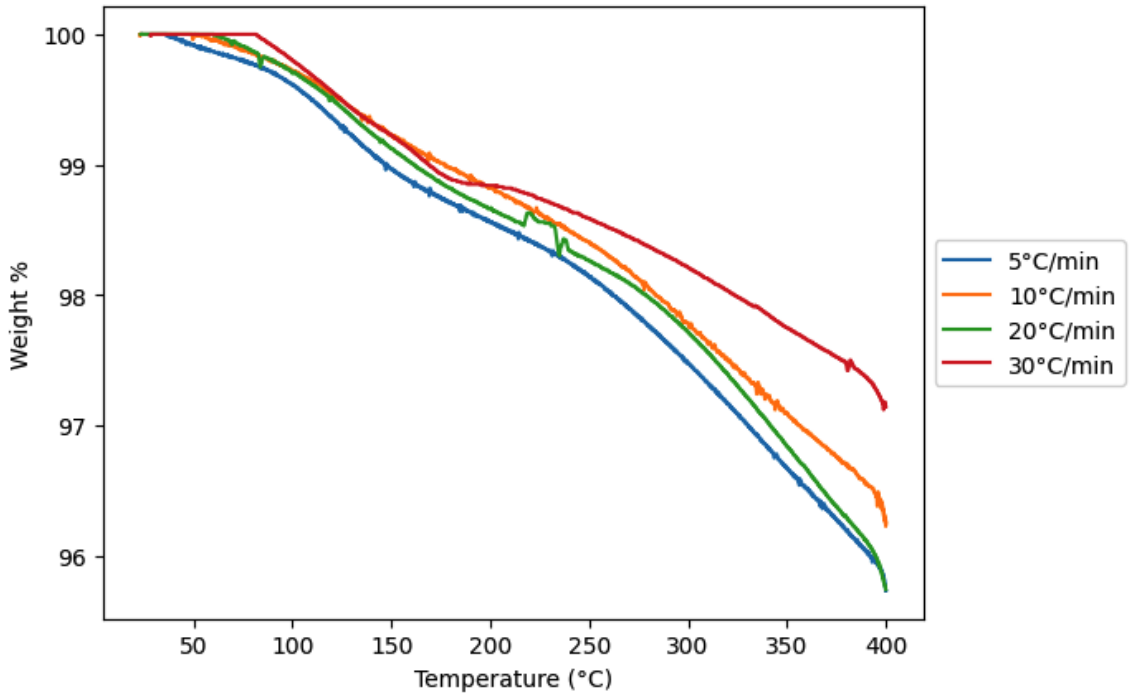

Figure 4-2: TGA weight percent versus temperature of LMO at different heating rates.

Plotting weight percent against time (Figure 4-3) shows that for higher heating rates, while it takes shorter time for a sample to reach 400°C, the sample does not achieve the weight loss as it would under lower heating rates. This provides insight on how decomposition reactions take time to proceed. The higher the heating rate on a sample, the less time for the decomposition reaction to occur at a given temperature point, shifting the decomposition to higher temperatures (to the right). This illustrates the interplay between temperature, time, and reaction rates in thermogravimetric analysis. These insights can help in understanding the decomposition kinetics of the LMO material and its thermal stability, which are crucial for its safe and efficient use in applications such as LIBs

Oxide decompositions involve the release of lattice oxygen[48]. In the case of LMO, the weight percent loss at 400°C, which depends on the heating rate, is between 2.5 - 4.5%. This indicates that no decomposition has yet taken place.

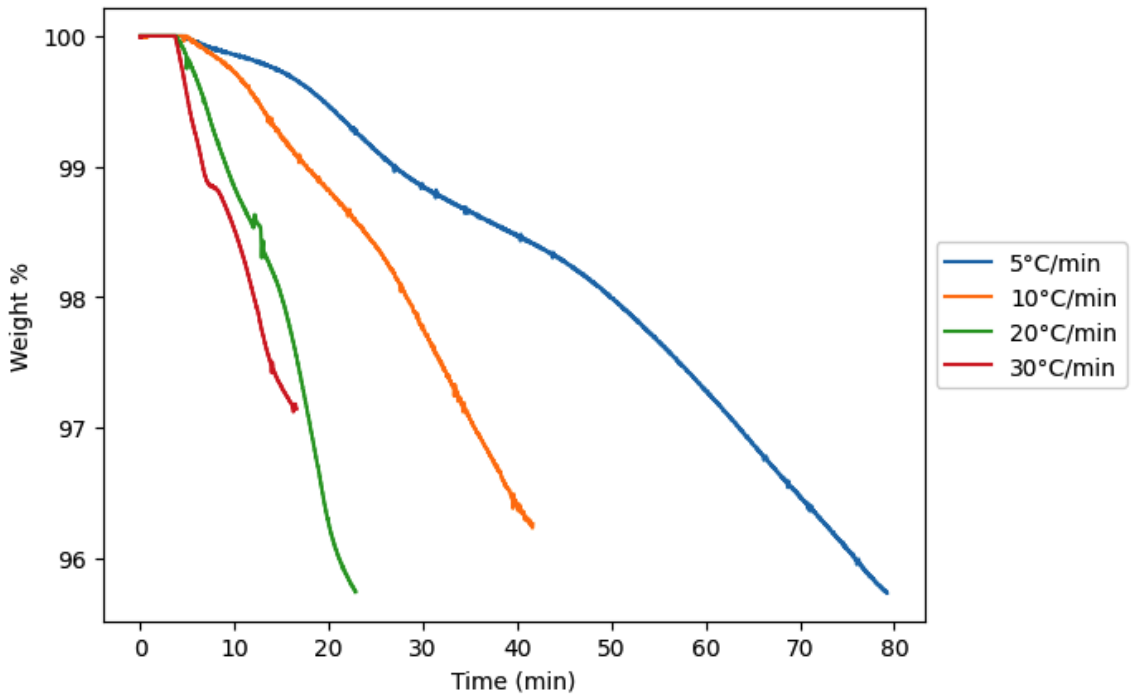

Figure 4-3: TGA weight percent versus time of LMO at different heating rates.

4.2.2 Uncharged LMO TGA

In an uncharged (discharged) LMO sample, the Li^+ are primarily intercalated within the spinel lattice. During charging, Li^+ are extracted from the lattice and move through the electrolyte to the anode. Note that while in this state, while the battery has no stored electrical energy that can be used to power a device, the LMO cathode has chemical potential energy.

A TGA run on an uncharged LMO cathode sample (with a charge cut-off voltage of 4.8V) indicates no observable mass loss (Figure 4-4). During the short exposure time of the LMO to air, the intercalated lithium may have reacted with the atmosphere to form a stable compound. The LMO sample's brief exposure to air may also have caused it to react with CO_2 to form Li_2CO_3, which starts experiencing weight loss at temperatures above 600°C[58]. The mass percent increase of 0.2% is negligible and within equipment sensitivity. Compared to the charged LMO case, the uncharged LMO has more lithium (intercalated) which reacts to form more stable compound

and hence experiences no mass loss.

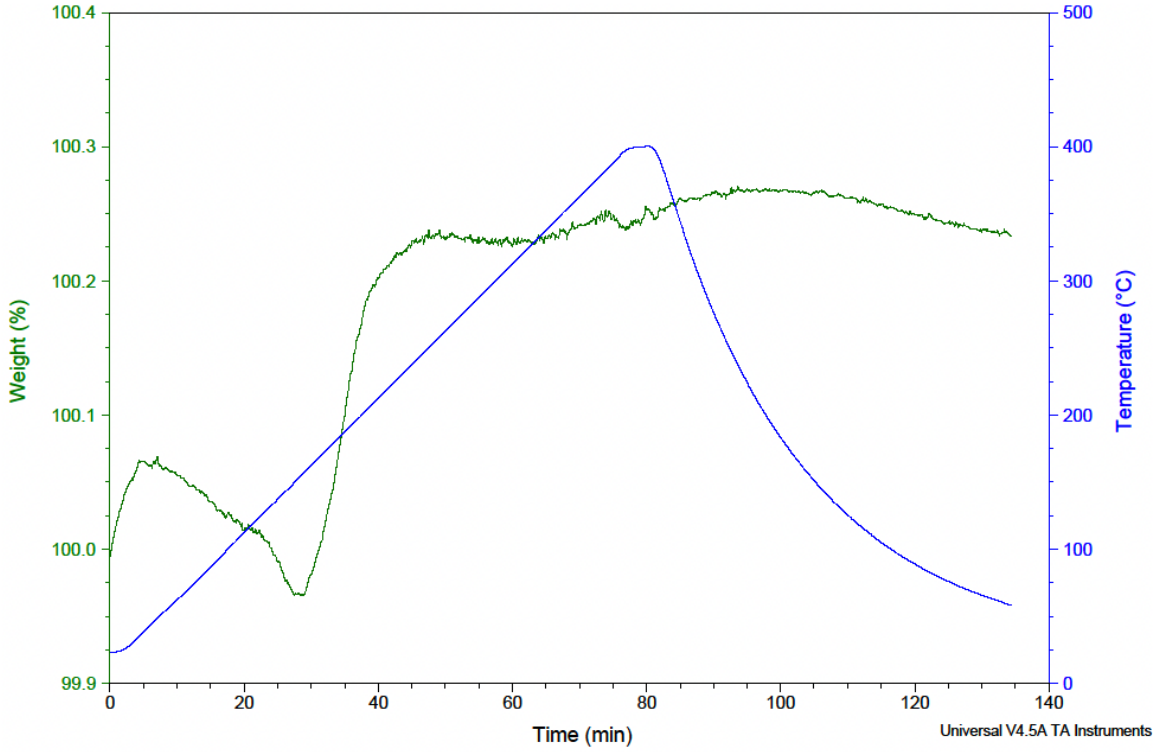

Figure 4-4: TGA profile of an uncharged LMO sample indicating weight percent (left axis – in green) versus time and temperature (right axis- blue) versus times.

4.2.3 LMO TGA Under Different Charge Cut-off Voltages

The charge cut-off voltage is the maximum voltage to which the battery is charged. The higher the charge cut-off voltage, the more energy can be stored in the battery. LMO cathode samples were charged to 4.1V and 4.8V (referring to the charge cut-off voltage). The 4.8V LMO cathodes, since they are charged to a higher voltage, have more Li^+ intercalated into the anode structure, thereby storing more energy.

TGA experiments were carried out on LMO cathodes charged to 4.1V and 4.8V, with the heating rate controlled at 5°C/min. As shown in Figure 4-5, charging to higher voltages can cause the cathode to decompose faster. The process of lithium intercalation and de-intercalation causes the LMO cathode to expand and contract. In the case of the 4.8V charged LMO LIB, the extent of this expansion and contraction is greater than that of the 4.1V charged LMO LIB, leading to subtle structural changes in the cathode structure, thereby reduce its thermal stability. Given that there is a noticeable weight loss difference of 1.5% between the 4.1V and 4.8V charged samples, and that there is no observable weight loss in the uncharged LMO sample (see Figure 4-4), we can conclude that the presence of lithium in the lattice structure of the cathode causes the cathode material to react with air to form an inert layer. This illustrates how difficult it is to analyze lithium-based samples outside of a glovebox.

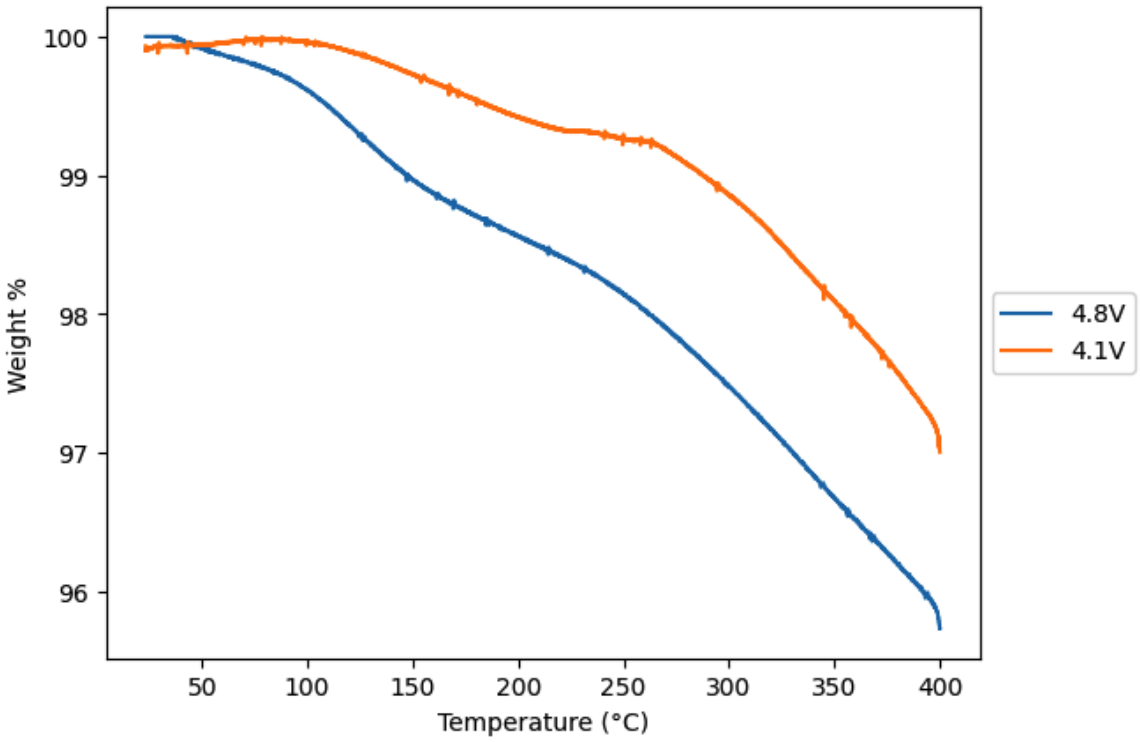

(a)

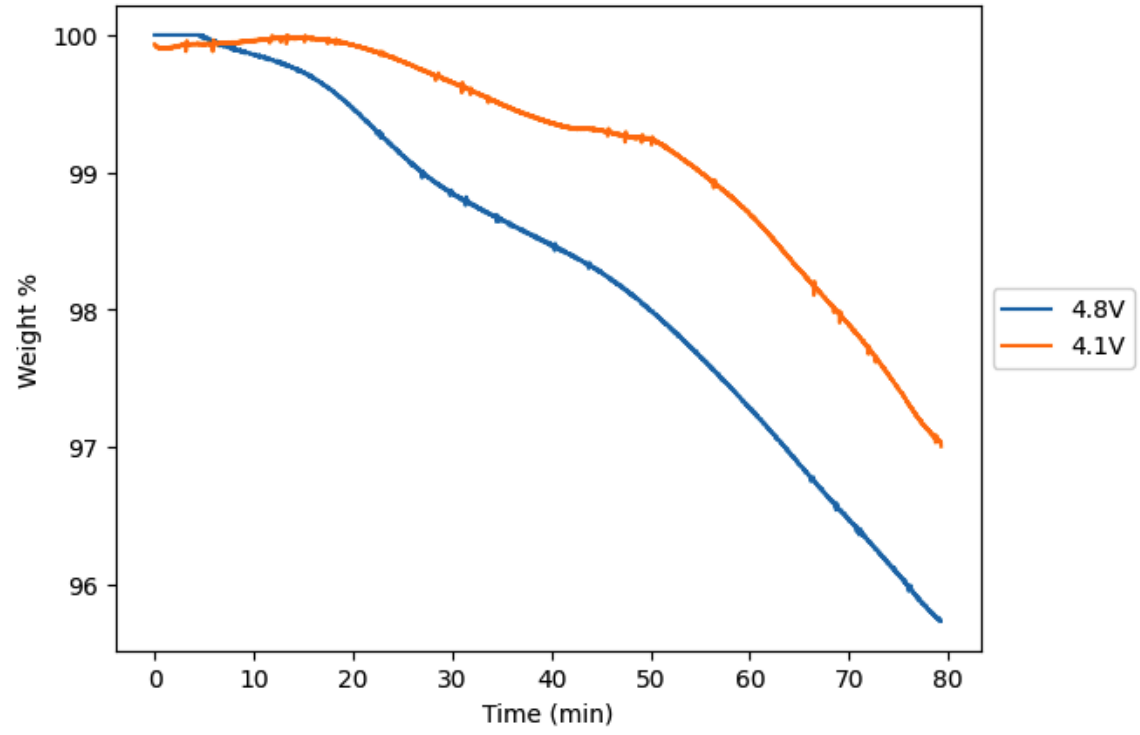

(b)

Figure 4-5: TGA plots of 4.1V and 4.8V LMO at 5°C/min. Top plot (a): weight percent versus temperature. Bottom plot (b): weight percent versus time plot.

Note on Importance of Drying Samples

Initial experiments conducted on LMO samples showed significant weight loss which was variable. This lead us to conduct multiple experiments with different charging protocols, as shown in Figure 4-6. We finally determined that the drying protocol after the cathode is disassembled from the coin cell is very important. Drying is required to ensure that no organic electrolyte, which has a lower boiling point, is present on the cathode surface. The process of vacuum drying involves placing the sample inside a drying oven which operates under vacuum, thereby reducing the pressure inside the chamber. The reduced pressure lowers the boiling point of the electrolyte, allowing it to evaporate at lower temperatures. We determined that a minimum period of 12 hours of vacuum drying was necessary for all LIB samples in order to ensure the absence of any residual electrolyte on the sample. The TGA analysis shown in Figure 4-6 showed variable (and significant) weight loss for different charging protocols because the LMO samples were not dried properly and therefore had residual electrolyte.

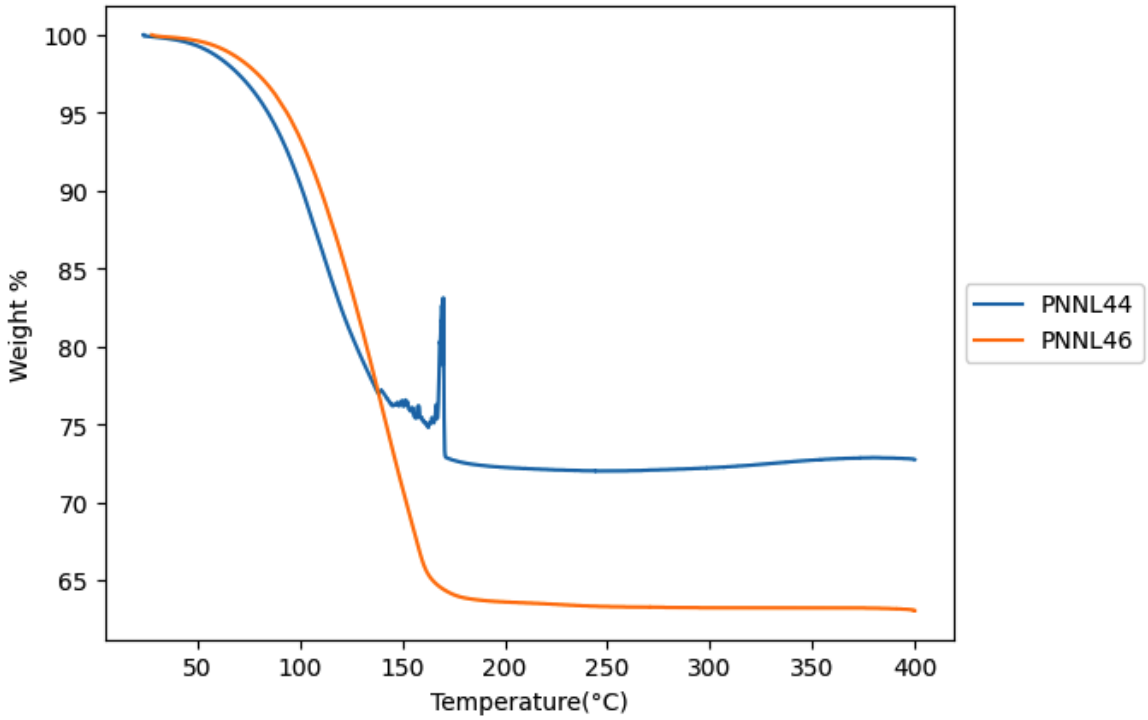

Figure 4-6: TGA on LMO with different cycling protocols: Pacific Northwest National Laboratory (PNNL)44 and PNNL46 LMO refer to charging to 4.4V and 4.6V.

4.3 Anodes

4.3.1 The Solid-Electrolyte-Interface (SEI) and its Importance

The solid-electrolyte-interface (SEI) is a passivation layer that forms on the anode surface instantaneously when the cell circuit is completed. It is formed by the decomposition of the electrolyte on the graphite anode. The SEI preserves the electrochemical efficiency of the cell by preventing interactions between the electrolyte and the anode, remaining permeable and selective towards Li^+ only. The SEI has a negligible electrical conductivity and high electrolyte diffusion resistance[24]. The presence of the SEI is essential to the high performance of the LIB; however, the SEI growth, formation, and electrochemical stability have remained active research questions. Ideal properties to the SEI would include, in addition to negligible electrical conductivity and high electrolyte diffusion resistance, insolubility in the electrolyte, and a greater

operating temperature and potential window.

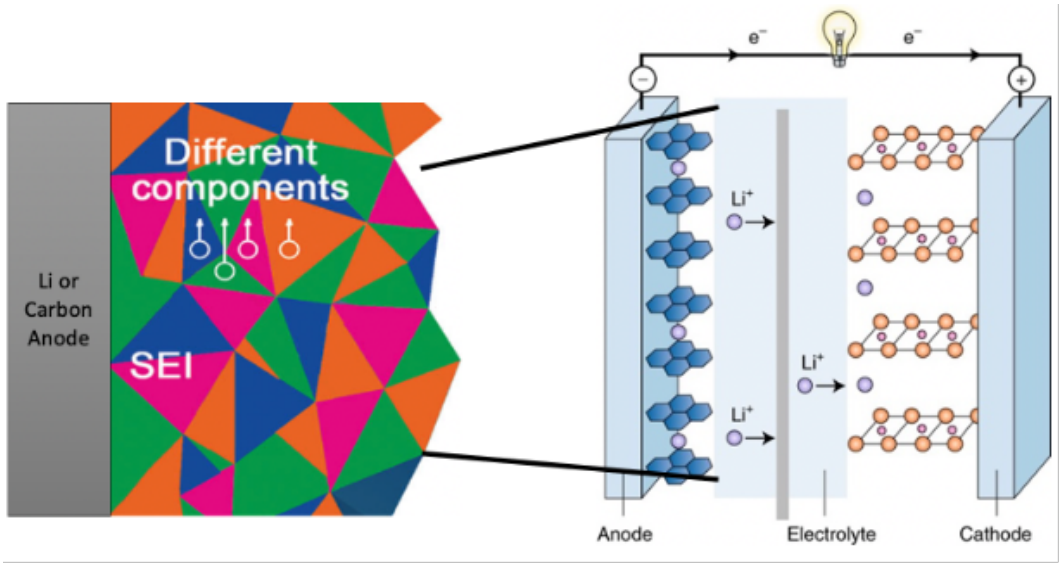

Figure 4-7: Representation of SEI. Adapted from [29].

The anode SEI is formed of precipitates of the solvent, salt, impurities, and Li given that they are instable at the anode operating potential window[36]. The SEI is primarily formed during the first charging cycle of the cell and only gradually grows until it is fully developed[24]. SEI formation is heavily absent on the cathode surface because of the high oxidation potential of the carbonate solvents found in the electrolyte[24]. Both Fourier transform infrared spectroscopy (FTIR) and X-ray photoelectron spectroscopy (XPS) have been employed to characterize the SEI. The difficulty in characterizing the SEI extends to attempting to demarcate the boundary between the end of the SEI and beginning of the electrolyte. The SEI layer is composed of stable inorganic species, primarily LiF and Li_2CO_3, and metastable organic species such as $ROCO_2Li$, $(CH2OCO_2Li)_2$, and ROLi[62, 68]. Some researchers have also claimed that Li_2O and LiOH are present at the SEI if the electrolyte is contaminated[25]. The inner layer adjacent to the anode consists mainly of inorganic species while the outer layer adjacent to the electrolyte consists mainly of organic species[62, 68, 25]. The SEI is extremely sensitive to air, humidity, and any contamination[62]. A representation of the SEI is shown in Figure 4-7.

4.3.2 SEI TGA

Since the electrolyte components form part of the components of the SEI, we decided to conduct thermal analysis of SEI's that were formed from different electrolytes: 1M Lithium hexafluorophosphate in propylene carbonate (1M $LiPF_6$ in PC) and 1M lithium bis(trifluoromethanesulfonyl) imide in 1,2-dimethoxyethane and 1,3-dioxolane (1M LiTFSI in DME:DOL).

An "anode-free" LIB was used to thermally analyze the SEI that is formed on the copper current collector. The absence of the graphite anode provides a purer environment to study the SEI, ensuring there is no influence of graphite in the thermal signals. TGA was conducted on the SEI and the copper current collector after the intercalated lithium was stripped from the copper current collector (LIB was discharged). Even when the SEI samples are stripped of lithium, the samples still have lithium compounds and are very reactive. In two instances, the TGA experiment failed as the SEI sample "popped" as soon as the argon vial was opened and exposed to the atmosphere (ambient air) in order to load the sample into the TGA. This "popping" phenomenon is due to certain components of the SEI sample reacting rapidly and exothermically with components of air.

Even though the SEI is known to have species that decompose below 100°C, the 1M $LiPF_6$ PC SEI sample showed no observable weight loss (Figure 4-8). The slight decrease in weight followed by an increase is attributed to the buoyancy effect (see Section 3.1.2), which occurs at elevated temperatures and results in an overall increase in weight. To eliminate the effect of the copper current collector, the SEI was carefully scraped off the copper current collector using a razor blade. TGA was conducted on the SEI powder, and likewise, the sample did not exhibit any weight loss (Figure 4-9).

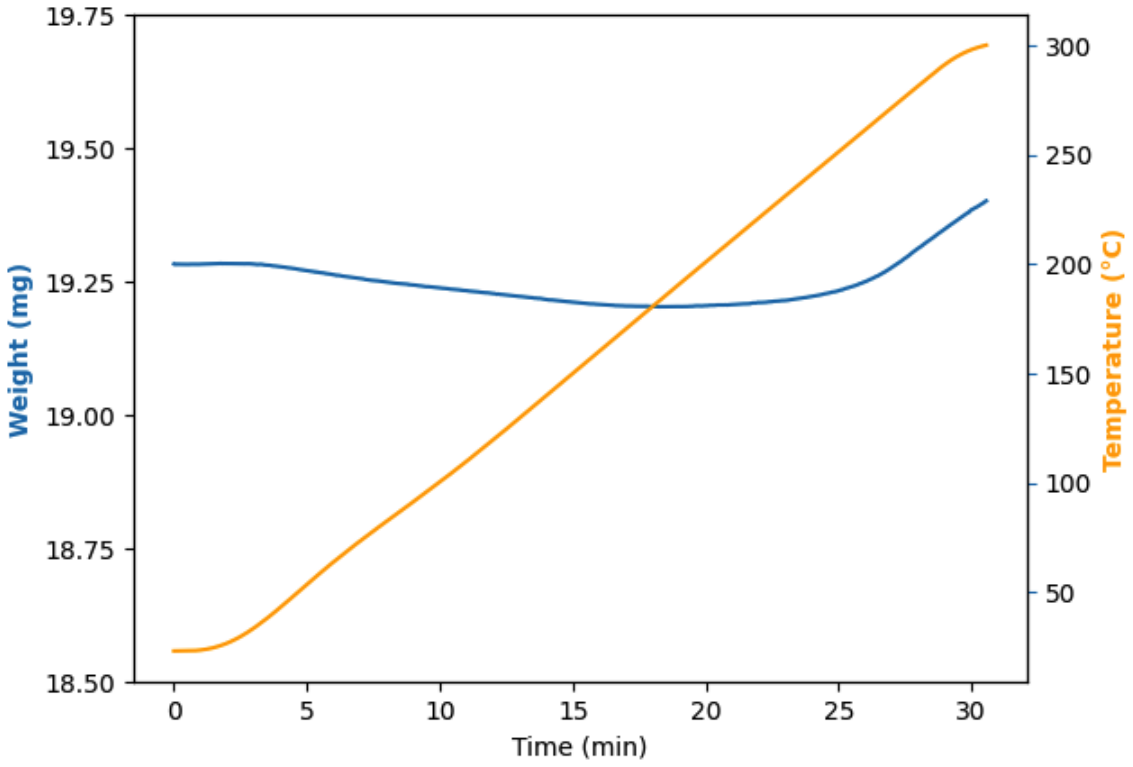

Figure 4-8: TGA on copper current collector and SEI formed in 1M $LiPF_6$ PC.

Similarly, the 1M LiTFSI DOL:DME SEI sample (which included the copper current collector) did not exhibit any observable weight loss at temperatures below 300°C (Figure 4-10). Interestingly, the sample did start to increase in weight at temperatures above 300°C. The thermogravimetric gain is substantial (increase of over 0.80 mg) and not negligible to be merely explained by the buoyancy effect. It can be attributed to several factors including the potential oxidation at elevated temperatures. While the TGA furnace is continuously purged with argon at a flow rate of 90 mL/min, it is important to acknowledge that the furnace is not at 100% perfect seal, which may allow for the entry of trace amounts of oxygen, thereby leading to potential oxidation reactions. Considering the exceptional sensitivity of the SEI, even trace levels of any non-inert gases, but also including some inert gases like nitrogen[35, 65], can significantly influence the TGA analysis.

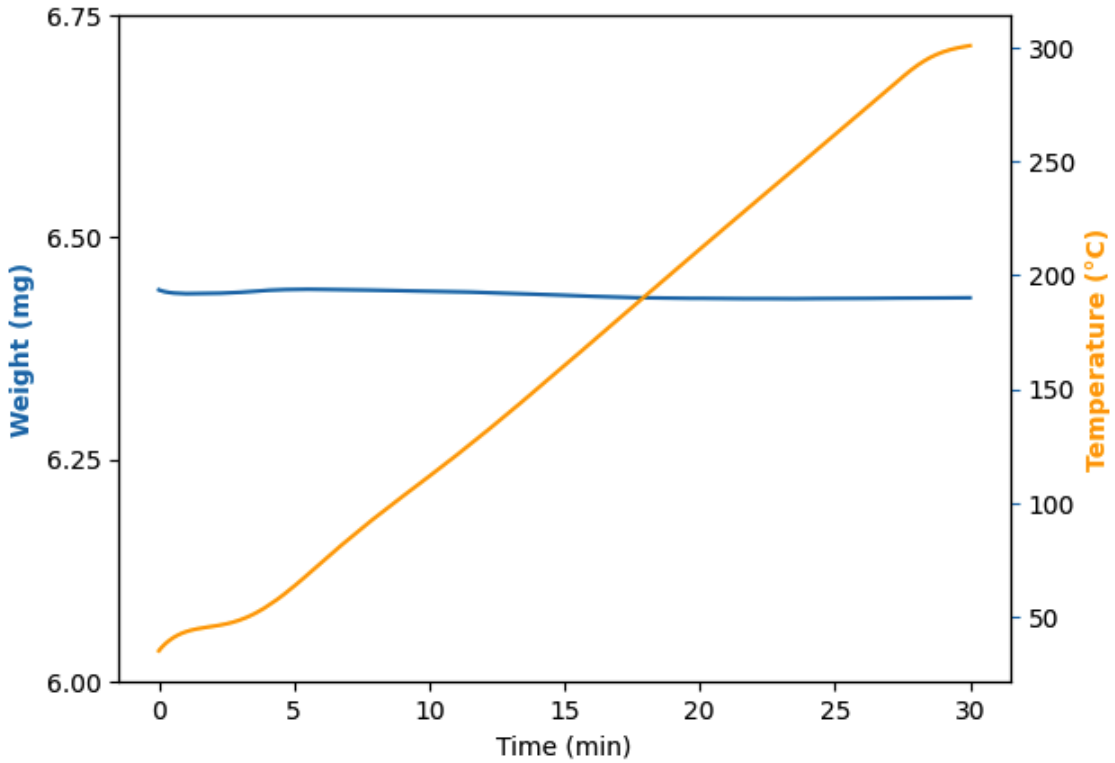

Figure 4-9: TGA on SEI formed in 1M $LiPF_6$ PC without copper current collector.

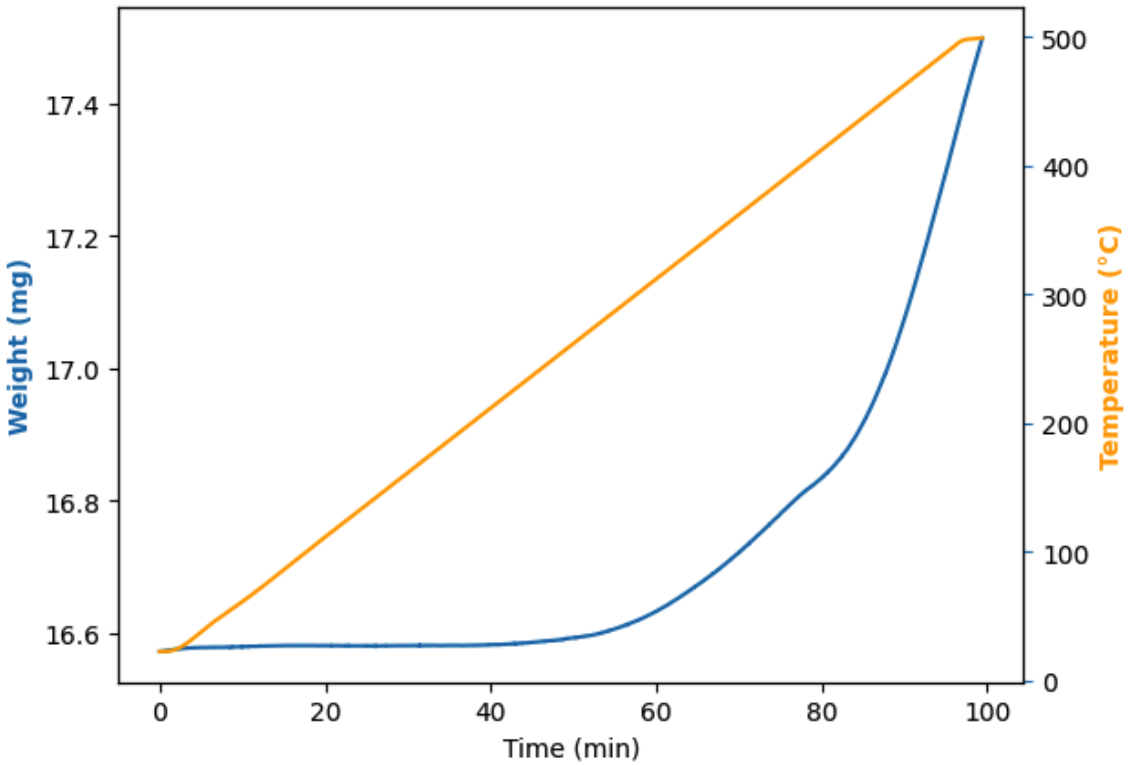

Figure 4-10: TGA on SEI formed in 1M LiTFSI in DOL:DME.

The SEI forms in-situ during the initial charging cycles of an LIB, and its growth is usually self-limiting. The SEI is composed of organic and inorganic compounds, many of which are reactive and sensitive to moisture and oxygen, making the SEI very difficult to handle outside of a glovebox. Performing thermal analysis on the SEI becomes very difficult since DSC and TGA experiments do involve some contact with the ambient air environment during the sample loading process. Even then, the SEI layer is very thin and fragile, and handling it without causing damage is also a challenge. Furthermore, the heterogeneous and evolving nature of the SEI layer means that it can be hard to get a representative sample for these measurements. In many cases when the SEI samples were being prepared, we were not able to generate an appreciable amount of SEI (depending on the choice of electrolyte used).

In conclusion, we have encountered significant challenges in conducting thermal analysis on the SEI. The reactive and environmentally sensitive nature of the SEI necessitates handling and storage within a controlled glovebox environment. The inherent characteristics of the SEI and the experimental conditions required to study it pose considerable obstacles to performing reliable and repeatable thermal analysis. These multifaceted difficulties rendered our analysis inconclusive, leading us to shift our focus away from the SEI layer in this particular study.

4.4 Salts

Salts play a crucial role in the electrolytes of LIBs. The primary purpose of the salt in the electrolyte is to provide Li^+ for conduction and to shuttle from the anode to the cathode during discharge and in the reverse direction during charging. The anions of the salt also contribute to the electrolyte's overall stability by causing a more stable electrolyte environment that can withstand higher operating voltages without decomposing[52]. As previously mentioned, the salt is also involved in the formation of the SEI. It becomes important to understand the thermal behavior of salts and how they decompose within different electrolyte systems. Therefore, studying these interactions, particularly under different thermal conditions, can yield valuable insights into optimizing the electrolyte formulation for improved battery design and safety performance.

In this section, we review the existing literature on the thermal behavior of $LiPF_6$ salts. Following that, we conducted an investigation into the thermal behavior of $LiPF_6$-based electrolytes. We illustrate the interplay between the colligative property of boiling point elevation and the chemical reactivity of an electrolyte at varying concentrations of $LiPF_6$ in DMC. Our findings showcase how these fundamental properties influence each other, highlighting the complexities of thermal behaviors in such electrolyte systems.

4.4.1 Brief Literature Discussion on $LiPF_6$

The salts used in lithium-based batteries are lithium salts, LiX; therefore, the only degree of freedom is in the X^- anion. The major purpose of salts in cells is to preserve the electrochemical neutrality of the cell. In LIBs, the most decisive choice for a salt used in industrial and commercial production is whether the electrolyte formed from the salt can protect the aluminum current collector from corrosion[27]. The aluminum current collector is subjected to a constant anodic polarization which can lead to

its degradation and disintegration; however, the presence of suitable species in the electrolyte can react with the aluminum and passivate the surface by forming species such as Al_2O_3[39, 48]. Other major requirements for the salt are chemical inertness, insusceptibility to hydrolysis, and thermal stability. The lithium salts also dictate the composition and morphology of the SEI, even though the solvent constitutes the major species in the SEI.

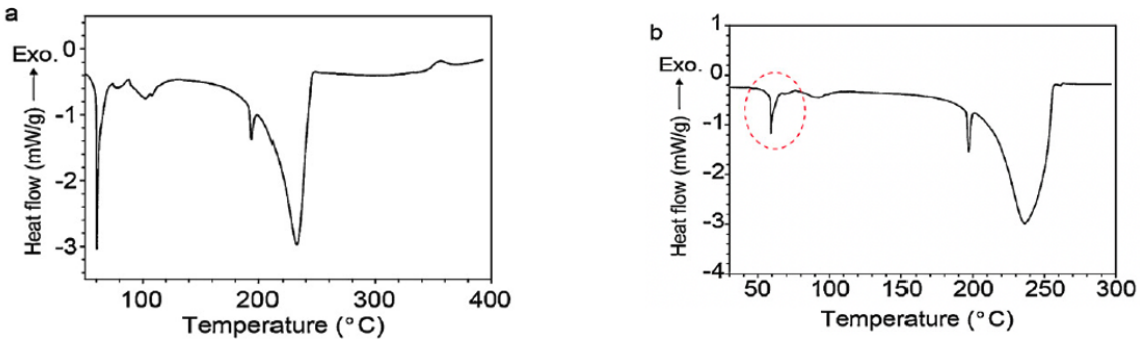

Figure 4-11: DSC heating curves of (a) manufacturer's grade $LiPF_6$ and (b) reagent grade $LiPF_6$. The first endothermic peak occurring below 100°C is attributed to HF removal and thermal decomposition due to presence of even trace amounts of moisture. The large endothermic peaks occurring above 200°C are due to $LiPF_6$ thermal decomposition reaction. Reproduced from [56].

The main salt used in commercial LIBs is lithium hexafluorophosphate ($LiPF_6$) due to its coordination and good solubility in dipolar aprotic solvents (organic carbonates). $LiPF_6$ is a highly soluble salt even in low permittivity solvents such as dimethyl carbonate (DMC). However, $LiPF_6$ is thermodynamically unstable and starts to decomposes to LiF and PF_5 at 50°C[27, 56] (Figure 4-11), and in the presence of even trace amounts of H_2O, can further hydrolyze to produce HF (see Equation 4.1 and Figures 4-12 and 4-14), which is chemically reactive with both electrodes[27, 56, 66]. Figure 4-14 shows the Fourier Transform Infrared (FTIR) spectra of gaseous products from $LiPF_6$ decomposition in the presence and absence of trace water, and confirms that HF is produced when trace water is present.

$$LiPF_6\,(s) + H_2O\,(g) \longrightarrow LiF\,(s) + OPF_3\,(g) + 2\,HF\,(g) \tag{4.1}$$

The TGA profile at 10°C/min heating of $LiPF_6$ in the presence and absence of H_2O demonstrate a noticeable difference in thermal stability, as shown from the derivative curves in Figure 4-12 [66]. The TGA profile of pure $LiPF_6$ in dry environment ($<$ 10 ppm H_2O), as shown in Figure 4-13, indicates no mass loss within 1 h at 70°C or 90°C[66]. This is in contradiction to studies that demonstrate that the temperature of decomposition of $LiPF_6$ is at 50°C[27, 56]. This difference may be due to the purity of the salts used or in the experimental protocol (being cognizant to presence of H_2O, O_2, etc).

The SEI formed in the presence of $LiPF_6$ is highly dense and uniform, making the cell electrochemically efficient (minimal capacity loss) at low temperatures until about 50°C[48, 57, 66]. Numerous potential culprits (complexes) that start decomposing at temperatures close to 50°C include $LiPF_6$, the SEI itself, and some studies have even cited the electrolyte itself decomposing[48, 57, 66].

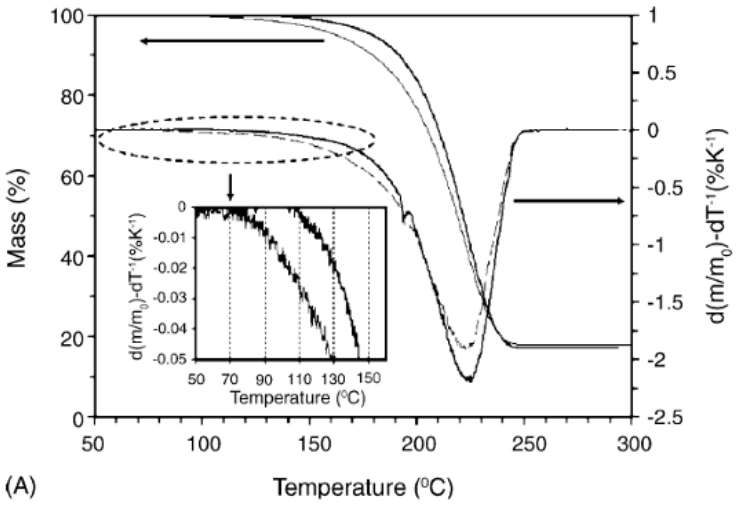

Figure 4-12: Mass loss (left) and rate of mass loss (right) during thermal decomposition of $LiPF_6$ in argon containing $<$ 10 ppm H_2O (solid line) and with 300 ppm H_2O (dashed line). Reproduced from [66].

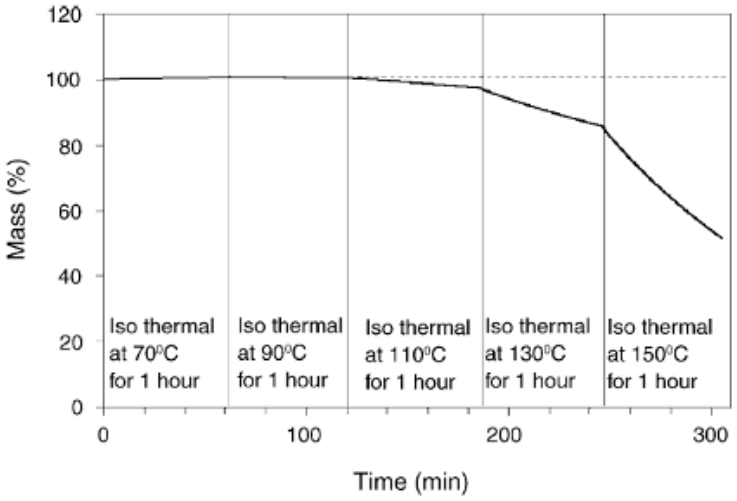

Figure 4-13: TGA isothermal curves of $LiPF_6$ decomposition in dry ($<$ 10 ppm H_2O) carrier gas. Reproduced from [66].

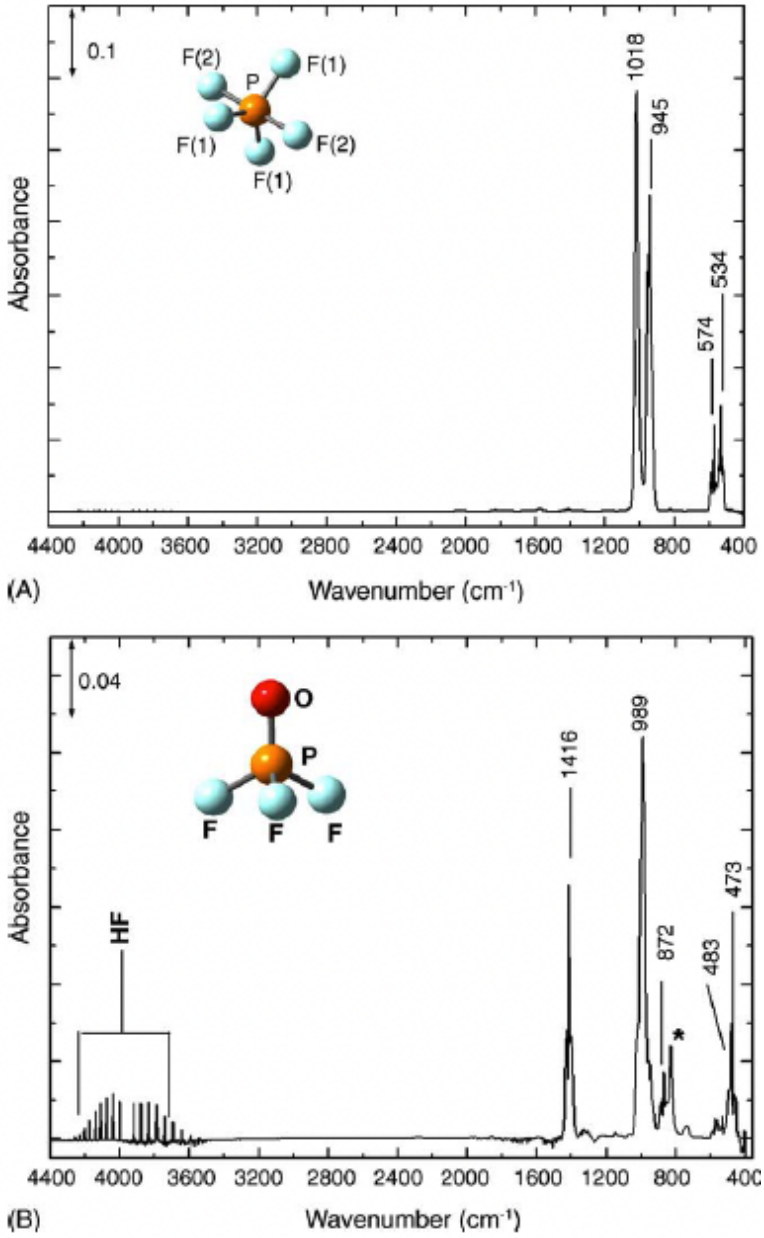

Figure 4-14: FTIR spectra of gaseous products from $LiPF_6$ decomposition at temperature of 215°C in (a) low moisture environment and (b) environment containing 300 ppm of water vapor (B). Spectrum in (a) is assigned entirely to PF_5 and (B) to a mixture of POF_3 and HF. Reproduced from [66].

4.4.2 DSC Analysis on $LiPF_6$-based Electrolytes

While there is heat flow data in the literature on $LiPF_6$ alone and on electrolytes (via DSC), there has been a lack of detailed deconvoluted analysis, which can separate overlapping thermal events into their individual components and provide more detailed insight into these processes. The thermal study of $LiPF_6$ in the solid state (as a salt) is informative, but it does not reveal the effect of its interactions with other species in the electrolyte; nor does a thermal study on the entire electrolyte capture specific interactions within its constituents. Therefore, to capture the different interactions within the electrolyte, we decided to conduct a study of the heat flow profile of the solvent, solvent and salt, and the full electrolyte (solid state solvent added to solvent and salt). In these set of experiments, DMC is chosen to be the solvent as it is commonly used in $LiPF_6$.

Boiling point elevation refers to the increase in the boiling point of a liquid solvent when another compound, typically a non-volatile solute such as a solid particle, is added to it (hence forming a solution). A liquid boils when its vapor pressure is equal to the external pressure. However, the addition of a non-volatile compound (which does not readily evaporate into a gas under existing conditions) reduces the vapor pressure of the solvent. Thus, a higher temperature is required to achieve sufficient vapor pressure for the liquid to boil. This phenomenon holds true even when the solid particles ionize, underscoring that the occurrence of boiling point elevation is independent of the chemical nature of the solute but is influenced by the number of particles added to the solution. Boiling point elevation is a colligative property of a solution, which means it depends on the concentration of solute particles in the solution, not on the type of particles.

The DMC solvent sample and 1.0 mole/L (molar; M), 2.0M, and 3.0M $LiPF_6$ DMC samples were prepared in an argon glovebox environment and then sealed in DSC crucibles. 1.0M $LiPF_6$ DMC is a common electrolyte choice and 2.0M and 3.0M $LiPF_6$ DMC were chosen to double and triple the concentration, respectively. This

was done to investigate the impact of increased salt concentration on the thermal behavior and stability of the electrolyte. The DSC crucible was transferred in a sealed vial from the glovebox to the DSC station. The DSC crucibles were pierced right before the crucible was placed in the DSC chamber, in order to prevent over-pressurization. The DSC runs were conducted at a heating rate of 5°C/min from room temperature to 370°C; the results are presented in Figure 4-15.

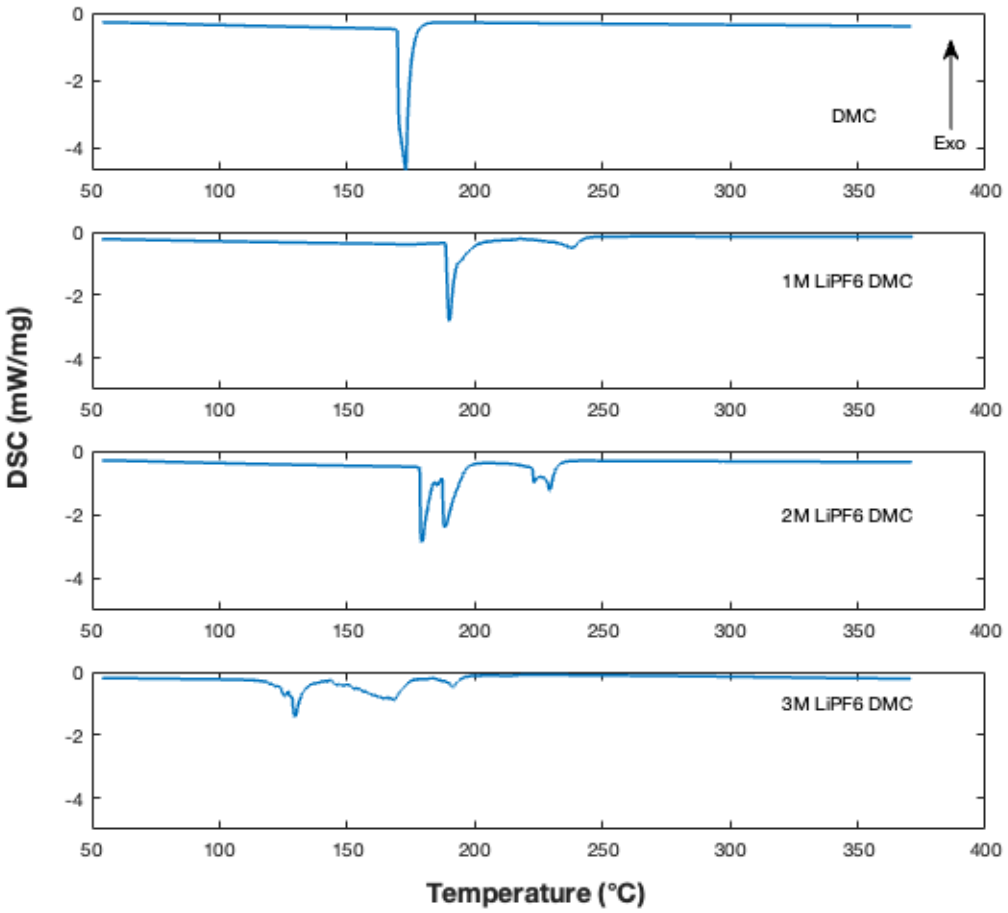

Figure 4-15: DSC runs on DMC; 1.0M, 2.0M, and 3.0M $LiPF_6$ in DMC. The first peak shifts to the right (to a higher temperature) when $LiPF_6$ is first added to DMC at 1.0 mole/L. When the concentration of $LiPF_6$ is further increased, the first boiling peak shifts to lower temperatures than that of 1.0M $LiPF_6$ DMC.

As the concentration of the salt increases, endothermic interactions start occurring at lower temperatures (Figure 4-15). The 1.0M $LiPF_6$ DMC peak is to the right of

the DMC peak. This does not imply a stabilizing effect, but a demonstration of the boiling point elevation colligative property: solute constituent particles disrupt the vaporization process, requiring more energy (higher temperature) to convert the solution into a vapor. The extent of boiling point elevation is proportional to the concentration of the solute particles in the solution. The intermolecular forces are not the only interactions present, as there remain chemical reactions between the $LiPF_6$ and DMC. These chemical reactions are amplified with an increasing $LiPF_6$ concentration and the colligative properties are less dominant. At 3.0M $LiPF_6$ DMC, the peaks occur at lower temperatures than that of pure DMC. The presence of multiple peaks in the 3.0M $LiPF_6$ DMC case corresponds to multiple phase transitions and chemical reactions occurring at different temperatures. These transitions relate to the boiling point of the solution and to changes in the solvent-solute interactions as the system undergoes heating. Table 4.1 tabulates the temperature at the first peak for each DSC curve of DMC and 1.0M,2.0M, and 3.0M $LiPF_6$ in DMC.

	Temperature(°C)
DMC	173.0
1.0M $LiPF_6$ DMC	189.4
2.0M $LiPF_6$ DMC	179.3
3.0M $LiPF_6$ DMC	129.8

Table 4.1: Temperature at the first peak of DSC runs on DMC; 1.0M, 2.0M, and 3.0M LiPF6 in DMC.

When $LiPF_6$ is first added to DMC at a concentration of 1.0M, it is observed that the first peak in the DSC scan shifts to the right, towards a higher temperature. This is consistent with boiling point elevation, a colligative property where the boiling point of a solution is higher than that of the pure solvent due to the presence of solute particles. However, as the the concentration of $LiPF_6$ in the DMC solution increases, the first boiling peak shifts to lower temperatures than that of the 1.0M $LiPF_6$ DMC solution that can be explained by changes in the interactions between the $LiPF_6$ and DMC as the concentration increases, and possibly by side reactions that become significant at higher concentrations. In this analysis conducted, the interplay

between the boiling point elevation colligative property and the chemical reactivity was demonstrated for an electrolyte at different concentrations. This phenomenon has to be further explained in greater detail.

4.5 Standardization of the Protocol and its Application to LiFSI-based Electrolytes

Leveraging the knowledge learned during the thermal analysis on $LiPF_6$ and DMC, mainly the limitations of TGA and DSC experiments on LIB material, and the interplay between the boiling point elevation colligative property and the chemical reactivity, a more comprehensive thermal analysis will be conducted on electrolytes composed of LiFSI salt in DMC and dimethoxyethane (DME) which are conventional solvents that are used in LIBs.

LiFSI has similar conductivity at room temperature to $LiPF_6$ solutions in the same solvent. LiFSI even surpasses $LiPF_6$ conductivity at low and sub-zero (negative) temperature ranges, thereby enhancing the battery operability at lower temperatures. While $LiPF_6$ can decompose and react with water to form HF, a highly reactive and corrosive substance, LiFSI does not form HF, making it a significantly safer choice. LiFSI is compatible with various types of solvents and can be used in different electrolyte formulations. Moreover, LiFSI is known to allow for the stable electrochemical cycling of $LiFePO_4$ (LFP)-based cells, which is important given that LFP cathodes do not use the scare and expensive cobalt[23].

Previous thermal studies on LiFSI have mainly relied on comparing it to $LiPF_6$ have relied on demonstrating the lower gas evolution of LiFSI from "pouch cell studies". These pouch cell studies rely on storing pouch cells of LiFSI-based LIBs and $LiPF_6$-based LIBs at 60°C for some time and then comparing the gases evolved through ex-situ gas measurements[49].

In our study, we propose a standardized experimental protocol that integrates TGA and DSC experiments to go beyond their classical stand-alone application in polymer thermal analysis. This integrated approach aims to address the complexity of LIB thermal analysis, which encompasses not only phase changes but also intricate chemical reactions. In our thermal analysis experiments, LiFSI was used with a DMC

(carbonate) and DME (ether) solvents. Our interest in this system is given their high columbic efficiencies (and therefore, their promising potential) in LIB and lithium metal batteries, especially when LiFSI is used at high concentrations (Figure 4-16).

Our thermal analysis revealed distinctive interactions when LiFSI was incorporated into different electrolyte systems. Specifically, we observed variations in thermal behavior between the carbonate-based and ether-based electrolyte systems. In the carbonate-based electrolyte system, an exothermic peak was detected at 350°C. This suggests a heat-releasing reaction or phase change occurring at this temperature, a characteristic unique to this particular system when interacting with LiFSI. The ether-based electrolyte system demonstrated an exothermic peak at a considerably lower temperature range of 200°C, implying that a heat-releasing process happens at a lower temperature compared to the carbonate system. Additionally, an endothermic peak was observed at the 300°C temperature range in the ether-based system, indicating a heat-absorbing process or phase change occurring at this temperature. These different thermal responses highlight the influence of the electrolyte system on the thermal stability of the LIB.

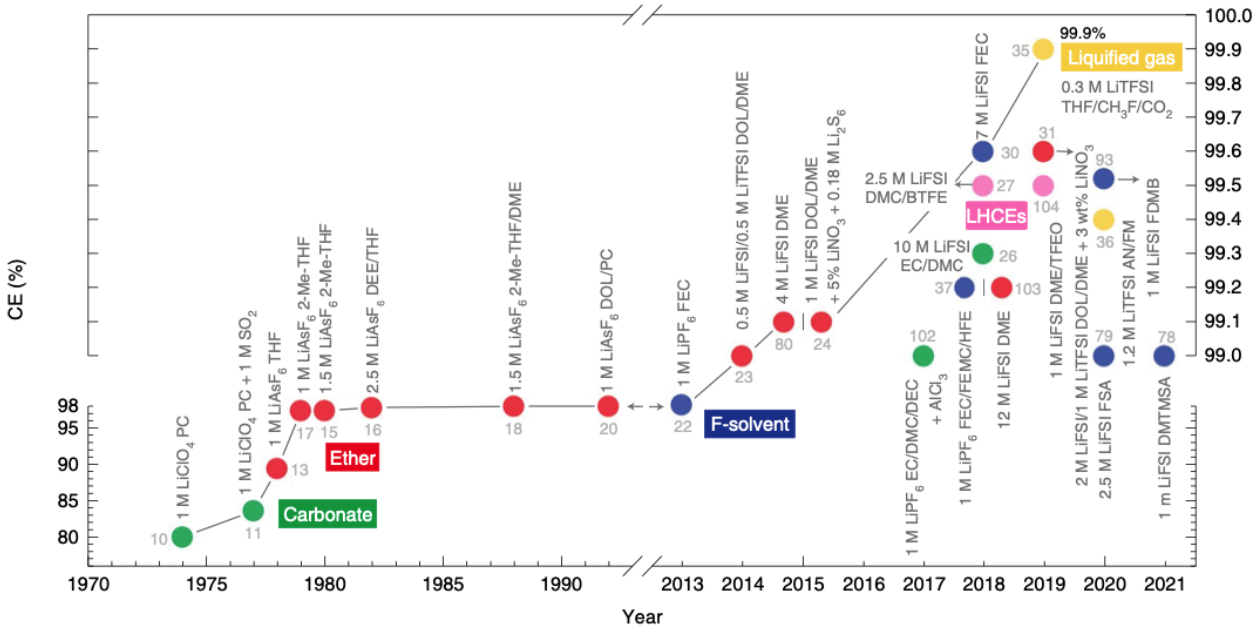

Figure 4-16: Benchmarking of published electrolyte strategies with record-breaking columbic efficiencies (CE) for lithium metal batteries - sorted by publication year. If a battery has a CE of 98%, it means that 2% of the energy is lost during each charge-discharge cycle. Over thousands of cycles, these losses accumulate and can significantly reduce the battery's useful life. The past decade has shown electrolyte formulations that have shown CE increases by 1-2% compared to previous electrolyte formulations that were only able to exhibit a CE of up to 98%. This is significant because even a 1-2% increase in CE can profoundly impact the performance and longevity of a battery system, especially in large-scale energy storage. Reproduced from [38].

4.5.1 Methodology

The first step in our protocol to acquire consistent and interpretable thermal signals is to standardize the sample container. We opted to hermetically seal inside the glovebox every sample for both TGA and DSC in a DSC crucible. The mass of the hermetically sealed crucible was weighed before and after the sample was loaded to know the mass of the empty crucible and the sample. Following this, in both the TGA and DSC scenarios, the hermetically sealed DSC crucibles which had the samples were placed in an gas-tight vial inside the glovebox. This vial was then carefully transported to the respective TGA and DSC stations. To limit air exposure time, the vial was opened only once at the station and the sealed crucible was punctured with a pinhole and swiftly loaded into the relevant apparatus. This method ensures the sample's exposure to ambient conditions is minimized, thus aiming to limit deviations and reactions with air.

*Many papers in the literature fail to mention the DSC protocol used and whether sealed or unsealed crucibles were used. This omission poses a significant limitation to the overall understanding of the experimental data. It is worth noting that certain papers have utilized unsealed crucibles for their DSC studies, yet they have failed to account for mass loss as a function of temperature[26]. The use of unsealed crucibles makes the analysis difficult to interpret as their is not a clear understanding of whether the changes observed are due to thermal decomposition, volatilization, or other phenomena associated with mass loss - or if there is even mass loss in the first place. Consequently, the findings obtained from these studies lack clarity and may lead to erroneous conclusions (see Figure 4-17). 18650 cells are cylindrical LIBs, named for their dimensions of 18mm diameter and 65mm length, making them slightly larger than standard AA batteries. In one study, three commercial 18650 Li-ion cells with $LiCoO_2$ (LCO), $LiFePO_4$ (LFP), and $LiNi_xCo_yAl_{1-x-y}O_2$ (NCA) cathodes were studied using the DSC on the component level[26]. Conducting separate thermal analyses of different anodes and cathodes at varying states of charge (SOC) is critical to un-

derstanding their individual behaviors and the thermal stability of LIBs. However, the experimental protocol adopted in the study fell short, resulting in data of low resolution. This underscores the necessity of more rigorous and improved protocols to ensure high-quality and more interpretable data in LIB thermal analysis.

The usage of unsealed DSC crucibles in the study introduced difficulty in conducting a useful analysis. It made the identification of peaks challenging. Note that in this paper, unlike the convention used in reporting DSC results, the downward direction (negative values) indicate exothermicity. As shown in Figure 4-17, the definition of the exotherms was lost and became difficult to definitively distinguish from the baseline. This resulted in a lack of precise understanding of the materials' thermal properties. For example, on a macro-level, subfigures E and F reveal distinct thermal responses: LFP cathodes, as displayed in subfigure E, show an endothermic behavior, whereas NCA cathodes in subfigure F present an exothermic reaction, both in the vicinity of 200°C. However, it proves challenging to derive more detailed information from these results due to the broad curves.

When the battery is fully charged (100% SOC), the anode holds a large concentration of Li^+. As the LIB discharges and the SOC decreases, the Li^+ move from the anode to the cathode. This alters the chemical composition of both the anode and cathode materials. These changes can affect their thermal responses in several ways. From Figure 4-17, it is hard to determine the correlation of SOC and the onset temperature (peaks) within the same cathode. One would expect that changes in the SOC would proportionally impact the amount of heat that is generated (released) or gained; however, the data from all three anode and cathode cases contradict this expectation. There is no discernible trend to suggest which SOC - 0%, 50%, 75%, or 100% - corresponds to the highest or lowest heat change. This could potentially be due to a variety of factors, including the intricate and multi-faceted nature of the electrochemical reactions taking place within the battery or changes in the thermal properties of the battery materials as the SOC shifts. This emphasizes the complexity of the relationship between SOC and heat generation in batteries and underscores the

need for further investigation into this matter.

DSC plots A-C in Figure 4-17 represent graphite anodes disassembled from the three different 18650 LIBs. The paper does not explicitly state whether the electrolyte used in each of the three batteries is the same. However, assuming that the electrolyte is indeed identical across the LIBs, the variable across the LIBs and that can *possibly* influence the anode chemistry would be the cathode. As mentioned, the SEI formation process involves the reduction and decomposition of electrolyte components upon contact with the Li. Thus, in general, the SEI is primarily a product of interactions between the electrolyte and the anode, rather than the cathode. While the cathode does not directly contribute to the SEI, it *can indirectly* impact the SEI formation and properties through altering the overall electrochemical stability of the electrolyte, which may influence the formation and composition of the SEI. A macro-level detail that is deduced from the DSC plots is that the NCA anode showed DSC onset temperatures slightly lower than those of the LCO anode.

The data presented in the paper is valuable, but by implementing our refined methodology we can extract even more detailed curves that distinguish between exothermic and endothermic reactions. Utilizing sealed crucibles with pinholes, a notable improvement over unsealed ones, allows for more accurate identification of peaks and their corresponding temperatures. This method, therefore, enables a more in-depth interpretation of thermal behaviors. Additionally, we incorporate the use of a TGA, which provides insights into mass loss as a function of temperature. This technique, which was not utilized in the referenced paper, provides a more comprehensive picture of the thermal behavior of LIB components.

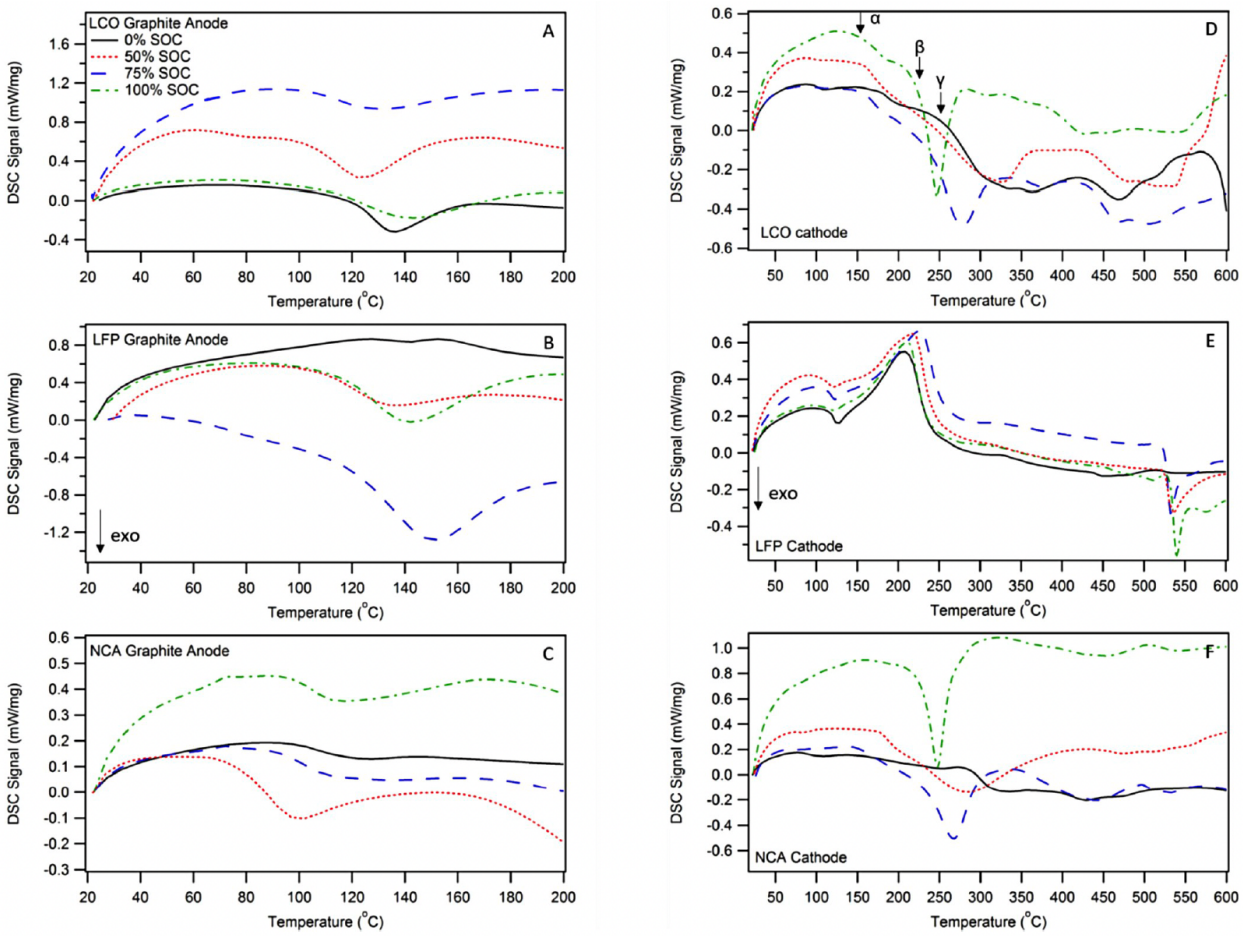

Figure 4-17: DSC results of anodes and cathodes at different SOC using unsealed crucible. The authors mark α, β, and γ in the DSC plot of the LCO cathode in Fig. 3D to reveal an initial small exothermic peak onset at 150°C (α), immediately followed by a larger exothermic peak (β) whose maxima and definition increases with increasing SOC. At lower SOC (0% and 50%), the peak onset (γ) and maxima are shifted to higher temperatures. The authors' presentation of data up to 200°C for anodes while extending to 600°C for cathodes may indeed suggest a difference in the thermal stability of these materials. While cathode materials (inorganics) are known to be more thermally stable and decompose at higher temperatures compared to anode materials (organic), it is not entirely clear from the information provided whether the authors stopped the anode DSC scans at 200°C, or simply chose to visually display the curves up to this temperature.Reproduced from [26].

To address such issues and improve the accuracy of the DSC analysis, it is important to incorporate TGA data by normalizing by the instantaneous mass. By doing so, the DSC signals can be appropriately interpreted, as the true contribution of a smaller mass (at higher temperatures) is revealed. Neglecting to incorporate TGA data leads to attenuation of the DSC signals therefore compromising the validity and reliability of the results. Both TGA and DSC methods complement each other, providing information not only on the temperatures at which the significant changes occur, but also on the nature (endothermic or exothermic) and the magnitude of these changes (mass loss and heat flow).

TGA runs must be conducted before DSC runs, in order to obtain mass as a function of temperature. Both the TGA and DSC experiments have to be conducted at the same heating profile. In our case, we chose an experimental heating protocol with an intermediate heating rate of 5°C/min from 25°C to 400°C. As shown in Figure 3-17, with multiple heating and cooling DSC correction runs, temperatures below 50°C and above 370°C do not equilibrate as they were on the extremum of the temperature range (see note on sample temperature control in Section 3.2.2); therefore, values below 50°C and above 370°C were omitted from the analysis. In order to keep both environments identical, inside both the DSC and TGA furnace chambers, the flow rate of the argon gas was set to 90 mL/min.

Following the standard convention of reporting DSC data from the polymers community, in our experiments, positive values indicate exothermicity (heat flow out of the sample) and negative values indicate endothermicity (heat flow towards the sample).

4.5.2 Results

DMC

DMC ($C_3H_6O_3$) has a normal boiling point of 90°C, a density of 1.07 g/mL at 25°C, and a molar mass of 90.08 g/mol. The skeletal structure of DMC is presented in Figure 4-18. Similar to the DME sample, the DMC sample was prepared in an argon-filled glovebox and transported in a sealed DSC crucible until it was slit with a pinhole and immediately loaded into the DSC chamber.

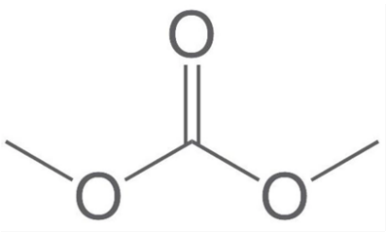

Figure 4-18: Skeletal structure of DMC.

From the TGA profile of DMC (Figure 4-19), the boiling point of the DMC sample in the crucible is 99°C, due to pressurization. The temperature at which 5% mass loss occurs is 50°C.

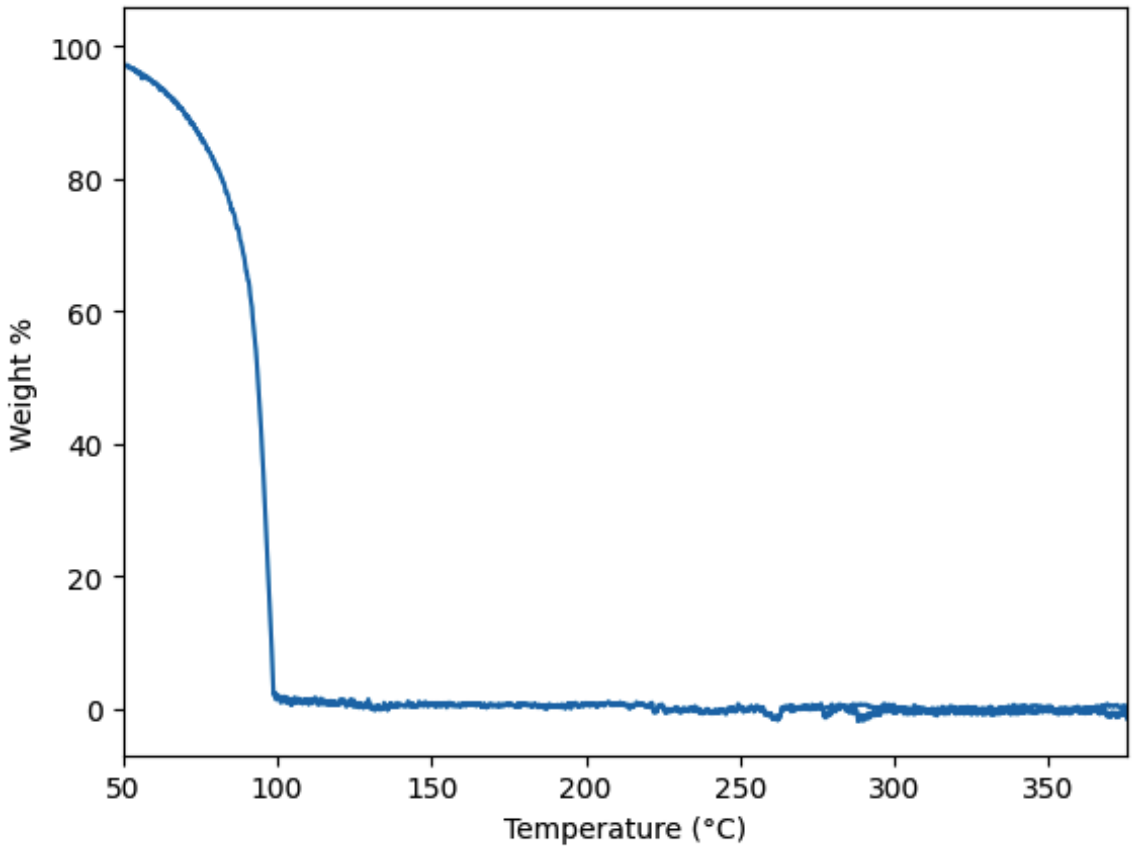

Figure 4-19: The TGA profile of DMC shows a pressurization-induced boiling point at 99°C and a 5% mass loss occurring at 50°C.

DME

DME ($C_4H_{10}O_2$) is a colorless and aprotic liquid ether that has a normal boiling point of 85°C, a density of 0.867 g/mL at 25 °C, and a molar mass of 90.12 g/mol. A TGA analysis was conducted on a DME sample placed in a sealed DSC crucible with a pinhole slit that was conducted immediately before the sample was loaded to the TGA (in order to minimize time in exposure to air) (Figure 4-21).

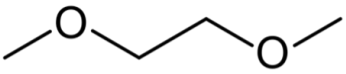

Figure 4-20: Skeletal structure of DME.

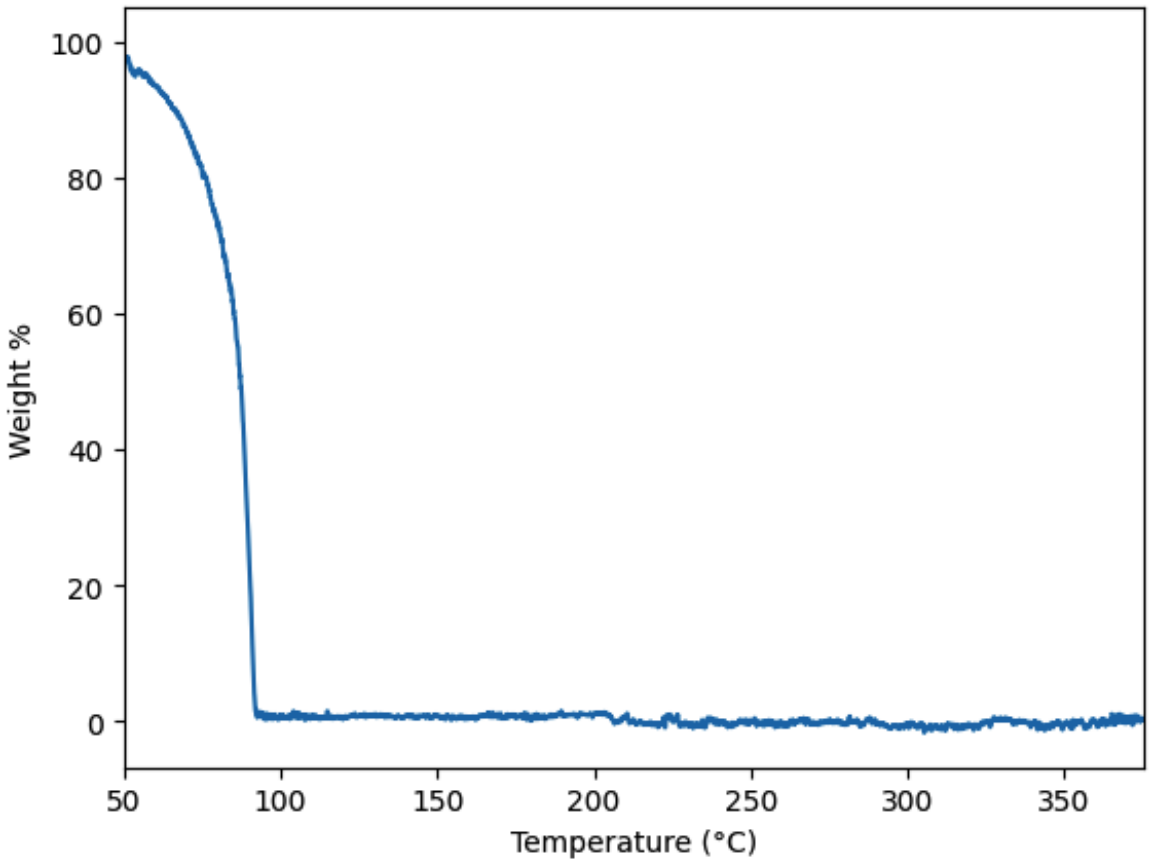

Figure 4-21: The TGA profile of DME revealed a boiling point at 92°C and recorded a 5% mass loss at 53°C.

From the TGA profile of DME (Figure 4-21), the boiling point of the DME sample in the crucible is 92°C, which is slightly above the normal boiling point of DME (85°C) due to pressurization in the DSC crucible. The temperature at which 5% mass loss occurs is 53°C.

LiFSI

The TGA and DSC results of LiFSI are presented in Figure 4-22. LiFSI salt is a solid at room temperature and remains thermally stable until it melts at a temperature of 146°C. This is shown with the downward peak, which as mentioned, represents endothermicity (heat flow into the sample, thus results in melting). At 146°C, there is no mass loss. The LiFSI salt experiences 5% mass loss at a temperature of 312°C. A strong exothermic peak occurs at 360°C. The exothermic peak occurs when the mass percent of the sample is 62.6% (37.4% mass loss). This suggests that a significant decomposition or reaction occurs in the sample, leading to the release of heat and the corresponding mass loss.

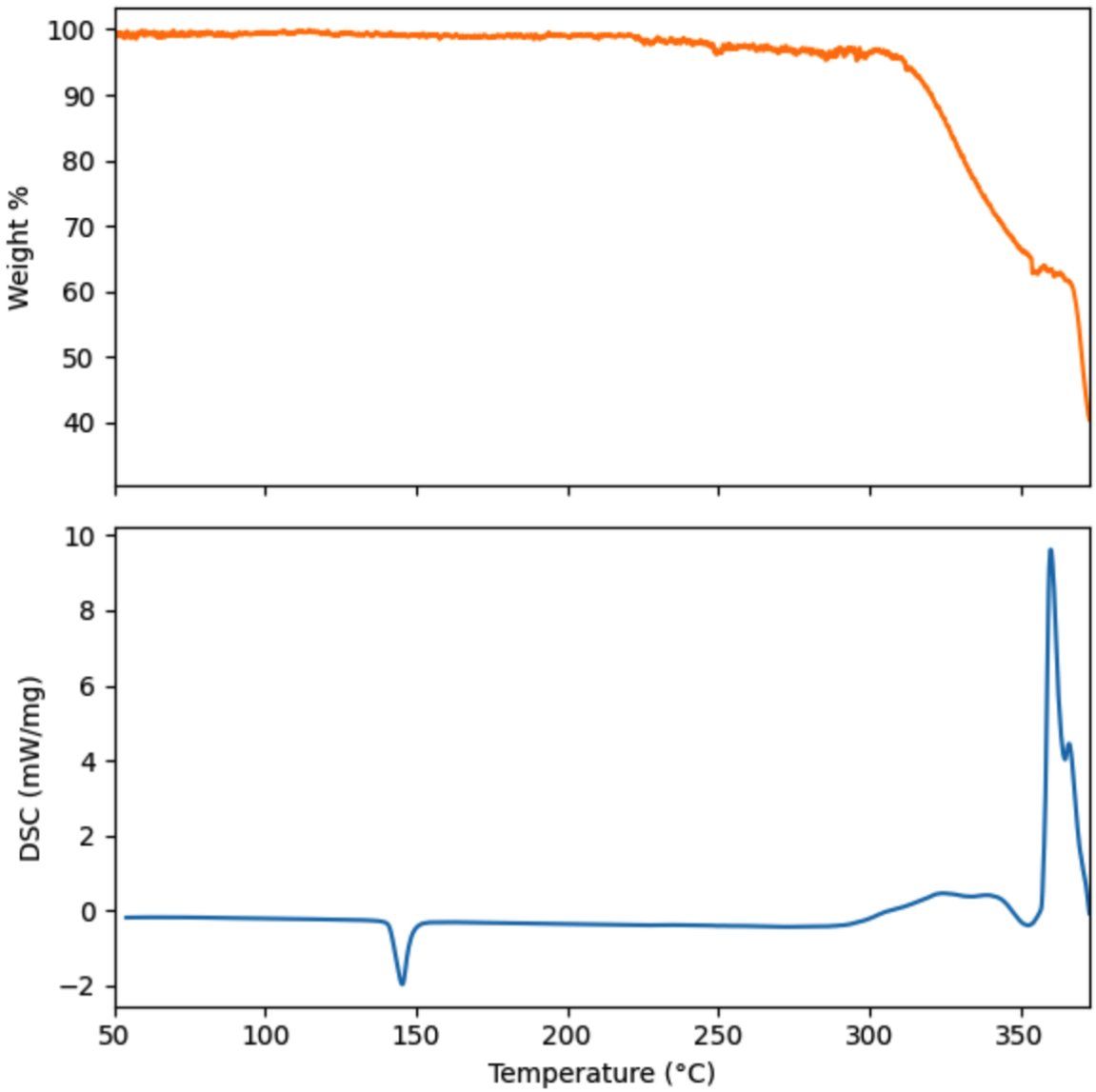

Figure 4-22: TGA (top) and DSC (bottom) of LiFSI salt. The heating rate is at 5°C/min.The endothermic process (indicated by the downward peak) does not coincide with mass loss, thereby indicating melting of the salt. An intense exothermic peak at 360°C, corresponding with a 37.4% mass loss, indicates a substantial decomposition reaction within the sample, leading to heat release and subsequent mass reduction.

3M LiFSI DMC

The 3M LiFSI DMC electrolyte solution was prepared by dissolving LiFSI in DMC solvent according to their stoichiometric ratio. The resulting solution was by mass 34.4% LiFSI and 65.6% DMC. The TGA and DSC results of 3M LiFSI DMC are presented in Figure 4-23. No melting of LiFSI is exhibited since it is ionized in the solution, meaning it exists as ions rather than as a solid at room temperature. The electrolyte solutions experiences 5% mass loss at a temperature of 98°C, unlike in the case of the TGA of pure DMC where 5% mass loss occurs at a temperature of 50°C (Figure 4-19). A strong exothermic peak occurs at 348°C. The exothermic peak occurs when the mass percent of the sample is 13.8% (86.2% mass loss). This suggests that a significant decomposition or reaction occurs in the sample, leading to the release of heat and the corresponding mass loss. Compared to the pure LiFSI salt case (Figure 4-22), the exothermic peak occurs at a lower temperature, with the remaining mass being also attributed to LiFSI.

The findings have relevance even if 350°C is well above the thermal runaway temperature of LIBs, which are typically below 200°C. Firstly, it underscores the inherent thermal stability of the LiFSI DMC electrolyte solution, which can resist decomposition up to high temperatures. This can contribute to safer operation under normal conditions. Secondly, should a thermal runaway occur, understanding the behavior of the electrolyte at these higher temperatures is crucial. Knowing that an exothermic decomposition reaction occurs at 348°C provides insights into potential secondary reactions or further heat releases that might exacerbate a thermal runaway event. Thus, these results help us to design better thermal management strategies and improve the safety features of LIBs.

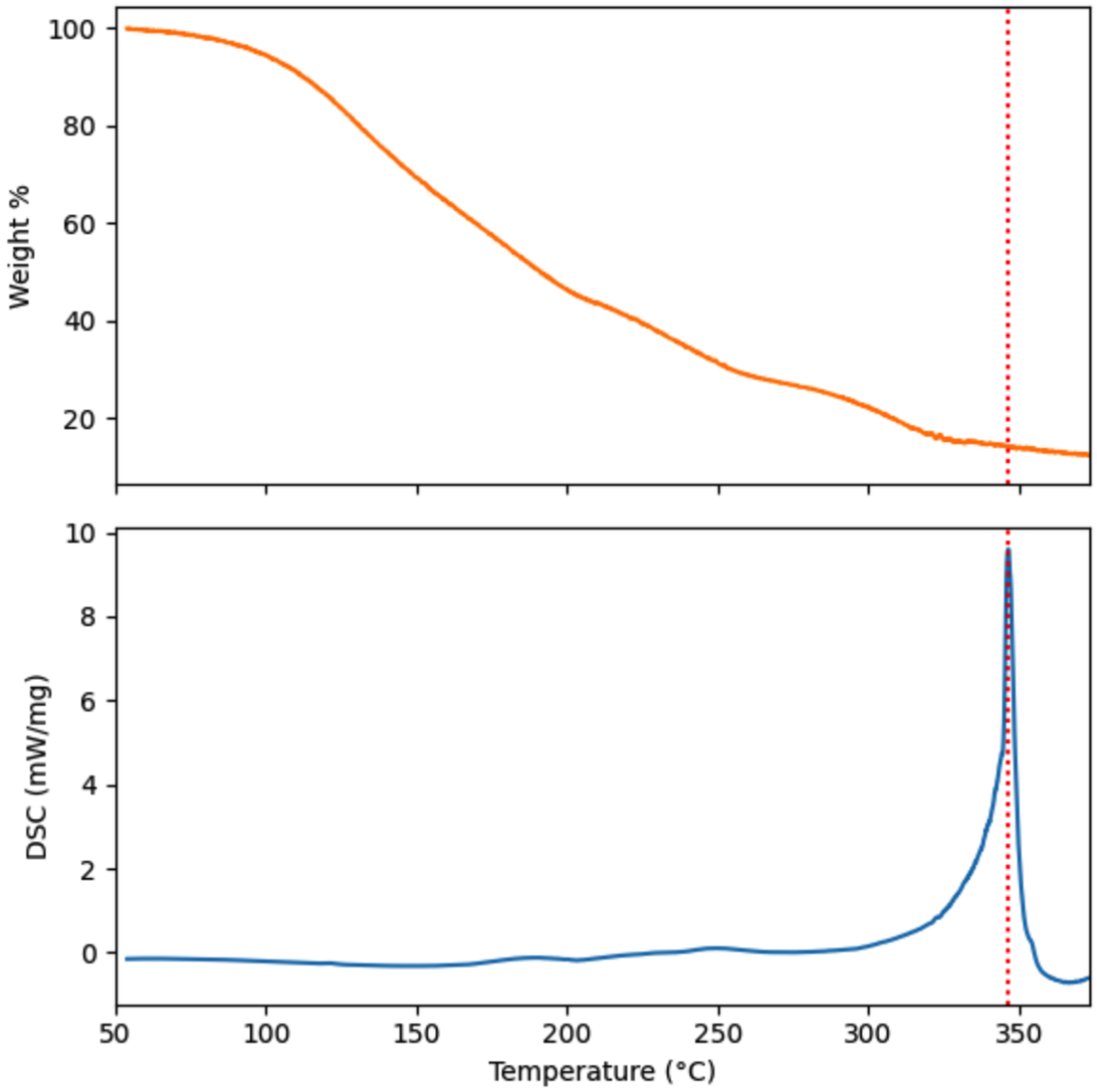

Figure 4-23: TGA (top) and DSC (bottom) of 3M LiFSI DMC electrolyte solution. Dotted line represent the local maxima of the DSC curve. The 5% mass loss at 98°C and the significant exothermic peak at 348°C, corresponding with an 86.2% mass loss, suggest substantial decomposition reactions within the solution, leading to heat release and subsequent mass loss.

5M LiFSI DMC

The 5M LiFSI DMC electrolyte solution was by mass 46.7% LiFSI and 53.2% DMC. The TGA and DSC results of 3M LiFSI DMC are presented in Figure 4-24. Similar to the 3M LiFSI DMC case, the 5M LiFSI DMC electrolyte solutions experiences 5% mass loss at a temperature of 99°C. A strong exothermic peak occurs at 351°C. The exothermic peak occurs when the mass percent of the sample is 24.3% (75.7% mass loss). This does not simply suggest boiling or evaporation, but rather a significant exothermic decomposition or reaction occurring in the sample.

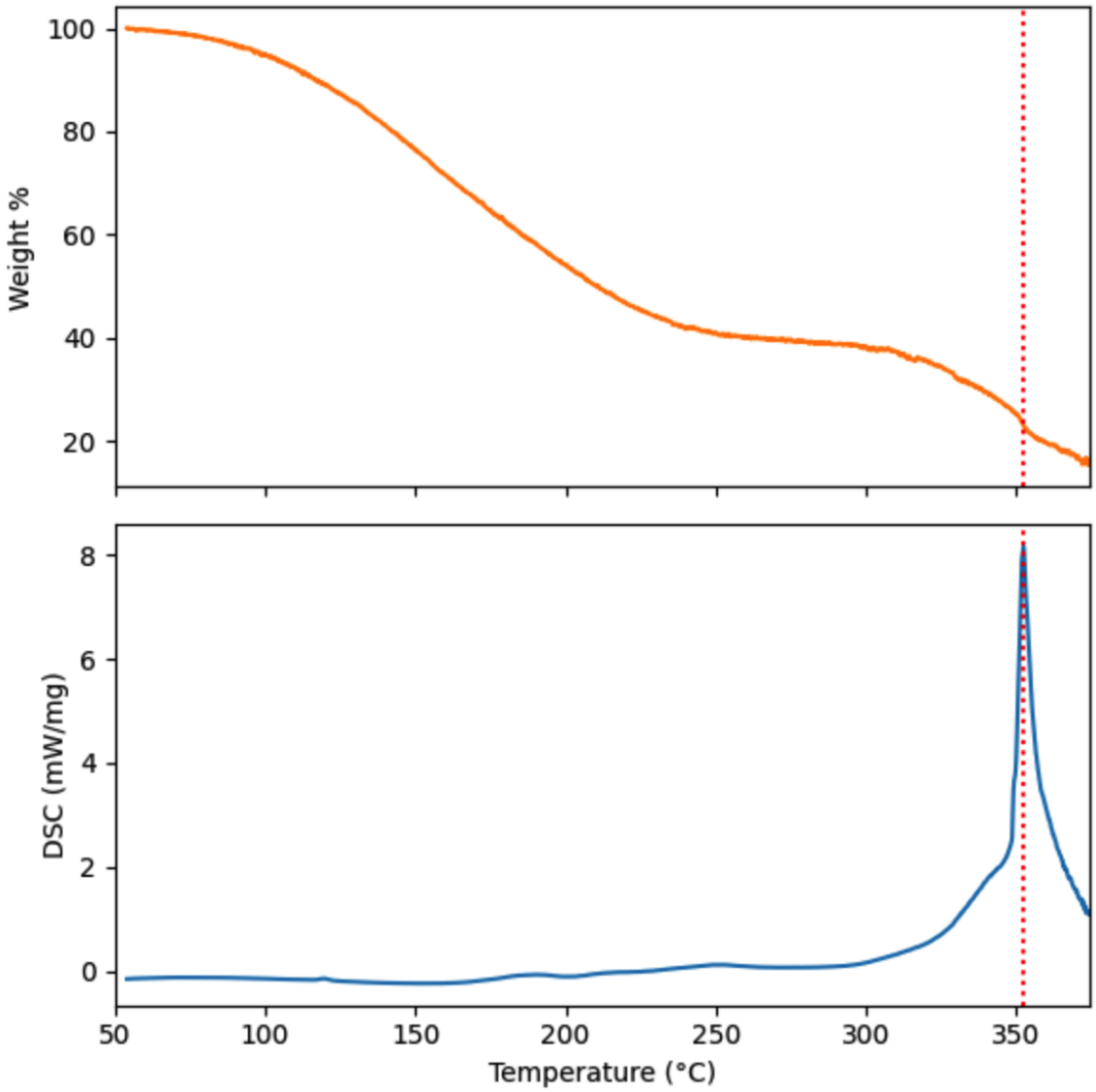

Figure 4-24: TGA (top) and DSC (bottom) of 5M LiFSI DMC.A 5% mass loss is observed at 99°C. A significant exothermic peak at 351°C, corresponding with a 75.7% mass loss, indicates a substantial decomposition or reaction within the solution rather than simple boiling or evaporation.

3M LiFSI DME

The 3M LiFSI DME electrolyte solution was by mass 39.3% LiFSI and 60.6% DME. The TGA and DSC results of 3M LiFSI DME are presented in Figure 4-25. The 3M LiFSI DME electrolyte solutions experiences 5% mass loss at a temperature of 84°C. An exothermic peak - though not as large as in the DMC case - occurs at 208°C. The exothermic peak occurs when the mass percent of the sample is 35.9% (64.1% mass loss). Compared to LiFSI in DMC, LiFSI in DME exhibits exothermicity, suggesting a significant decomposition or reaction occurring in the sample at the 200°C temperature range. This demonstrates that the choice of solvent can influence the thermal behaviour of the electrolyte solution. The endothermic local minima occurs at 307°C when the mass percent of the sample is 17.7% (82.3% mass loss). This endothermicity observed in the 3M LiFSI DME electrolyte solution suggests a heat-absorbing process or reaction, potentially associated with the decomposition or phase transition of the residual salt remaining after all the solvent has evaporated.

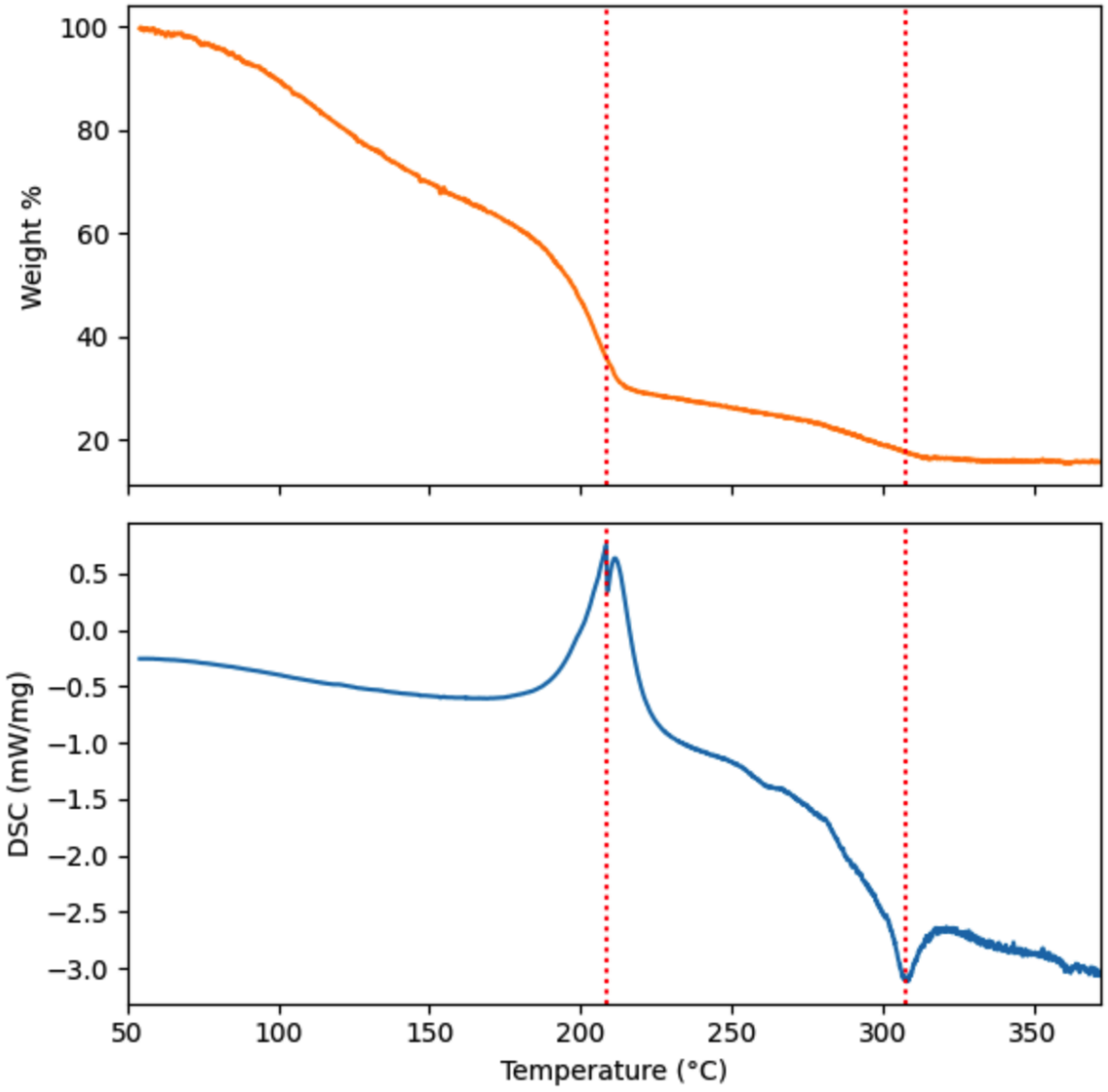

Figure 4-25: TGA (top) and DSC (bottom) of 3M LiFSI DME. Dotted line represent the local maxima and minima of the DSC curve. An exothermic reaction, marked by a peak at 208°C and concurrent with a 64.1% mass loss, signifies significant decomposition or transformation. A distinct endothermic local minimum at 307°C, at an 82.3% mass loss, indicates a heat-consuming process, possibly a phase transition or decomposition of residual salt after all solvent has evaporated.

5M LiFSI DME

The 5M LiFSI DME electrolyte solution was by mass 48.1% LiFSI and 51.9% DME. The TGA and DSC results of 5M LiFSI DME are presented in Figure 4-26. The results follow the same trends as with the 3M LiFSI DME case, with the exothermic local maxima occurring at 210°C and the endothermic local minima at 303°C.

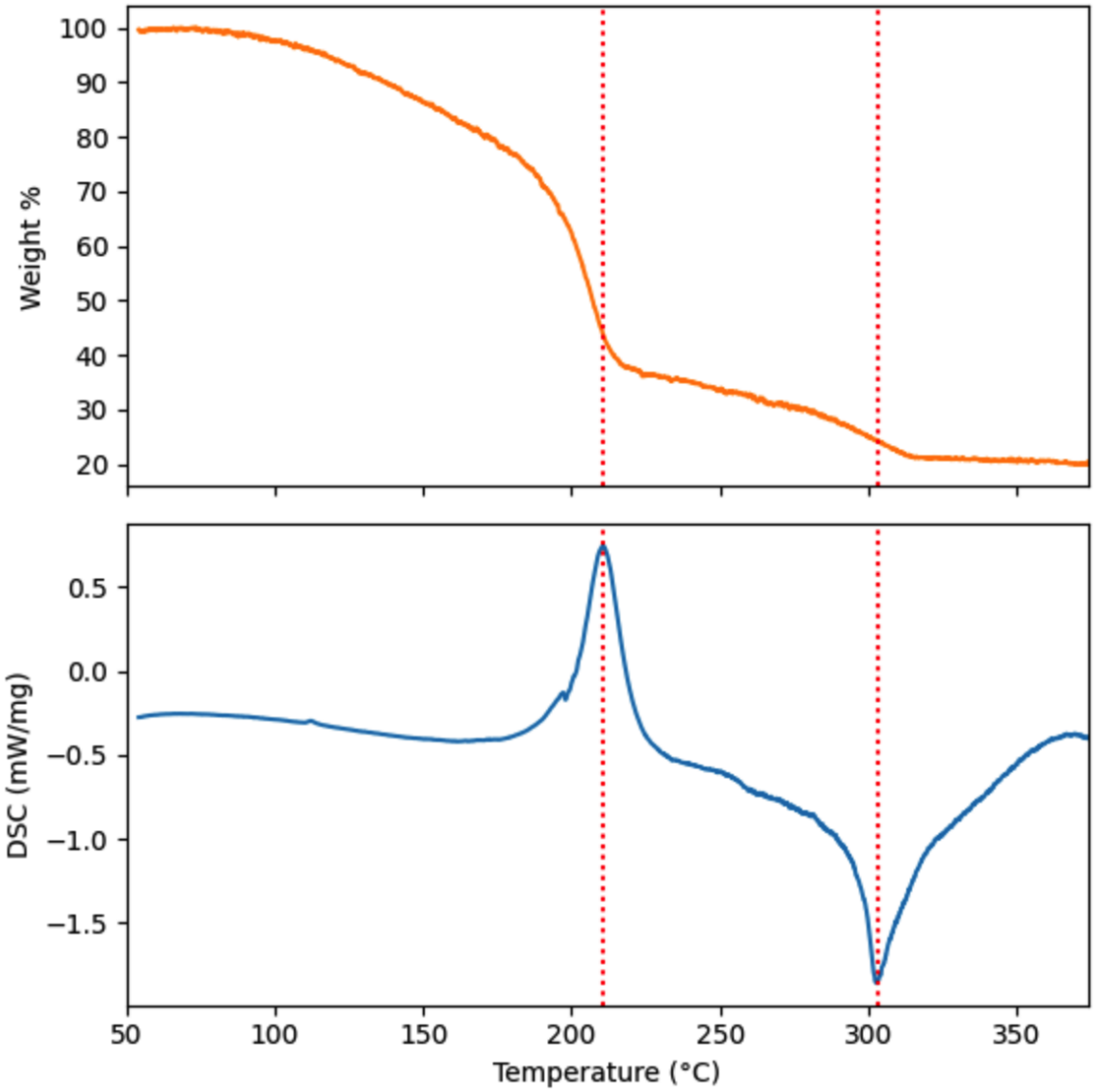

Figure 4-26: TGA (top) and DSC (bottom) of 5M LiFSI DME. The thermal behavior is similar to that of the 3M LiFSI DME solution, with an exothermic peak at 210°C signifying significant decomposition or transformation. An endothermic trough at 303°C indicates a heat-absorbing process, potentially a phase transition or decomposition of the remaining salt after solvent evaporation. This consistency underlines the inherent thermal trends of LiFSI DME solutions across varying concentrations.

Tetraglyme

In order to further validate the results of the behavior of LiFSI in DME, we decided to run additional TGA and DSC experiments using tetraethylene glycol dimethyl ether (tetraglyme) solvent instead of DME as that would provide useful comparative data since it is structurally similar. Tetraglyme ($C_{10}H_{22}O_5$) was chosen because its chemical structure is just an elongated version of that of DME (see Figure 4-20 and Figure 4-27). Tetraglyme is a polar aprotic solvent with a normal boiling point of 275°C, a density of 1.009 g/mL, and a molar mass of 222.2g/mol. The TGA profile of tetraglyme is presented in Figure 4-28.

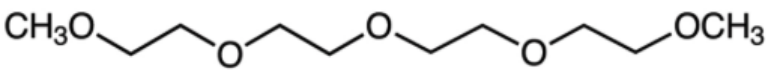

Figure 4-27: Skeletal structure of tetraglyme.

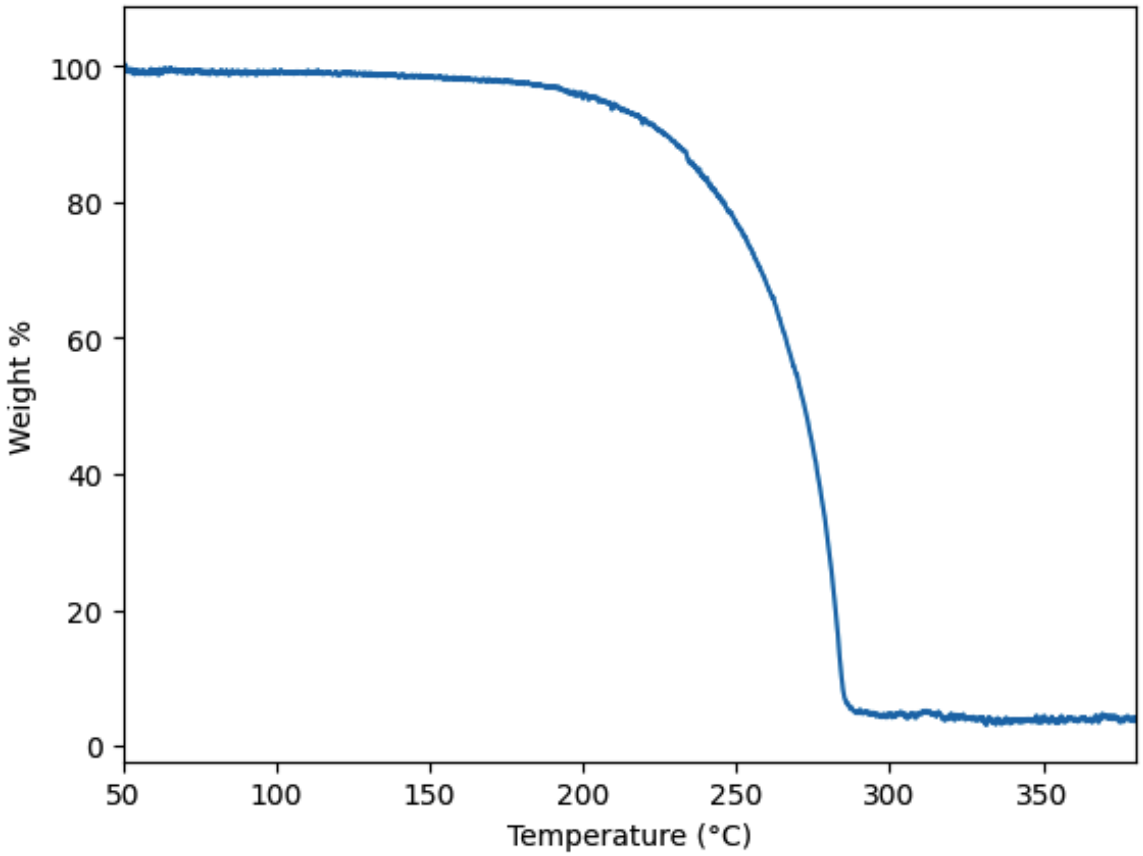

Figure 4-28: The TGA profile of tetraglyme.

The TGA and DSC results of 5M LiFSI tetraglyme are presented in Figure 4-29. The DSC result follow the same trends as with the 3M and 5M LiFSI DME, with the exothermic local maxima occurring in the 200°C range. The 5M LiFSI tetraglyme undergoes an exothermic interaction at 238°C. The 5M LiFSI tetraglyme also undergoes endothermicity but the local minima is not achieving in our temperature range.

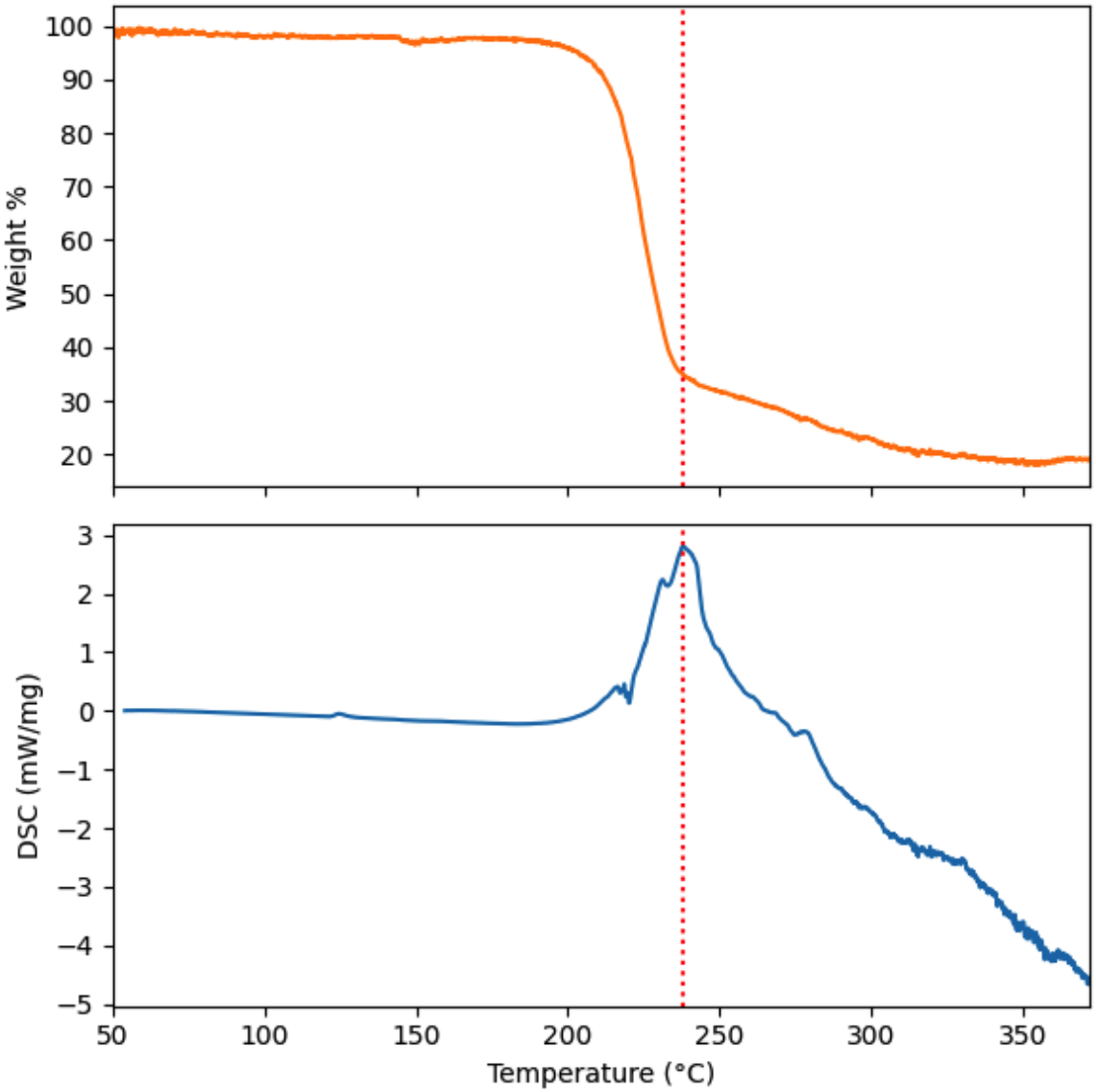

Figure 4-29: TGA (top) and DSC (bottom) of 5M LiFSI tetraglyme. The DSC curve shares similarities with the 3M and 5M LiFSI DME solutions, exhibiting an exothermic peak in the 200°C range (specifically, at 238°C) indicative of substantial decomposition reaction. An endothermic process is also present, but the specific local minimum is not reached within our temperature range.

It is apparent from the results that LiFSI in both DME and tetraglyme undergoes an exothermic event in the 200°C range, with a specific local maximum for 5M LiFSI tetraglyme occurring at 238°C. The similarity in behavior is likely due to the structural similarities of the two solvents, DME and tetraglyme. Both are polar aprotic solvents, which have the ability to dissolve a range of salts, including LiFSI.

Chapter 5

Conclusion and Future Work

5.1 Conclusion

Thermal runaway can have significant implications on the design, material selection, and the battery management systems of lithium-based batteries, impacting their performance, reliability, and life cycle. If heat is not dissipated quickly enough, the temperature of a battery can rise rapidly, leading to a condition known as thermal runaway. Once initiated, thermal runaway can lead to the release of flammable gases, potential battery explosion, or even fire. Consequently, understanding and preventing thermal runaway is critical for ensuring the safe use of lithium-ion batteries, especially in high-energy applications such as electric vehicles and large-scale energy storage systems.

In this study we use the DSC and TGA, which have traditionally been used to study polymers, to study the thermal behavior of LIB components. These techniques provide comprehensive insights into the thermal properties and stability of the materials under varying conditions. By coupling the TGA and DSC, we are able to obtain information not only on the temperatures where significant changes occur but also on the nature (endothermic or exothermic) and the magnitude of these changes (mass

loss and heat flow).

The literature offers significant insights into the thermal behavior of LIB components, but a common practice seen in these studies is the decoupling of the TGA and DSC. While each of these techniques individually provides useful data, when used together, they offer a comprehensive picture of the thermal behavior of LIB components. A limitation observed in the literature is the use of either unsealed DSC crucibles or fully sealed ones, both of which have their shortcomings. Unsealed crucibles decrease the resolution of the data obtained and makes the identification of peaks challenging. On the other hand, fully sealed crucibles prevent mass loss altogether, inhibiting the ability to correlate thermal events with changes in mass.

Our methodology enhances the traditional approach by concurrently performing TGA and DSC using sealed crucibles that are slit with pinholes. This approach offers a more holistic understanding of the thermal behavior, effectively bridging the gap between the mass loss from TGA and the heat flow data from DSC. The design of the crucibles allows for controlled mass loss, providing more precise identification of thermal events and their corresponding impact on mass loss, making for a more profound interpretation of the thermal behavior of LIB components. Incorporating TGA data by normalizing by the instantaneous mass is crucial for accurate interpretation of DSC signals. This procedure reveals the true contribution of smaller mass at higher temperatures, which would otherwise be masked. Failing to incorporate TGA data may result in attenuation of DSC signals, compromising the validity and reliability of the results. We conducted both TGA and DSC experiments under comparable conditions to ensure consistency and reliability in the data collected. This involved maintaining identical TGA and DSC furnace environments: heating rates, temperature profiles, and gas flow rates were all chosen to be the same across both techniques. Additionally, a DSC crucible with a pinhole is utilized for both experiments. This consistent experimental setup enables more accurate comparative analysis and interpretation of the data.

LiFSI salts are gaining significant interest in the field of next-generation LIBs and lithium-metal batteries, mainly due to their unique properties that could enable higher columbic efficiencies (and hence higher energy densities). We apply our methodology on LiFSI-based electrolytes that use DMC and DME solvents.

The 3.0M and 5.0M LiFSI-DMC electrolyte solutions exhibits distinctive thermal behavior, characterized by a strong exothermic peak at 348°C.Prior to the strong exothermic peak observed at 350°C, the solution undergoes a phase of evaporation with no significant heat exchange, as evidenced by DSC analysis. This indicates that until the temperature reaches 350°C, the electrolyte solution predominantly experiences only physical changes, i.e., the transformation from the liquid to gas phase, without involving any chemical transformations. The occurrence of a strong exothermic peak at 350°C suggests a substantial decomposition reaction within the electrolyte solution. This reaction releases heat, leading to the drop observed in the DSC curve. It is likely that this reaction involves the breakdown of LiFSI and/or DMC or a reaction between them.

Our analysis shows that this is different from the LiFSI-DME electrolyte solutions which have a pronounced exothermic peak, observed at 210°C for both concentrations, points to a substantial reaction or phase transition within the electrolyte solutions. This reaction is exothermic, indicating that it releases heat, which is a characteristic of many decomposition reactions. This exothermic peak is followed by an endothermic trough at 303°C suggests a heat-absorbing process within the electrolyte solutions. This could potentially be associated with another phase transition or a particular reaction that absorbs heat, indicating that the system goes through another significant change at this temperature.

The contrast between the thermal behaviors of LiFSI-DMC and LiFSI-DME is significant. Where the former only displays a significant heat-releasing reaction at 348°C, the LiFSI-DME electrolyte solutions commence their exothermic reactions much earlier, at 210°C. This indicates that different classes of solvents can significantly

influence the thermal behavior of the electrolyte solution, leading to various reaction thresholds and thermal profiles. We further confirmed this by running the same TGA and DSC analysis on tetraglyme. Both tetraglyme and DME belong to the same class of solvents - ethers. Similar to DME, thermal analysis on tetraglyme showed that it exhibited an exothermic peak in the 200°C range (specifically, at 238°C).

5.2 Future Work

For future research directions, we aim to employ additional analytical tools to expand our understanding of the thermal behavior of lithium-ion battery components. Specifically, we plan to use Mass Spectrometry (MS) or Gas Chromatography (GC) to analyze the gases produced during the thermal decomposition processes. These techniques will provide information about the nature and composition of the gases evolved, allowing us to understand the exact reactions taking place and identify any potentially hazardous species released. Once we have collected these data, we can develop chemical kinetic mechanisms for different concentrations of LiFSI in various classes of solvents. Understanding the kinetics of these systems is vital to understanding the rate at which the reactions occur under different conditions, which directly impacts the thermal behavior and safety of the battery system.

We also plan to extend our investigations to the thermal behavior of specific cathodes and anodes used in conjunction with these particular electrolyte formulations. By examining these components in conjunction, we can better understand the overall effects that arise from their interactions, providing a more holistic and realistic perspective on the thermal safety of these next-generation LIBs.

Chapter 6

Bonus - Techno-economic Analysis on Sodium-ion Batteries!

6.1 Background and Motivation

While LIBs have become the dominant technology for portable electronics and EVs, there are several factors that suggest it may be prudent to consider alternative electrochemical energy storage solutions. One key factor is the projected increase in demand for high-energy-density batteries, driven in part by the rapid growth of the EV market (see Figure 2-6). This demand will put pressure on the supply of critical materials such as lithium, cobalt, and nickel, which are all used in LIBs. While the price of LIB has been dropping for the past 30 years (see Figure 2-1), the cost of its raw materials has become volatile in recent years, which can create uncertainty and risk for companies that rely on LIBs. For example, the price of lithium has jumped more than 600 percent from about $17,000 per metric tonne in January 2022 to over $70,000 in December 2022 [8, 10], as shown in Figure 6-1. This risk of further price increases and scarcity could be mitigated by exploring alternative electrochemical energy storage solutions that are less reliant on these materials.

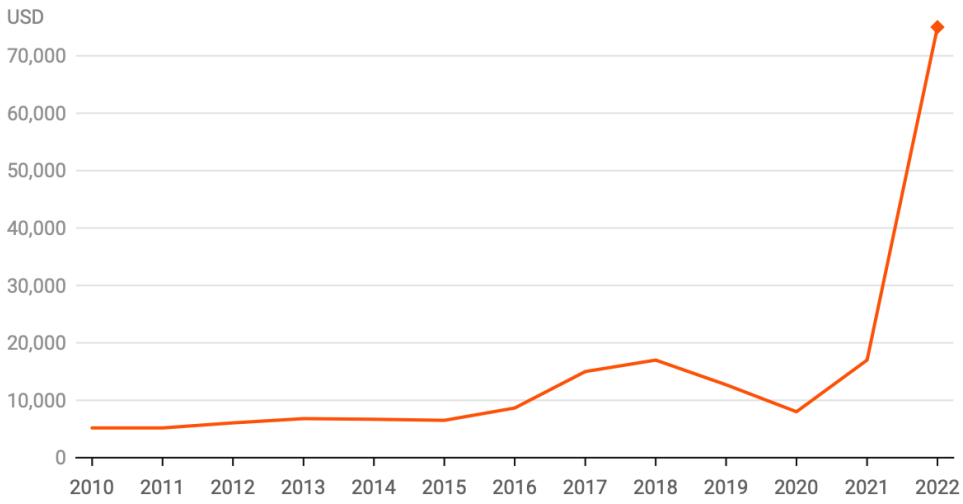

Figure 6-1: Price of battery-grade lithium carbonate per metric ton in U.S. dollars. Reproduced from [3].

NIBs operate similarly to LIBs where Na^+, instead of Li^+, transports and intercalates between the anode and cathode during charging and discharging. Hard carbon anodes are commonly used intercalation anodes used for NIBs. A schematic of an NIB is shown in Figure 6-2. The electrolyte used in NIBs is similar to those used in LIBs where sodium hexafluorophosphate ($NaPF_6$) salt, instead of $LiPF_6$, is used in an organic solvent like DMC or EC or a combination of those two. One major advantage of NIBs is that they do not rely on cathode materials such as lithium, cobalt, and nickel, which are commonly used in LIBs and can be expensive or subject to supply constraints. Instead, NIBs typically use more abundant and lower-cost materials such as manganese, iron, and sodium (which is the sixth most abundant element on Earth[15]). In fact, while increasing cobalt and nickel content in LIBs increases the energy density of the LIBs, it has little effect on the energy density of NIBs[73]. NIBs are known to have lower electrochemical efficiencies and energy densities compared to LIBs, which makes them less attractive for portable electronic devices and EVs, where energy density is critical. NIBs are proposed by the scientific community to be complements to LIBs in large-scale stationary energy storage applications, in which energy density is not as critical.

Since NIBs are not commercially available yet, extensive research and development

are still required to make them viable for practical applications. However, significant progress has been made in recent years, and there is growing interest in the potential of NIBs especially when energy density (size of battery) is not of significant importance (i.e., in large-scale stationary energy storage).

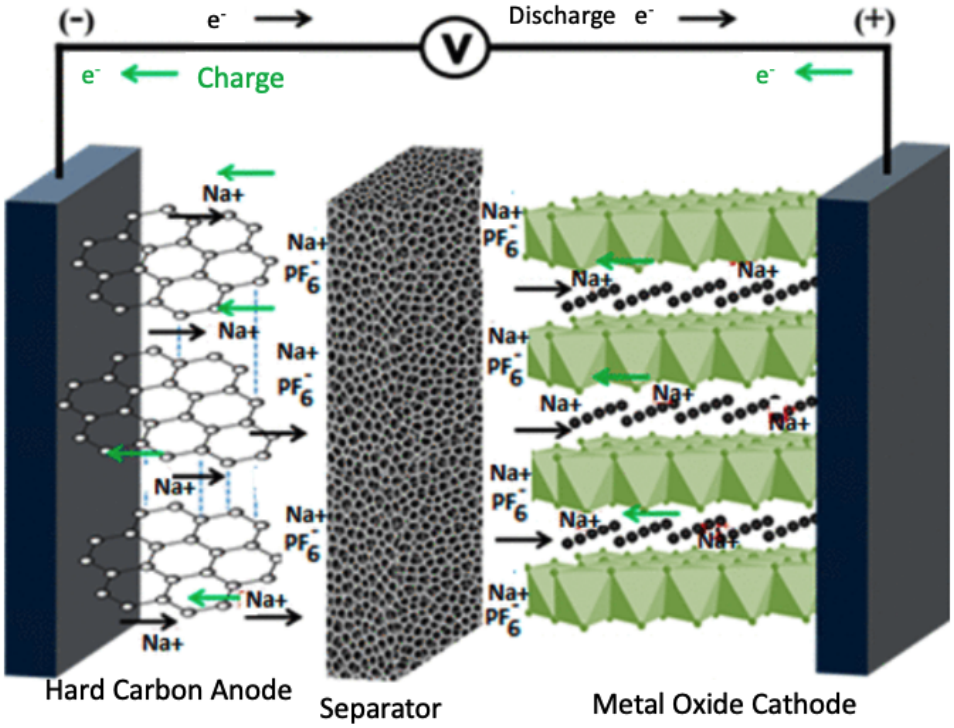

Figure 6-2: Schematic of NIB. Adapted from [21].

6.2 Importance of Cathodes

The cathode is a crucial component of a battery systems and greatly influences its overall performance, including the cell voltage, capacity, and cycle stability. Given that the cathode active material (CAM) is both the most expensive component of and the main differentiator between LIBs and NIBs, it is important to conduct a cost analysis of CAMs. The cost of the CAM can vary depending on factors such as the specific material used, its purity, production methods, and market demand. For LIBs, the cost of the CAM depends on the battery chemistry and ranges between 40-60% of the total cost[63]. The exact cost breakdown of CAM remains mostly undisclosed due to a multitude of strategic, competitive, and economic reasons. This confidentiality helps manufacturers maintain their competitive edge in the market, influence market perception, and secure their financial performance. In the competitive landscape of battery manufacturing, proprietary information can equate to a significant advantage. Moreover, if the detailed cost structure of a product is made public, it could influence the perceived value of the product and potentially impact a company's pricing strategy. Customers or competitors might argue that the product is overpriced if they know how much it costs to produce. By keeping costs confidential, manufacturers have more flexibility in their pricing strategies. A study conducted by Wentker et al. employed a bottom-up approach to model the cost breakdown of the CAM, relying heavily on the actual material costs[63]. Their findings suggested that these material costs constitute approximately 60% of the total CAM costs, with the remainder attributable to the expenses incurred during processing and manufacturing (see Figure 6-3 and Figure 6-4).

Layered metal oxides (LMOs) are among the major classes of materials being researched for use as CAMs in NIBs because of the material class's simple structure, synthesis, and potential for scalability. In our work, we developed a process-based cost model (PBCM) that calculates the cost of manufacturing a LMO-based NIB CAM and identifies scalability challenges. A PBCM is a detailed cost model that

estimates the total costs as a sum of a series of specific processes and unit operations, each with an associated cost. It is often used in manufacturing or production to assess costs that includes materials, labor, equipment, overheads, and any other costs directly or indirectly related to the process. The main advantage of a PBCM is that it provides detailed data of where costs are incurred. This can help in identifying of potential bottlenecks and hence scalability challenges. Cost modeling of CAM is less common than that of battery- and pack-level cost modeling[32]. The Argonne National Laboratory Battery Manufacturing Cost Estimation (BatPaC) is the major model used in academia for estimating the cost of manufacturing LIBs. BatPac does not calculate the cost of CAMs but rather take takes the cost of a CAM as an input into the model. In light of these considerations, our LMO-based NIB CAM PBCM can serve as an essential tool to fill the gap in manufacturing and scalability challenges of NIB. It provides detailed insights into the manufacturing cost structure of CAMs.

In order to obtain equipment specifications and information regarding unit operations for CAM manufacturing, multiple expert interviews were conducted with equipment vendors, academics, and applied scientists and engineers that work in LIB battery manufacturing (due to the absence of NIB manufacturing).

Process	Labor (hr/yr)	Capital Equipment ($M)*	Plant Area (m^2)
Materials preparation/mixing			
Positive	200,000	200	8,000
Negative	270,000	280	8,800
Electrode coating			
Positive	59,000	90	16,000
Negative	59,000	78	16,000
Calendaring			
Positive	61,000	25	2,100
Negative	69,000	25	2,100
Notching			
Positive	250,000	29	3,200
Negative	250,000	29	3,200
Electrode vacuum drying			
Positive	41,000	14	2,000
Negative	35,000	11	1,600
Cell assembly in dry room			
Electrode slitting†	260,000	30	-
Cell stacking	700,000	170	-
Current collector welding	190,000	190	-
X-ray inspection	190,000	14	-
Inserting cell in container	49,000	11	-
Electrolyte filling & cell sealing	132,000	25	-
Dry room	8,000	7.3	61,000
Formation cycling, testing, and sealing	560,000	830	110,000
Module assembly	170,000	94	27,000
Pack assembly and testing	150,000	94	27,000
Warehouse	31,000	200	10,000
Building and supporting systems			
Building	-	1,700	-
Solvent recovery	17,000	36	1,100
Rejected cell and scrap recycle	38,000	9.3	3,300
Control laboratory	46,000	16	1,300
Total	3,876,000	4,222	305,700

†both electrodes
*cost includes installation

Table 6.1: BatPac processes. Labor, capital equipment, and plant area for each process step in the baseline plant case. Reproduced from [45].

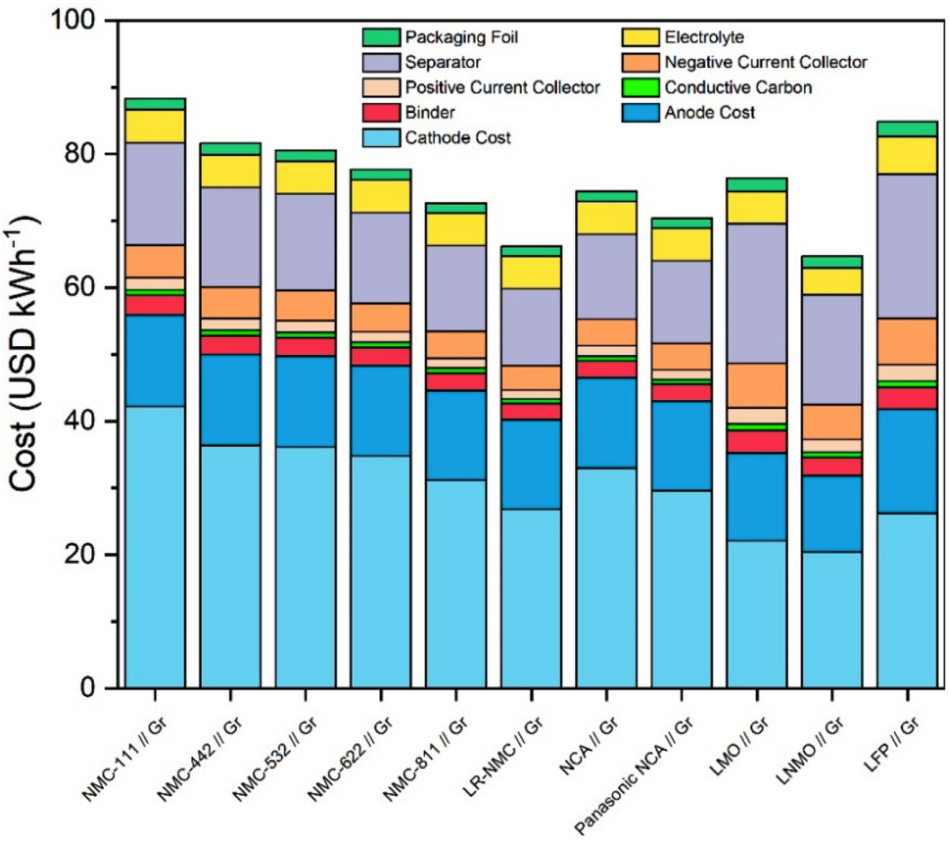

Figure 6-3: LIB cost breakdown by component. Reproduced from [63].

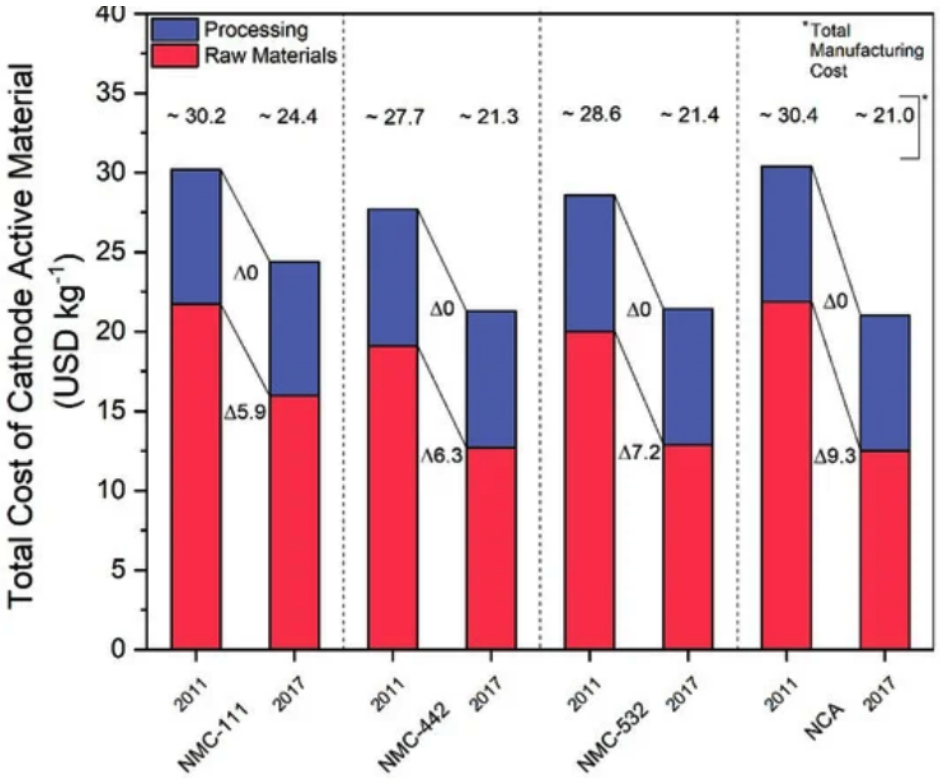

Figure 6-4: Materials and processing costs of cathode active materials of LIBs. Reproduced from [63].

6.3 Equipment

For our PBCM, we conducted interviews with machine vendors, applied engineers, and scientists that work for LIB manufacutring companies to determine the costs and operational parameters of the equipment used in our model. These parameters, which include cost, processing rates, floorspace requirement, number of workers necessary, and power consumption, are presented in Table 6.2.

Equipment	**Unit Cost (USD)**	**Processing Rate (L/hr)**	**Direct Workers**	**Indirect Workers**	**Power (kW)**	**Floorspace (m^2)**
Solid-state mixer	300,000	1,600	0.5	0.25	15	20
Solid-state dryer	1,500,000	1,000	1	0.5	20	20
Liquid-state reactor	700,000	1,900	1	0.25	15	115
Filter press	1,500,000	2,000	2	0.5	15	10
Furnace	1,500,000	1,000	1	0.25	50	40
Electrospinning unit	150,000	0.1	0.5	0.25	20	10

Table 6.2: Equipment details.

6.3.1 Solid-state Mixers

Solid-state mixing is required in co-precipitation synthesis to mix salts before they are dissolved in a solvent for solution preparation,and in solid-state synthesis for effectively mixing solid salt particles before sintering.

Ribbon and paddle mixers are types of horizontal trough mixers designed for typically mixing dry powders and small granule salts, respectively. Ribbon mixers have a double helix design that allows for efficient and consistent mixing. The mixer is designed with an inner and outer ribbon that moves materials in opposite directions for thorough blending. Paddle mixers, on the other hand, have paddle-shaped blades attached to a rotating shaft. These blades mix and blend the material as they rotate. Paddle mixers can handle more dense particles. Given that they are horizontal, dead-spots (areas within the mixer where movement/ mixing is minimal) are observed. The

typical range for mixing time is 15-20 min. Ribbon and paddle mixers can only achieve up to 98% discharge since they are horizontal.

Tumble blenders (tumbling mixers) are alternatives to horizontal trough mixers like ribbon and paddle mixers when uniformity of mix and minimization of dead zones are of primary concern. The working principle of a tumble blender involves rotating or 'tumbling' the entire mixing vessel along a horizontal axis. This causes the materials inside to be lifted, sheared, and folded together, which results in high uniform mixing. Tumbling also helps break up any agglomerates that might form during the mixing process. Agitator bars may be added to tumble blenders to ensure particle deagglomeration, size reduction, and ultimately a more homogeneous and consistent mix. The use of agitator bars is only necessary when dealing with lower percentages of certain constituents in a mix, typically if a constituent salt in a desired mixture is below 10%. While the typical mixing time is between 15-20 min per batch, batch loading and unloading time adds a total of another 10-15 min, making tumble blenders slower than ribbon and paddle mixers.

The choice of mixer often depends on the properties of the solids being mixed, including its abrasiveness. The power of the motor is also dictated by the salt density. If the material is abrasive, tumble blenders and paddle mixers are used since they are gentle when mixing. Tumble blenders can handle higher bulk densities and 100% discharge. If material is non-abrasive, ribbon mixers can be used. Ultimately, the experts interviewed in the battery industry have reported using both paddle mixers and tumble blenders for mixing salts.

6.3.2 Solid-state (Cake) Dryers

Solid-state drying, also known as cake drying on an industrial scale, is a process that is similar to solid-state mixing, but with the addition of heat and vacuum conditions,to allow for drying. This process is often used to remove moisture from a solid material,

after it has been filtered and formed into a "cake" or solid mass.

Tumble blenders can be used for drying certain materials, if there is evidence that the material will form a free-flowing powder as it dries and not agglomerate. Static drying may be required for part of the process as the mixture dries, before any tumble can occur. Some experts have reported that tumble blenders are not suitable for vacuum drying of wet cakes (slurry, paste). Adding an agitator to tumble blender adds complexity to the system causing the final particles to be more "fluffy".

Vertical cone screw blenders are mixers that utilize a rotating screw agitator within a conical vessel to lift and fold materials, ensuring comprehensive mixing and exposure to drying conditions. Double planetary mixers are mixers with two blades that perform a dual action: rotating on their own axes and orbiting the mix vessel simultaneously. By modulating the mixing speed, one can regulate the texture or "fluffiness" of the dried output.

The important factor in drying with these mixers is the turnover of particles: as long as the particles are being continuously moved and exposed to the drying conditions, the drying process should proceed effectively. It is hard to know the drying time beforehand as that requires trial-and-error to sample and check for the moisture level. The experts interviewed have mentioned that some manufacturers tend to overshoot by 12-20 hours drying, where only a few hours of drying may be needed, close to 5-7 hours.

Lab-scale synthesis routes use vacuum ovens to dry the precipitates. On an industrial scale, the precipitates are in a slurry and upon filter-pressing, are in a wet cake. To dry the cake, it is placed in an industrial dryer that is made up of a mixer that is vacuumed rated. The drying temperature range is typically between 90-120°C. Vigorous agitation should not occur as that may lead to "fluffiness" in the dried solid particles, which is an adverse effect as only high-tap density particles are of value. Some manufacturers have reported compressing or pelletizing the powder if it is fluffy.

6.3.3 Liquid-state Mixers

Synthesis by co-precipitation is a desirable method as it allows for particle size control. The co-precipitation step involves the gradual mixing of two solutions into a reactor. A metal cation solution is prepared by dissolving metal salts into deionized (DI) water and in some cases in a sulfuric acid solution, as some salts such as $MnSO_4$ precipitate in DI water. A basic buffer solution with pH of 14 is also prepared by dissolving NaOH and NH_4OH in DI water. A starting solution in the reactor is the basic buffer solution. While the system can be exposed to atmospheric oxygen before or after the mixing occurs, the system can be purged with Nitrogen when it is undergoing mixing to obtain the highest yield[30]. The salt and basic solution are gradually added to the reactor via a flow control valve and a spray nozzle where the solutions are sprayed above the reactor liquid line. The reactor initially contains a buffer solution, and that is to ensure that the pH of the solution remains constant in range of 10-12 as the solutions are gradually added. The addition of the solutions to the reactor takes about 1 hour; however, continuous mixing occurs for at least 10 hours - that is when precipitation occurs. High and steady stirring speeds are required to ensure the proper morphology of precipitate solids (typically at 800RPM)[46]. The reactor is kept under an isothermal temperature of about 50°C.

6.3.4 Filtration

A filter press is used to separate solids and liquids in a slurry through pressure. The total pressure is applied first by applying a mechanical pressure on the plates followed by pumping at high pressure the slurry through the press. The press is made up of numerous plates with filter cloths in between them. The nature and the mass ratios of the solids and liquids in the slurry are defining factors of the characteristics of the filter press. The mechanical pressure applied is to remove as much liquid as possible. The residual solid cake is then vacuum dried to recover the

Automated filter presses are more common as they are significantly less labor intensive. Fully automated and advanced programmable logic controllers (PLCs) can keep filter-pressing up to the point when liquid is no longer exiting from the bottom of the plates. Such PLCs are adaptive and self adjusting to the unique composition of the slurry. More conventional automated filter-presses have a set-point for the pressure or time of filtering.

High pressure filter-presses, typically those that operate at 16-21 bar, produce dryer cakes than those that operate at averages pressures (7-15 bar). Blow dryers installed in the filter press are unnecessary as they decrease moisture content by only 1-2% by mass. High pressure filter-presses also have shorter filtration cycles (30-40min) compared to those that operate at average pressures (1-2hours). The filtration time is independent on the size of the length of the filter press (number of plates) and is rather a function of operating pressure.

Membrane plates are used for niche applications when the filter press cannot be operated at high pressure. The membrane plates can swell or "squeeze" in to remove excess liquid, as opposed to standard plates that are rigid. A mixture can be pumped in at low pressure, and rely on the "squeeze" pressure that occurs through the inflation of the membrane. Membrane presses are more expensive and need to be replaced more often since they break more.

Only about 0.1% of solids will pass into the liquid stream, and that occurs at the beginning when the cake is forming and starting to cover the porous plates.High pressure filter-presses also have shorter filtration cycles (30-40min) compared to those that operate at average pressures (1-2 hours). The filtration time is independent on the size of the length of the filter press (number of plates) and is rather a function of operating pressure.

The solution exiting the reactor is placed in a holding tank as it is gradually discharged into the filter press. This will allow the filtration process occur in smaller batches throughout the shift, decreasing the size (and cost) of the filter. This will

allow the solution is allowed to cool to room temperature. This will also ensure that a homogeneous solution is fed into the filter press.

Full washing with water is not required as that will add to wastewater stream; however, rinsing with water is required after the discharge of the cake from the press, in order to ensure full removal of remaining solids on the plates. The addition of more plates (i.e. increase of size of filter press) will not necessarily decrease the filtration time. Filtration time varies from 10-15 minutes in filtration of mining slurry (solid% $> 50\%$) to 3-4 hours in 1% sludge wastewater.

6.3.5 Furnace

Both calcination and sintering are thermal processing techniques used in CAM synthesis. Sintering is the process of applying heat to a powdered material in a way that it maintains its shape while bonding the particles. Calcination is a heat treatment process where solids are heated at high temperatures in absence or limited supply of air.

The industrial furnaces that are utilize during CAM synthesis are conveyor belt furnaces which allow for large quantities of a powder material to be processed continuously in a controlled environment. These furnaces operate by placing the CAM on rollers, which are then placed on a conveyor belt and pushed into the furnace.

The powders are are loaded onto the conveyor belt at one end of the furnace at room temperature. The conveyor belt moves the material through different zones. In the preheating zone, the temperature starts to rise to prepare the material for the main heating process. The material then enters the main heating zone, where it is held at a high temperature to achieve the desired process before moving into the cooling zone where it cools down before exiting the furnace. Furnaces can have multiple heating zones if 2-step heatings are required.

The power consumption of the process largely depends on the insulation efficiency of the furnace. The nickel content of the CAM dictates the environment in which the sintering process can be conducted. If the Ni content is less than 50%, sintering can be performed in an air environment. However, if the Ni content is more than 50%, a pure oxygen environment is needed, which significantly increases the cost (about $4/kg-CAM according to one manufacturer).

6.3.6 Electrospinning

Electrospinning is a fiber production method which uses electric force to draw charged threads of polymer solutions or polymer melts up to fiber diameters on the micro to nanoscale order. It is a versatile technique for fabricating fibrous structures using various polymers. In industry, roll-to-roll (or roller) electrospinning system are used where the substrate material continuously passes through the electrospinning area, which allows for the continuous production of nanofibers on a large scale. Roll-to-roll electrospinning systems use multiple needles, often arranged in several rows. The purpose of using multiple needles is to increase the productivity of the electrospinning process. 10-20 needles per row with 3-5 rows are feasible configurations, but the precise arrangement can vary significantly depending on the specifics of the production process and the properties of the materials being used.

Each needle typically dispenses on the order of 1mL of precursor solution per hour. The flowrate can be adjusted depending on the specific materials used, the desired properties of the final product, and the characteristics of the electrospinning setup. The extruding speed is the speed at which the polymer solution is extruded from the nozzle and deposited on the collector. The extrusion speed is largely limited by the physical properties of the polymer solution, particularly its viscosity and surface tension.

6.4 Model Architecture

The PBCM is implemented in Python and comprises various modules that work together to calculate NIB CAM cost in USD per kg. The model requires a user-defined annual CAM flowrate and synthesis route input, which should include the chemicals used, the necessary unit operations, and the stoichiometry of the involved reactions. By allowing users to input specific case parameters, the model then computes the corresponding CAM costs. A schematic of the model architecture is presented in Figure 6-5. In cases where specific cost and price values, such as equipment and chemical costs, are unavailable for the year 2022, the model adjusts them for inflation using the Chemical Engineering Plant Cost Index (CEPCI).

6.4.1 Continuity

The **continuity** module in the PBCM calculates the material flows for each process step. This module begins with the user-defined annual CAM (product) flowrate, typically set at 6,500 tonnes per year. Using this initial flowrate, the continuity module performs a back-calculation to determine the overall material quantity required and the material flowrate through each unit operation or equipment involved in the process.

By working in reverse, the continuity module enables the determination of the necessary material quantities and flowrates to achieve the desired annual CAM flowrate. This information is required for evaluating the associated material requirements at each step of the production process.

Within this module, unit conversions play a significant role in converting the required flowrate, measured in tonnes per year, into molar and volumetric flowrates. These conversions are necessary for conducting stoichiometric calculations and determining the appropriate sizing of equipment. By converting the flowrate from tonnes

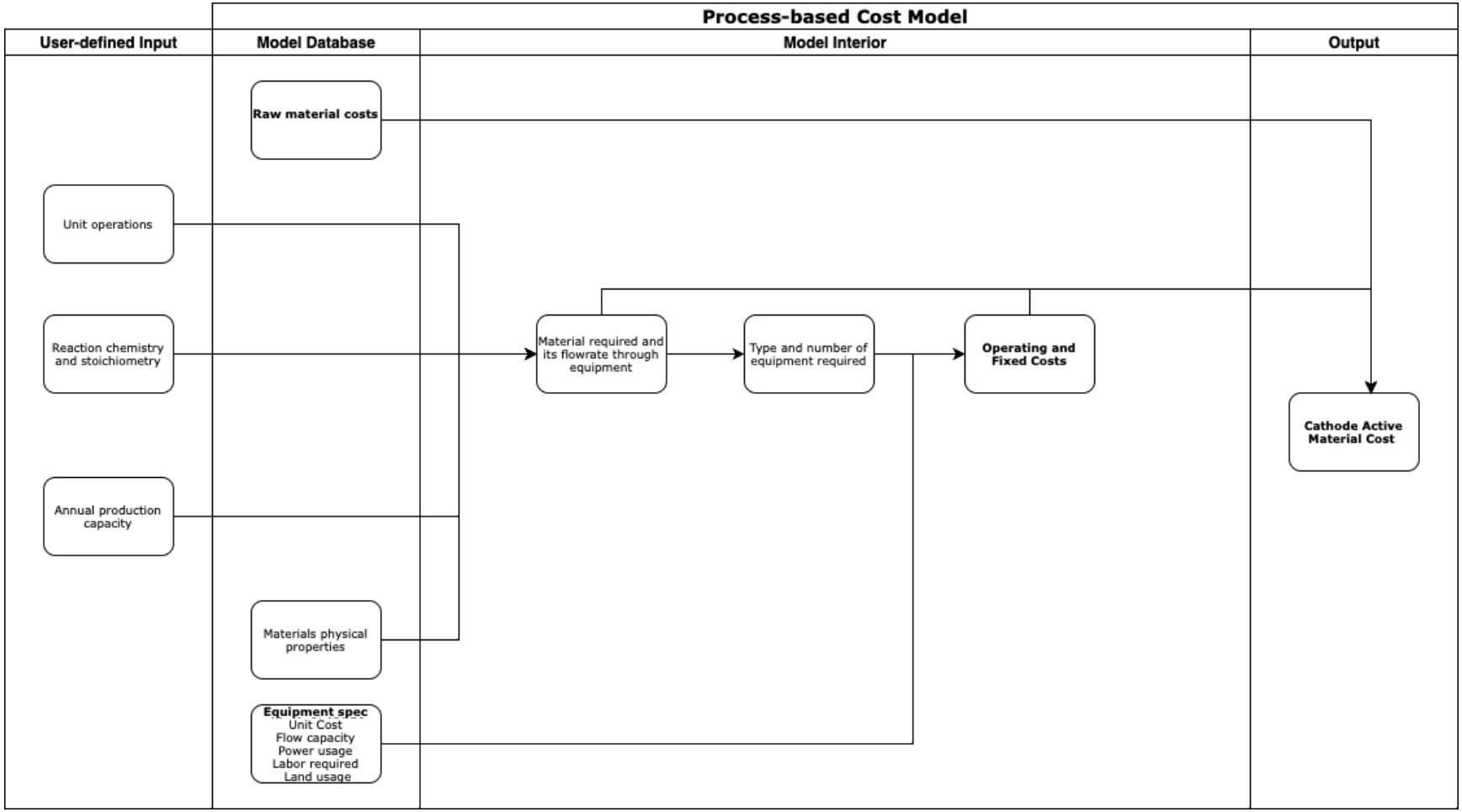

Figure 6-5: Model architecture.

per year to molar flowrate, the module enables the utilization of stoichiometric calculations that rely on molar quantities of reactants and products. The conversion to volumetric flowrate facilitates equipment sizing calculations as equipment capacities and processing rates have been specified in terms of volumetric throughput (see Table 6.2).

The model is currently limited to handling reactions with a single product, without considering any side reactions. Ther are further model assumptions and limitations:

- Accumulation is assumed to be zero for all process steps.
- 100% conversion is assumed for all reactions, meaning there are no remaining reactants after the reactions have occurred.
- No recycle streams are incorporated.

6.4.2 Processes

The **processes** module takes multiple input parameters, primarily the volumetric flowrates, from the **continuity** module.

$$\text{Annual Production Flowrate [L/yr]} = \frac{\text{Annual Production Capacity [kg-CAM/yr]}}{\text{Density [L/kg]}} \tag{6.1}$$

$$\text{Unit Cost Installed[\$]} = \text{ESI} \times \text{Unit Cost[\$]} \tag{6.2}$$

$$\text{Annual Production Time [h/yr]} = \frac{\text{Annual Production Flowrate [L/yr]}}{\text{Equipment Processing Rate [L/h]}} \tag{6.3}$$

$$\text{Annual Available Paid Time [h/yr]} = \text{ODPY} \times (24 - \text{PUDT}) \tag{6.4}$$

$$\text{Line Uptime [h/yr]} = \text{ODPY} \times (24 - \text{UPDT} - \text{PMT} - \text{PUDT}) \tag{6.5}$$

Parameter	Symbol	Value	Units
Operating Days per Year	ODPY	350	days / year
Operating Hours per Day	OHPY	21	hours / day
Wages		35.00	$ / hr
Unit Electricity Cost		0.09	$ / kWh
Unit Water Cost		0.003	$ / L
Discount Rate	r	10	%
Building Unit Cost		1,500	$ / m^2
Building Lifetime	BLT	30	years
Building Height		7	m
Dryroom Unit Cost		1270	$/ m^3
Planned Unpaid Downtime	PUDT	1	hour
Planned Maintenance Time	PMT	1	hour
Unplanned Downtime	UPDT	1	hour
Equipment Lifetime	ELT	20	year
Equipment Shipping and Installation Factor	ESI	4	

Table 6.3: PBCM parameters.

Equipment Cost

$$\text{Number of Equip Utilized} = \frac{\text{Annual Production Time [h/yr]}}{\text{Line Uptime [h/yr]}} \tag{6.6}$$

$$\text{Number of Equip Needed} = \text{ceil}(\text{Number of Equip Utilized}) \tag{6.7}$$

$$\text{Equip Invested[\$]} = \text{Number of Equip Needed} \times \text{Unit Cost Installed[\$]} \tag{6.8}$$

$$\text{Annual Equip Cost [\$/yr]} = \text{Equipment Invested[\$]} \left(\frac{r(1+r)^{\text{ELT}}}{(1+r)^{\text{ELT}} - 1} \right) \tag{6.9}$$

Building Cost

$$\text{Equip Floorspace } [\text{m}^2] = \text{Number of Equip Needed} \times \text{Unit Equip Floorspace } [\text{m}^2] \tag{6.10}$$

$$\text{Building Investment}[\$] = \text{Equip Floorspace}[\text{m}^2] \times \text{Building Unit Cost}[\$/\text{m}^2] \tag{6.11}$$

$$\text{Annual Building Cost}[\$/\text{yr}] = \text{Building Investment } [\$] \left(\frac{r(1+r)^{\text{BLT}}}{(1+r)^{\text{BLT}} - 1} \right) \tag{6.12}$$

Labor Cost

$$\begin{aligned} \text{Annual Labor Cost } [\$/\text{yr}] = \text{Wages } [\$/\text{h}] \times \text{Number of Direct Workers} \\ \times \text{Annual Available Paid Time}[\text{h/yr}] \times \text{Number of Equip Utilized} \end{aligned} \tag{6.13}$$

Electricity Cost

$$\text{Total Electricity } [\text{kWh/yr}] = \text{Annual Production Time } [\text{h/yr}] \times \text{Equipment Power } [\text{kW}] \tag{6.14}$$

$$\text{Annual Energy Cost } [\$/\text{yr}] = \text{Unit Cost Electricity } [\$/\text{kWh}] \times \text{Total Electricity } [\text{kW/yr}] \tag{6.15}$$

The unit cost of electricity is based on the average industrial electricity cost in the U.S.

Overhead Cost

$$\text{Annual Overhead Cost [\$/yr]} = \text{Wages [\$/h]} \times \text{Number of Indirect Workers} \times \text{Annual Available Paid Time [h/yr]} \times \text{Number of Equip Utilized} \tag{6.16}$$

Maintenance Cost

The maintenance cost is assumed to be 10% of the total of annual overhead, building, and equipment cost.

$$\text{Annual Maintenance Cost [\$/yr]} = 0.1 \times (\text{Annual Overhead Cost} + \text{Annual Building Cost} + \text{Annual Equipment Cost}) \tag{6.17}$$

Dryroom Cost

A dry room is a critical component of many manufacturing processes, particularly in the fabrication of LIBs and NIBs. The organic-based electrolyte used in these batteries can be very sensitive to moisture due to its reactivity, and therefore it is crucial to maintain a strictly controlled, low-humidity environment when filling the cells. A dry room needs to maintain a moisture concentration below 100 parts per million by volume (ppmv). This extremely low level of moisture helps to prevent unwanted reactions between the electrolyte and water, which can degrade the battery's performance. Our cost model draws upon a model of an LIB manufacturing plant that focuses on the management of humidity in its dry room[22]. Equipment can be specified to be put into a dry room. The user will also input the dry room height. The door of the dry room will be opened and closed approximately 120 times per day. The relative humidity of the make-up air (the air that is brought in from outside to replace the air that has been exhausted from the room) is 50%. The study estimates

that a dry room will cost \$1270/m³ [22].

$$\text{Equip Volume } [\text{m}^3] = \text{Equip Floorspace } [\text{m}^2] \times \text{Building Height } [\text{m}] \tag{6.18}$$

$$\text{Annual Dryroom Cost } [\$/\text{yr}] = \text{Equip Volume } [\text{m}^3] \times \text{Dryroom Unit Cost } [\$/\text{m}^3] \tag{6.19}$$

Material Cost

To ensure the most accurate reflection of the industrial pricing of the chemicals involved in our study, we gathered data using a \$/tonne pricing scale. Lab-scale chemical prices, which are generally reported in \$/g and \$/kg, were intentionally avoided in our study. Chemical pricing at these scales often include considerable markups due to the cost of purification, packaging, and distribution associated with smaller quantities. These prices do not reflect the economic realities of industrial chemical production, where economies of scale drastically lower per-unit costs. We utilized the following cross-commodity price reporting databases: U.S. Geological Survey, Texas A&M University Libraries Chemical Pricing Database, ICIS Chemical Business, London Metal Exchange, Shanghai Metals Market, and Fastmarkets. As mentioned, if 2022 prices were unavailable, the CEPCI was used to convert prices from earlier years into 2022 prices.

$$\text{Annual Material Cost } [\$/\text{yr}] = \text{Annual Production Capacity } [\text{kg-CAM/yr}] \times \sum_i \alpha_i \cdot P_i \tag{6.20}$$

where for precursor i, α_i is the mass ratio with respect to 1 kg of CAM (determined from the reaction stoichiometry) and P_i is the chemical price in \$/kg (converted from \$/tonne).

Net Cost in \$/kg

$$\begin{aligned}\text{Annual Total Cost} = {} & \text{Annual Material Cost} + \text{Annual Equipment Cost} + \text{Annual Building Cost} \\ & + \text{Annual Maintenance Cost} + \text{Annual Overhead Cost} + \text{Annual Labor Cost} \\ & + \text{Annual Energy Cost} + \text{Annual Dryroom Cost}\end{aligned} \tag{6.21}$$

$$\text{Net Cost [\$/kg-CAM]} = \frac{\text{Annual Total Cost [\$/yr]}}{\text{Annual Production Capacity [kg-CAM/yr]}} \tag{6.22}$$

6.5 Model Validation

Because of the competitive nature of the LIB industry and the sensitive nature of **cost** data, it is unsurprising that no company-specific data is available for LIB CAMs **costs**. Moreover, NIB CAM costs are not available since they are not commercial yet. cProf. Jessika Trancik's group at MIT compiled hundreds of price data points for several LIB CAMs, which notably includes Nickel Manganese Cobalt (NMC)[71]. This dataset is a highly valuable resource, comprising 1057 records sourced from approximately 280 references[71]. To develop estimates of representative values, Ziegler et al. took an approach of averaging CAM prices over five-year periods from 1995-2000 and 2010 to 2015, as shown in Figure 6-6.

To test the accuracy of our cost model, we have chosen to validate it against NMC using material and equipment costs and prices exclusively from the 2010-2015 period. The average $LiNi_{1/3}Mn_{1/3}Co_{1/3}O_2$ NMC **price** during that period is \$33/kg. A key

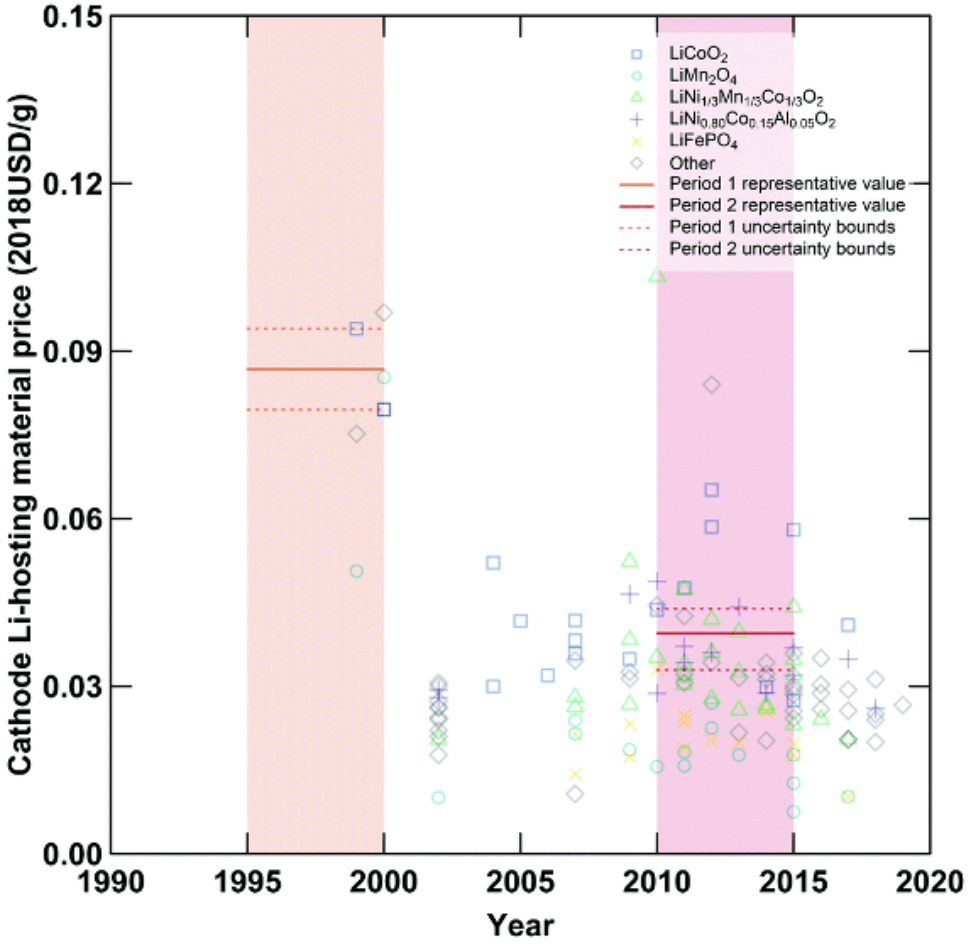

Figure 6-6: Specific prices of various LIB CAMs with focus on 1995-2000 and 2010-2015 periods. Adapted from [71].

assumption underlying our validation process is that the manufacturing process for NMC cathodes has not undergone significant changes since the early 2010s. This is based on the premise that while improvements and optimizations have certainly been made over the years, the fundamental steps in the production process, such as mixing, drying, and calcining have largely remained the same.

In our validation process, we first collect data on material costs and prices from the 2010-2015 period. This includes the prices of key raw materials such as nickel, manganese, cobalt, and lithium.

Year	**CEPCI**
2015	556.8
2014	576.1
2013	567.3
2012	584.6
2011	585.7
2010	550.8

Table 6.4: CEPCI during period of 2010-2015.

The average CEPCI between the period of 2010-2015 is 570. The equipment cost was adjusted to the CEPCI value of 570.

Material	**Average price per tonne**
Co-metal	\$31,500
Ni-metal	\$17,600
LiOH	\$6,670

Table 6.5: Average material price during the 2010-2015 period.

Identity	**Status**	**Solid-state mix**	**Liquid-state mix**	**Filter Press**	**Cake Dry**	**Calcine**
$NiSO_4{\cdot}6H_2O$	Precursor	0.33	0.33	0.33	0	0
$MnSO_4{\cdot}5H_2O$	Precursor	0.33	0.33	0.33	0	0
$CoSO_4$	Precursor	0.33	0.33	0.33	0	0
NH_4OH [2M]	Precursor	0	1	1	0	0
$[Ni_{0.33}Mn_{0.33}Co_{0.33}](NH_4)_2(OH)_2$	Intermediate	0	0	0	1	1
LiOH(s)	Precursor	0	0	0	0	1
$LiNi_{1/3}Mn_{1/3}Co_{1/3}O_2$	Product					

Table 6.6: Status of chemicals in the NMC333 production process.

Using our model, the NMC333 **cost** in the 2010-2015 period is calculated to be \$23.8/kg (Table 6.7). The average NMC333 **price** during that period is \$33/kg[71]. This implies that the average profit margin, using the data we calculated, is 27.8%. This figure falls within the profit margin range of 15-30% for the LIB energy storage industry, which we established through expert interviews and examination of various online databases[12].

$$\left(\frac{\$33/kg - \$23.8/kg}{\$33/kg}\right) = 27.8\%$$

This validation for our cost model is important given the lack of readily available cost data in the LIB industry due to its competitive nature.

	Cost (\$/kg)
Material	20.1
Equipment	2.17
Building	0.029
Overhead	0.304
Maintenance	0.250
Labor	0.865
Energy	0.035
Total NMC333 Cost	23.8

Table 6.7: Cost breakdown of NMC333.

6.6 Converting into Units of Cost per Unit Energy

The cost per unit mass ($/kg) of a CAM can be converted to cost per unit energy ($/kWh) to provide a way to compare the cost effectiveness of different CAM technologies, as the energy density of a CAM may offset the CAM materials cost and can make a more expensive material more cost-effective. Tracking the cost per kWh over time can help illustrate the progress made in improving battery technologies.

The conversion of $/kg of CAM to $/kWh typically requires the specific energy of the CAM measured in Wh/kg. For emerging technologies such as NIBs, that value is not well characterized or consistent yet. Instead, we rely on the specific charge and discharge capacity values that are reported in literature. The specific discharge capacity versus the number of cycles is a key metric frequently used in literature to understand the performance of a cell. It tracks the change in the amount of energy a cell can deliver as the cell is charged and discharged.

In order to be able to compare cell cost performances across different CAM configurations, especially since we are considering materials that are not fully matured and have not been extensively cycled, we decided to select the capacity at an intermediate value of 10 cycles. This allows for fair comparison across different CAM configurations as it provides a uniform, repeatable point of measure.

Method 1 - Using a Fixed Factor for Cost Conversion to Full Cell

Full Cell Specific Capacity Values

If the full-cell (FC) specific capacity value is reported, the conversion to the FC cost per kWh, Δ, is

$$\Delta\left[\frac{\$-\mathrm{FC}}{kWh-\mathrm{FC}}\right]=\delta\left[\frac{\$-\mathrm{CAM}}{kg-\mathrm{CAM}}\right]\times\frac{1}{\alpha}\left[\frac{\$-\mathrm{FC}}{\$-\mathrm{CAM}}\right]\times\frac{1}{\beta}\left[\frac{\mathrm{kg}-\mathrm{CAM}}{\mathrm{Ah}-\mathrm{FC}}\right]\times\frac{1}{\mathrm{OV}}\left[\frac{1}{\mathrm{V}}\right]\times\left[\frac{1000\mathrm{V}}{1\mathrm{kV}}\right] \tag{6.23}$$

where δ is output CAM cost from the PBCM, α is a factor that converts cost of CAM to cost of FC, β is the 10^{th} cycle FC specific capacity value which is usually reported per mass of CAM (mAh/g), and OV is the operating cell voltage (also known as the average working potential) in V. The factor α is typically around 30% (see Figure 6-3 for LIB case and Figure 6-7 for NIB case).

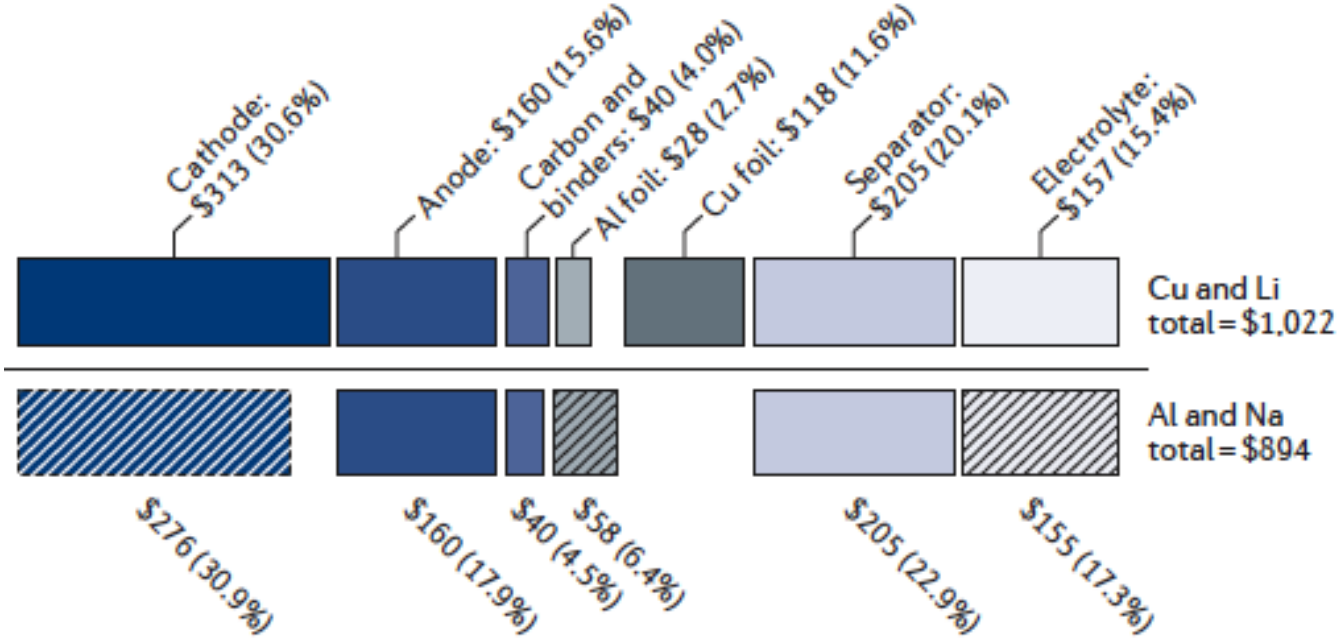

Figure 6-7: Calculated cell materials costs for a $LiMn_2O_4$-graphite LIB (top) and a theoretical $NaMnO_2$-hard carbon NIB (bottom) in which the copper foil is replaced with aluminium foil and lithium is replaced with sodium. Reproduced from [61].

Half Cell Specific Capacity Values

If the half-cell (HC) specific capacity value is reported, the conversion of the cost is made to the FC cost per kWh of CAM, Δ,

$$\Delta\left[\frac{\$-\text{FC}}{kWh-\text{CAM}}\right]=\delta\left[\frac{\$-\text{CAM}}{kg-\text{CAM}}\right]\times\frac{1}{\alpha}\left[\frac{\$-\text{FC}}{\$-\text{CAM}}\right]\times\frac{1}{\beta}\left[\frac{\text{kg}-\text{CAM}}{\text{Ah}-\text{CAM}}\right]\times\frac{1}{\text{OV}}\left[\frac{1}{\text{V}}\right]\times\left[\frac{1000\text{V}}{1\text{kV}}\right] \tag{6.24}$$

where β is the 10^{th} cycle HC cathode specific capacity value.

Method 2 - Adding the Non-cathode Component Contribution to the Calculated Cathode Contribution

Alternatively, we can hold constant the \$/kWh contribution of non-cathode components and add that to the calculated \$/kWh contribution of cathode component. The batteries in the study cited are 11.5 kWh batteries[61]; as shown in Figure 6-7, the cost contribution, the cost contribution of the none-cathode components for a theoretical NIB are \$618 for a 11.5kWh battery, resulting in a specific cost of \$53.7/kWh.

$$\Delta\left[\frac{\$-\text{FC}}{kWh-\text{FC}}\right]=53.7\left[\frac{\$-\text{non-cathode}}{\text{kWh}-\text{FC}}\right]+\delta\left[\frac{\$-\text{CAM}}{kg-\text{CAM}}\right]\times\frac{1}{\beta}\left[\frac{\text{kg}-\text{CAM}}{\text{Ah}-\text{FC}}\right]\times\frac{1}{\text{OV}}\left[\frac{1}{\text{V}}\right]\times\left[\frac{1000\text{V}}{1\text{kV}}\right] \tag{6.25}$$

where δ is output CAM cost from the PBCM, β is the 10^{th} cycle FC specific capacity value, and OV is the operating cell voltage.

In the absence of FC values, HC capacities were used as a substitute when comparing across cases. Using HC capacities for both cases allows for a like-for-like comparison.

In our study, while the ideal methodology specified the use of FC capacities, we encountered instances where only HC capacities were available. In order to maintain consistency and facilitate meaningful comparisons across specific cases, we opted to use HC capacities as a substitute. This allows for a 'like-for-like' comparison. By

comparing HC capacities against HC capacities, we believe our analysis remains comparative, despite the deviation from the ideal methodology. We acknowledge this as a limitation in our approach, but deem it necessary to provide comprehensive insights into all the cases examined.

Method 2 and the specific capacity of the 10^{th} cycle will be used in all subsequent case studies cost calculations.

6.7 Sodium-iron-manganese Oxide

The cost of $Na_{2/3}[Fe_{1/2}Mn_{1/2}]O_2$ (NFMO) produced by solid-state synthesis was modeled by examining the lab-scale synthesis route (see Figure 6-8) [59][64]. NFMO was produced by combining Na_2CO_3, Fe_2O_3, and Mn_2O_3 in stoichiometric proportions. In lab-scale synthesis, the constituents were manually ground with a mortar and pestle for a duration of 2 hours to ensure a homogeneous mixture. Following this, the mixture was compacted into pellet form for more effective handling. These pellets were then calcined in an air environment at a temperature of 900°C for 12 hours. After the calcination process, the pellets were quenching using liquid nitrogen, to finalize the synthesis. The lab-scale unit operations were converted into those used at the manufacturing level (see Section 6.3).

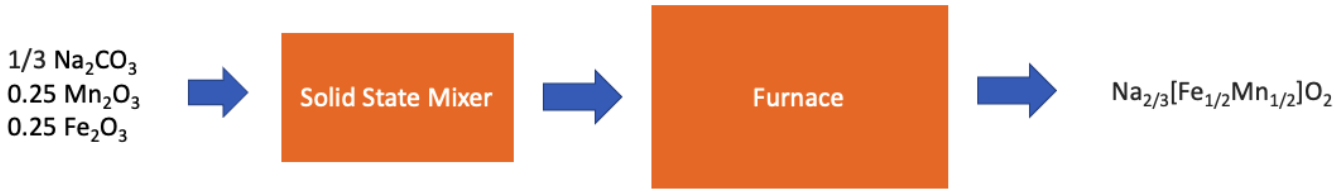

Figure 6-8: NFMO solid-state synthesis route.

As shown in Table 6.8, the cost of producing NFMO is $1.87/kg. The majority of the cost is material cost at $1.59/kg, followed by equipment and energy cost. At $1.87/kg, the solid-state synthesis process of NFMO is notably cost-effective. Solid-state synthesis processes do not require large volume throughputs since there are no liquids involved. Hence, solid-state synthesis processes require a small number of equipment and land area - this decreases the capital expenditure on the purchase, installation, and maintenance of such equipment, thereby reducing the overall production cost.

Colleagues at the Olivetti Group utilized natural language processing (NLP) tools to analyze a dataset of 10,000 academic papers, with a primary focus on extracting information related to performance and synthesis challenges and strategies pertaining to NIB CAM. Using Named Entity Recognition and Relationship Extraction (NER-RE),

	Cost ($/kg)
Material	1.59
Equipment	0.103
Building	0.006
Overhead	0.036
Maintenance	0.011
Labor	0.023
Energy	0.095
Total NFMO Cost	1.87

Table 6.8: Cost breakdown of NFMO.

we identified relevant phrases and established establish challenge-mitigation pairs and cluster. In this study, we will focus on three capacity improvement strategies: sacrificial salt addition, morphology change, and moisture sensitivity. The case studies identified for NFMO CAMs are presented in Table 6.9.

CAM	**Case**	**HC/FC**	**Anode**	**Elect**	**T**(°C)	**C-rate**	**Q**(mAh/g)	**E** (V)	**Synthesis**	**Ref.**
NFMO	Base	FC	H. Carbon	1M $NaPF_6$ EC:DEC	25	0.16C	50	1.0-4.1	Solid-state	[51]
NFMO	Base	HC	Sodium	1M $NaPF_6$ EC:DEC	25	0.13C	166	1.0-4.1	Solid-state	[51]
NFMO	+10% NaN_3	FC	H. Carbon	1M $NaPF_6$ EC:DEC	25	0.13C	78	1.0-4.2	Solid-state	[51]
NFMO	+20% NaN_3	FC	H. Carbon	1M $NaPF_6$ EC:DEC	25	0.10C	123	1.0-4.2	Solid-state	[51]
NFMO	+16% $Na_2C_4O_4$	FC	H. Carbon	1M $NaPF_6$ EC:DEC	25	0.11C	105	1.0-4.1	Solid-state	[50]
NFMO	+23% $Na_2C_4O_4$	FC	H. Carbon	1M $NaPF_6$ EC:DEC	25	0.09C	133	1.0-4.1	Solid-state	[50]
NFMO	+31% $Na_2C_4O_4$	FC	H. Carbon	1M $NaPF_6$ EC:DEC	25	0.08C	154	1.0-4.1	Solid-state	[50]
NFMO	Air-protected environment	HC	Sodium	1M $NaClO_4$ PC +2wt.% FEC	-	0.05C	172	1.5-4.3	Solid-state	[33]
NFMO'	Moisture insensitive	HC	Sodium	1M $NaClO_4$ PC +2wt.% FEC	25	-	186	1.5-4.3	Sol–gel	[42]
NMFTO	Air-protected environment	HC	Sodium	1M $NaPF_6$ EC:DEC +2wt.% FEC	-	1.0C	100	2.0-4.0	Co-precipitation	[37]
NFMO	Nanoparticles	FC	H. Carbon	1M $NaClO_4$ EC:PC	-	0.10C	75	1.0-3.8	Co-precipitation	[40]
NFMO	Nanofibers	HC	Sodium	1M $NaClO_4$ PC +2wt.% FEC	-	0.10C	171	1.5-4.2	Sol-gel +Electrospinning	[44]

Table 6.9: NFMO case studies that cause capacity improvement with respect to the base case. HC and FC stand for half-cell and full-cell. Capacity is taken at the 10^{th} cycle. NFMO' represents $Na_{0.59}Mn_{0.87}Fe_{0.13}O_2$. NMFTO represents $Na_{2/3}Mn_{0.8}Fe_{0.1}Ti_{0.1}O_2$. H. Carbon represents hard carbon. Elect represents electrolyte. T represents temperature. Q represents capacity. E represents cell potential.

The C-rate of a battery is a measure that describes the rate at which a battery is discharged relative to its nominal (maximum) capacity. It is an important parameter that provides insights into the battery's performance and longevity. In Table 6.9, in the cited references where the C-rate was not explicitly stated, it was calculated based on the following formula.

$$C - \text{rate} = \frac{\text{current (mA/g)}}{\text{nominal capacity (mAh/g)}} \tag{6.26}$$

Note that the nominal capacity is typically the capacity at the first cycle.

6.7.1 Sacrificial Salt Addition

The introduction of sacrificial salts can lead to improvements in specific capacity and a reduction in irreversible capacity loss, enhancing the overall performance of the battery. The purpose of a sacrificial salt is to release ions that can supplement the ions in the CAM. This process helps maintain the stability and performance of the battery. This can help to compensate for sodium ion loss during NIB operation, such as SEI formation, which can lead to a loss of capacity.

Sodium Azide

The negative electrode in the full cell configuration of an NFMO NIB exhibits an irreversible capacity that can be compensated for using a such as sodium azide (NaN_3) sacrificial salt. This addition leads to a significant improvement in the reversible capacity, resulting in an increase of up to 60% when 10% NaN_3 is added to the CAM[51]. A further improvement in the reversible capacity occurs when 20% NaN_3 is added (see Figure 6-9).

When NaN_3 additive is added, the CAM cost increase is due to material cost, however the overall \$/kWh value ultimately decreases given the capacity gained by adding NaN_3. As mentioned, the cell cost values are calculated using the 10^{th} cycle specific capacity and are presented in Table 6.10. A waterfall plot analysis is presented in Figure 6-10.

CAM	**Capacity** (mAh/g)	**CAM** (\$/kg)	**CAM** (\$/kWh)	**Cell** (\$/kWh)
NFMO	50	1.87	14.9	68.7
NFMO + 10 wt% NaN_3	78	1.98	10.2	63.9
NFMO + 20 wt% NaN_3	123	2.10	6.8	60.5

Table 6.10: NFMO-based NIB cost with and without NaN_3 addition.

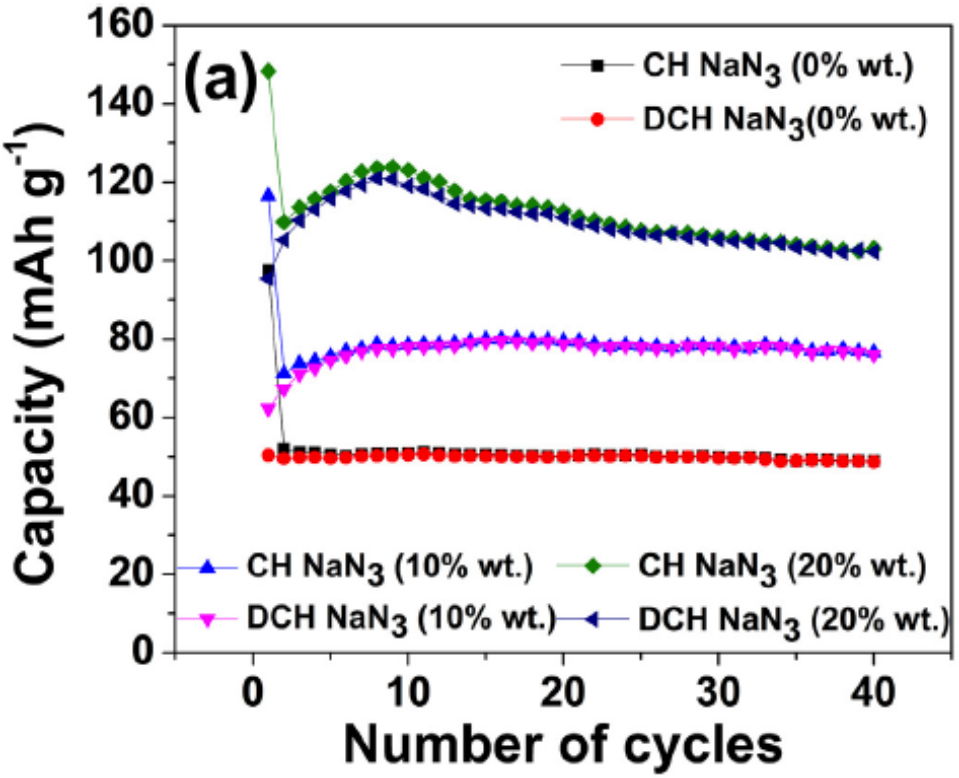

Figure 6-9: NFMO full cell cycling performance with 0%, 10%, and 20% NaN_3 addition. Reproduced from [51].

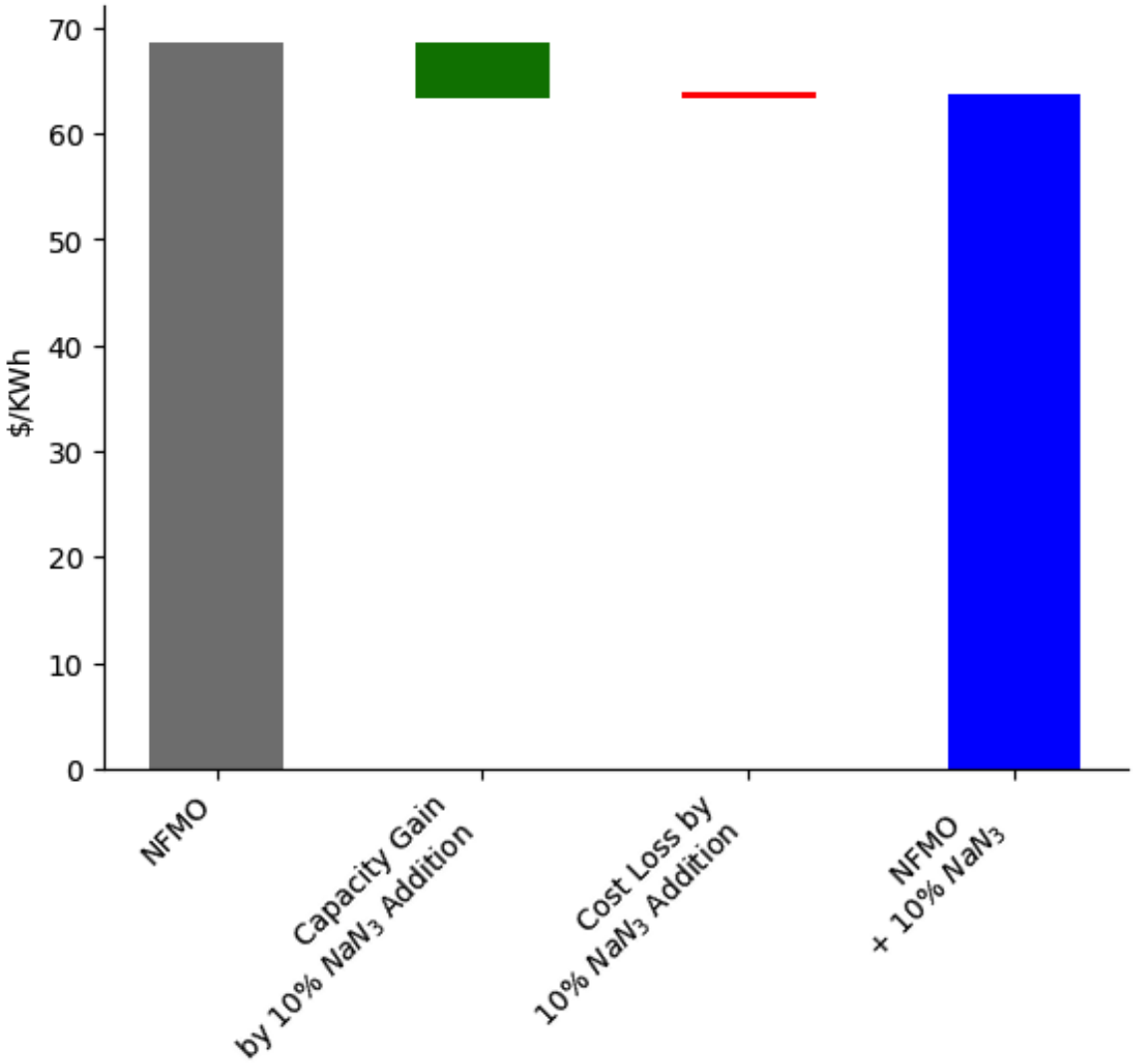

Figure 6-10: Effects of NaN_3 sacrificial salt addition on NFMO through waterfall plot analysis.

Sodium Squarate

Sodium squarate ($Na_2C_4O_4$) is another sacrifical salt that enhances the capacity performance of NFMO-based NIBs[50]. The cycling stability and electrochemical performance of NFMO with 23% and 31% $Na_2C_4O_4$ sacrificial salts outperforms the cathode with NaN_3 sacrificial salt. The full cell cycling performance plots are presented in Figure 6-11. Unlike NaN_3, $Na_2C_4O_4$ is not typically bought from suppliers so we were able to calculate its cost using our PBCM. $Na_2C_4O_4$ is synthesized using 3, 4-dihydroxy-3- cyclobutene-1, 2-dione (squaric acid) and Na_2CO_3 as starting materials. A 1:1 mass ratio mixture is dissolved in deionized water followed by overnight stirring. The resulting powder needs to be dried under vacuum to obtain $Na_2C_4O_4$ powder. Squaric acid is an expensive liquid that costs \$30/kg [18], and results in $Na_2C_4O_4$ costing \$32.8/kg.

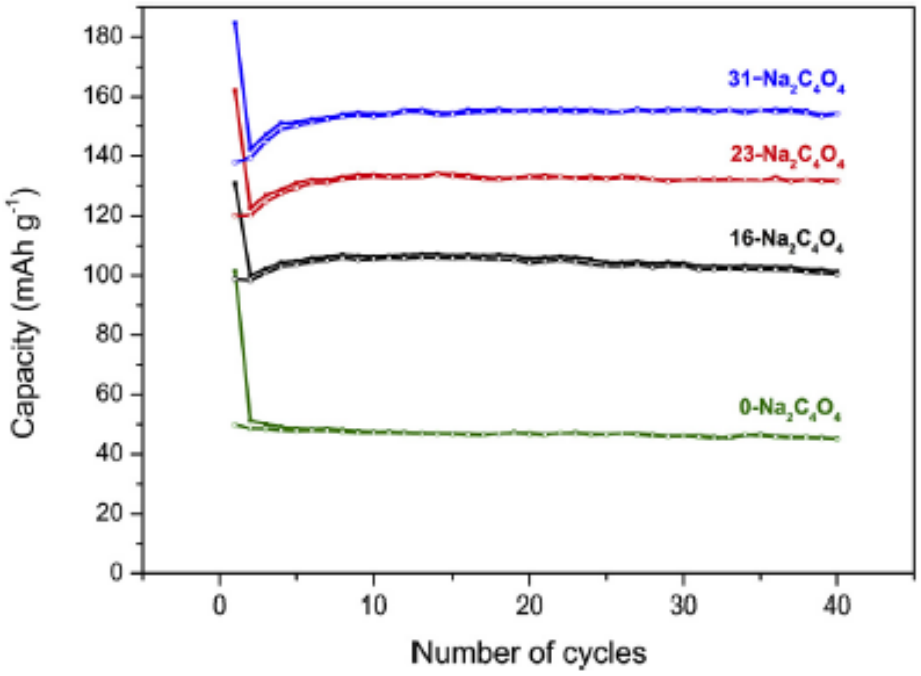

Figure 6-11: NFMO full cell cycling performance with 0%, 16%, 23%, and 31% $Na_2C_4O_4$. Reproduced from [50].

When $Na_2C_4O_4$ additive is added, the CAM cost increase is due to material cost, and the overall cell cost per unit energy (\$/kWh) also increases since the cost increase

by adding $Na_2C_4O_4$ is not compensated by the capacity gained by adding $Na_2C_4O_4$. The NFMO-based NIB cost with and without $Na_2C_4O_4$ addition are presented in Table 6.11. A waterfall plot analysis for the case with NFMO and 23% $Na_2C_4O_4$ addition is presented in Figure 6-12.

CAM	**Capacity** (mAh/g)	**CAM** ($/kg)	**CAM** ($/kWh)	**Cell** ($/kWh)
NFMO	50	1.87	14.9	68.7
NFMO +16% $Na_2C_4O_4$	105	6.8	25.9	79.6
NFMO +23% $Na_2C_4O_4$	133	8.9	26.8	80.5
NFMO +31% $Na_2C_4O_4$	154	11.5	30.1	83.7

Table 6.11: NFMO-based NIB cost with and without $Na_2C_4O_4$ addition.

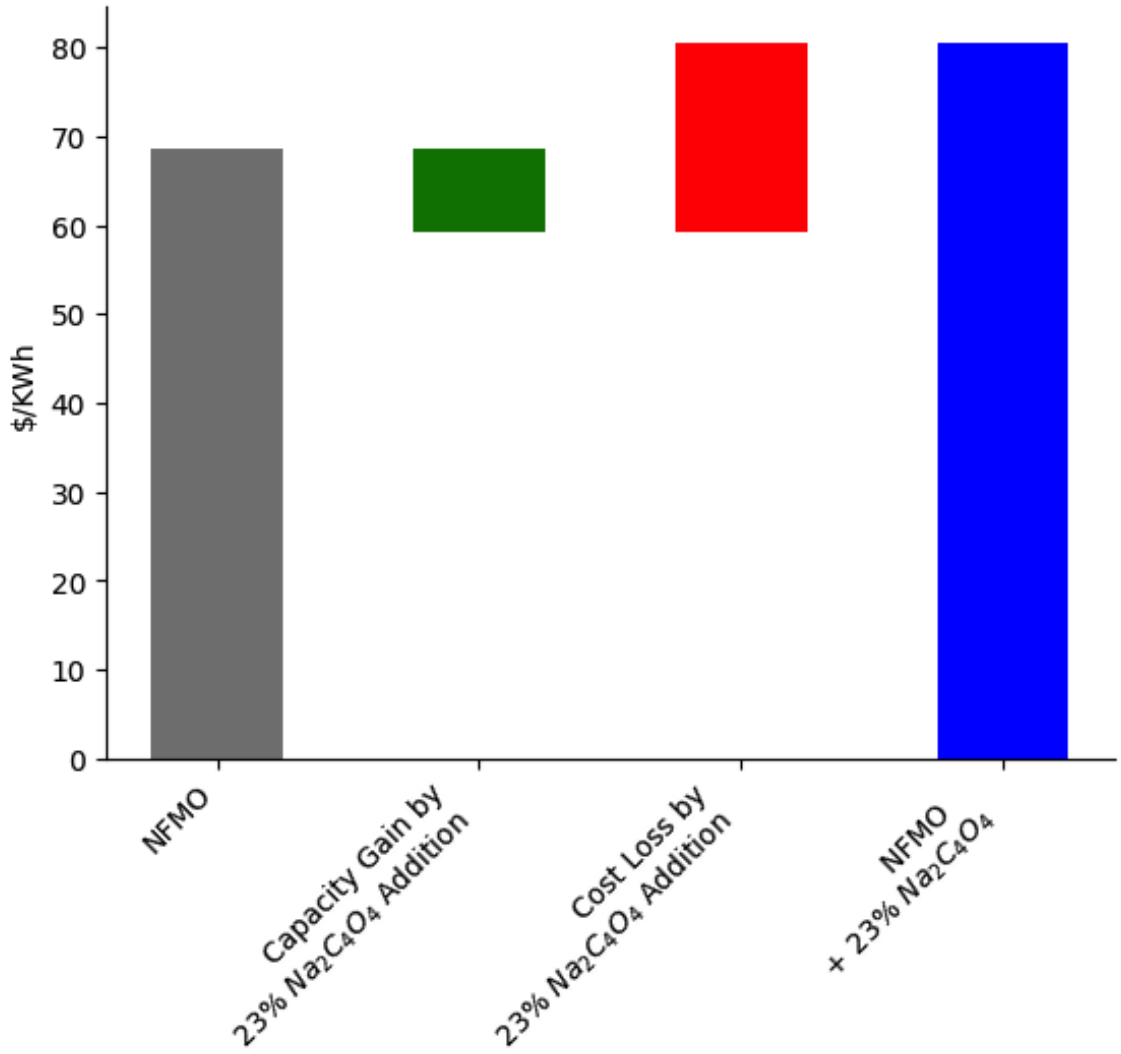

Figure 6-12: Effects of $Na_2C_4O_4$ sacrificial salt addition on NFMO through waterfall plot analysis.

6.7.2 Moisture Sensitivity

Air-protected vs Air-exposed NFMOs

In a study of solid-state synthesized P2-NFMO and its exposure to CO_2 and moisture, two distinct sample types, "air-exposed" and "air-protected," were studied[33]. Air-exposed samples were calcined in a furnace at ambient air. Air-protected samples were carefully obtained by heat treatment in a protective argon atmosphere, and subsequently transferred to an argon-filled glovebox.

It was determined that the two CAM samples exhibited different electrochemical behavior, with a higher charge-discharge polarization in air-exposed NFMO compared to the more rigorously air-protected NFMO. However, there was no significant improvement in cycling performance. The study only included cycling performance (discharge capacity) data on the air-protected NFMO NIBs, which were half-cells (HC)[33]. Air-exposed NFMO NIB HC data was obtained from the base case study[51]. The HC capacity at the 10^{th} cycle is not significantly different across the two samples. The cost model for the air-protected NFMO sample underwent specific modifications when compared to the air-exposed case. These changes include the incorporation of a dryroom environment within the furnace and the replacement of air with argon gas inside the furnace. These adjustments were implemented to modify the conditions under which the NFMO sample is processed. As shown in Table 6.12, air-protected NFMO NIBs are more expensive than the air-exposed NFMO.

CAM	**Capacity (HC)** (mAh/g)	**CAM** ($/kg)	**CAM** ($/kWh)	**Cell** ($/kWh)
Air-exposed (base case) NFMO	166	1.87	4.50	58.2
Air-protected NFMO	172	7.87	18.3	72.0

Table 6.12: NFMO moisture sensitivity case using air-protected environment. The air-protected NFMO sample was processed with special care to control moisture: it was calcined in argon gas within the furnace and subsequently stored in a dryroom. Note that the capacities are HC capacities, and therefore, cell cost per unit energy are based off that.

Moisture Insensitive $Na_{0.59}Mn_{0.87}Fe_{0.13}O_2$

Mn-rich layered oxides have demonstrated exceptional electrochemical stability even when exposed to moisture for prolonged durations (also see Section 6.7.3). $Na_{0.59}Mn_{0.87}Fe_{0.13}O_2$ was identified to be a moisture insensitive chemistry[42]. This increase in insensitivity to moisture is attributed to an increase in the Mn concentration of the oxide[42]. $Na_{0.59}Mn_{0.87}Fe_{0.13}O_2$ was synthesized by a sol–gel method using stoichiometric ratios of $NaNO_3$, $Fe(NO_3)_3$, and $Mn(NO_3)_2$, and a 2M citric acid solution as a chelating agent in a 1:1 molar ratio to the total metal cations[42]. The synthesis of moisture-resistant $Na_{0.59}Mn_{0.87}Fe_{0.13}O_2$ is still more expensive than producing air-exposed NFMO; however, adopting a moisture-resistant chemistry like $Na_{0.59}Mn_{0.87}Fe_{0.13}O_2$, which costs \$61.8/kWh, is cheaper than adopting an air-controlled synthesis route, which costs \$72.0/kg, because of the associated downstream cell production costs (see Table 6.13 and Table 6.12). A waterfall plot analysis for adopting $Na_{0.59}Mn_{0.87}Fe_{0.13}O_2$ is presented in Figure 6-13.

CAM	**Capacity (HC)** (mAh/g)	**CAM** (\$/kg)	**CAM** (\$/kWh)	**Cell** (\$/kWh)
Air-exposed (base case) NFMO	166	1.87	4.50	58.2
$Na_{0.59}Mn_{0.87}Fe_{0.13}O_2$	186	3.77	8.10	61.8

Table 6.13: Moisture insensitive $Na_{0.59}Mn_{0.87}Fe_{0.13}O_2$ case.

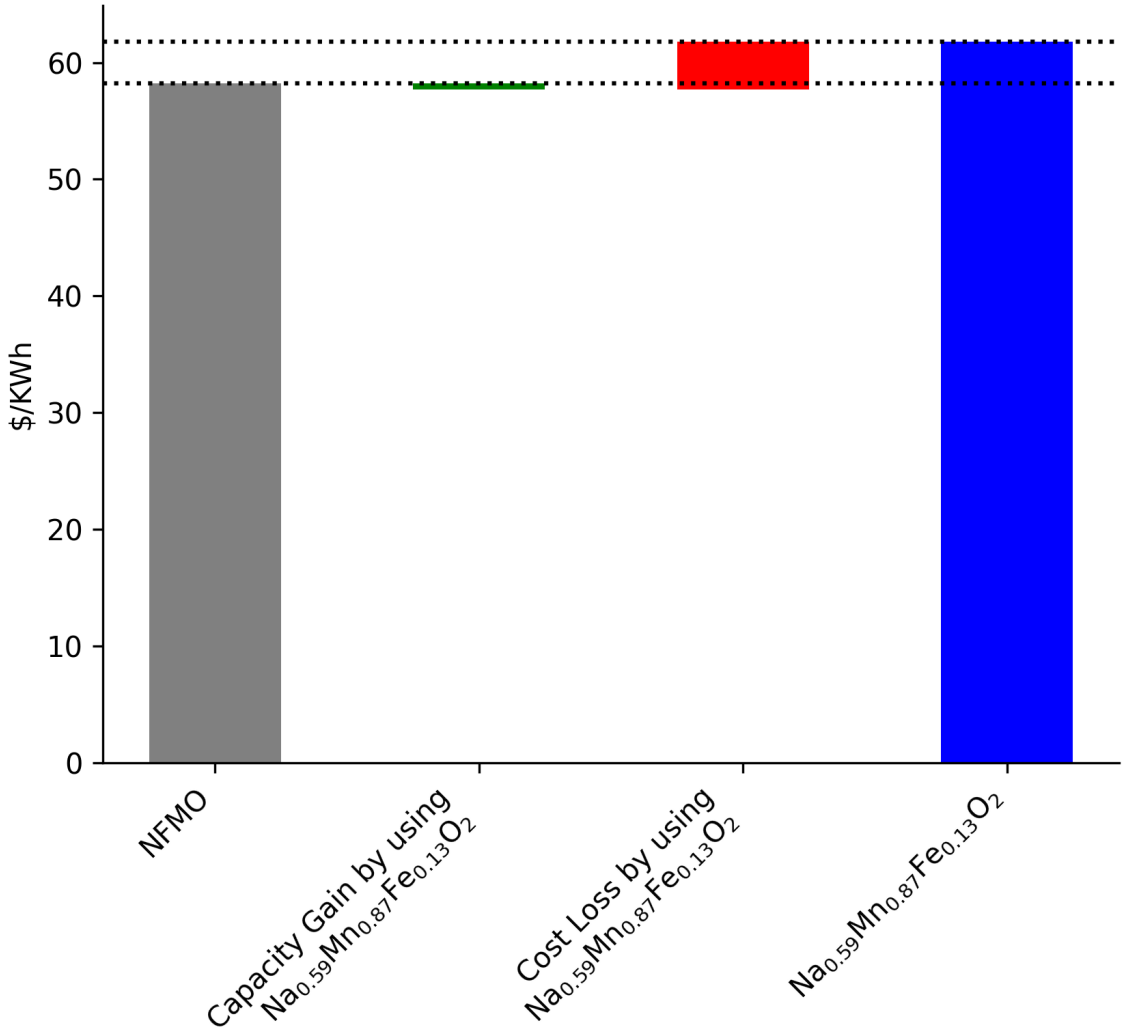

Figure 6-13: Effects of adopting moisture-insensitive $Na_{0.59}Mn_{0.87}Fe_{0.13}O_2$ chemistry demonstrated through a waterfall plot analysis.

6.7.3 Sodium-manganese-iron-titanium Oxide

Research on P2-$Na_{2/3}Mn_{0.8}Fe_{0.1}Ti_{0.1}O_2$ (NMFTO) CAM showcased the difference of using pristine dried electrodes and hydrated electrodes on cell capacity of NIBs[37]. Stoichiometric quantities of Na_2CO_3, Mn_2O_3, Fe_2O_3, and TiO_2 powders were used to synthesize the $Na_{2/3}Mn_{0.8}Fe_{0.1}Ti_{0.1}O_2$ CAM, as shown in Table 6.14. The hydrated phase was prepared by exposing the pristine powder to de-ionized water for 24 hours, followed by drying at 50°C. The protonated phase, which is not discussed in the analysis we present, was prepared by drying the hydrated phase in a vacuum oven at 200°C for 24 hours. The capacity plots of NMFTO-based NIBs that are pristine and hydrated are presented in Figure 6-14.

Identity	**Status**	**Solid-state mix**	**Liquid-state mix**	**Filter Press**	**Cake Dry**	**Calcine**
Na_2CO_3	Precursor	0.33	0.33	0.33	0.33	0
Mn_2O_3	Precursor	0.4	0.4	0.4	0.4	0
Fe_2O_3	Precursor	0.05	0.05	0.05	0.05	0
TiO_2	Precursor	0.1	0.1	0.1	0.1	0
H_2O	Precursor	8	8	8	0	0
$Na_{0.67}Mn_{0.8}Fe_{0.1}Ti_{0.1}O_2$	Product					

Table 6.14: $Na_{2/3}Mn_{0.8}Fe_{0.1}Ti_{0.1}O_2$ synthesis route.

The hydrated NMFTO case was modeled as a synthesis case with no moisture control. In the CAM manufacturing processes, a dry room environment is typically only introduced to the final heating step , as it would not be necessary to introduce a dryroom in precursor solid-state mixing or liquid-state reactors. As mentioned in Section 6.4.2, the dry room operations cost was estimated to be \$1270/m^3 [22]. A 30% equipment headspace was taken into account. The pristine NMFTO case was modeled with the presence of a dryroom. This increased the cost from \$3.30/kg to \$3.85/kg. To account for the dryroom cost downstream of the CAM production step, the plant area of all the steps in the BatPaC process, leading up to the cell assembly in the dry room step, were accounted for (Table 6.1). The annual production capacity used in

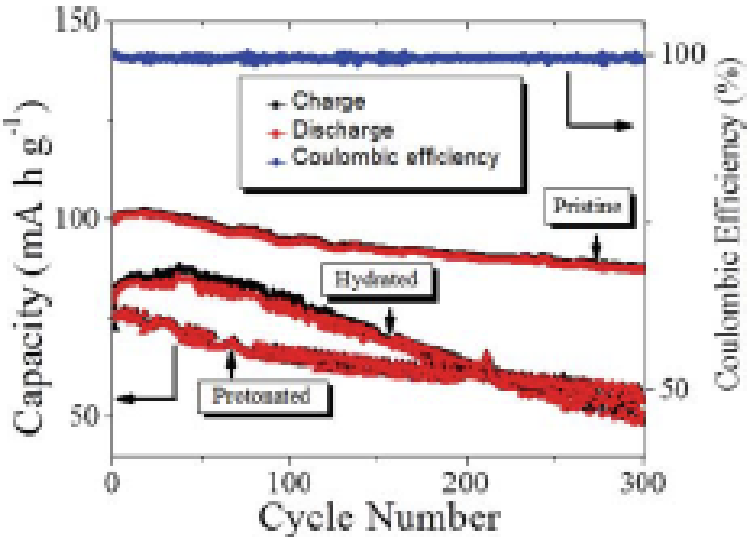

Figure 6-14: Capacity plots of NMFTO-based NIBs that are pristine and hydrated. Reproduced from [37].

our model was 6,500 tonnes-CAM/yr, were as the throughput in the BatPac basecase model was 72,500 tonnes-CAM/yr, therefore, our plant area was adjusted accordingly. The costs of the hydrated (no moisture control) and pristine (with moisture control) NMFTO-based batteries are presented in Table 6.15. A hydrated NMFTO-cathode NIB costs \$69.4/kg while a pristine NMFTO-cathode NIB costs \$68.1/kg, indicating a slight cost-effectiveness improvement. A waterfall plot analysis is presented in Figure 6-15.

CAM	**Capacity** (mAh/g)	**CAM** (\$/kg)	**CAM** (\$/kWh)	**Cell** (\$/kWh)
$Na_{0.67}Mn_{0.8}Fe_{0.1}Ti_{0.1}O_2$	84	3.30	15.7	69.4
$Na_{0.67}Mn_{0.8}Fe_{0.1}Ti_{0.1}O_2$ in dryroom	100	3.58	14.4	68.1
$Na_{0.67}Mn_{0.8}Fe_{0.1}Ti_{0.1}O_2$ in dryroom + downstream	100	18.5	74.4	128.1

Table 6.15: Moisture sensitivity case.

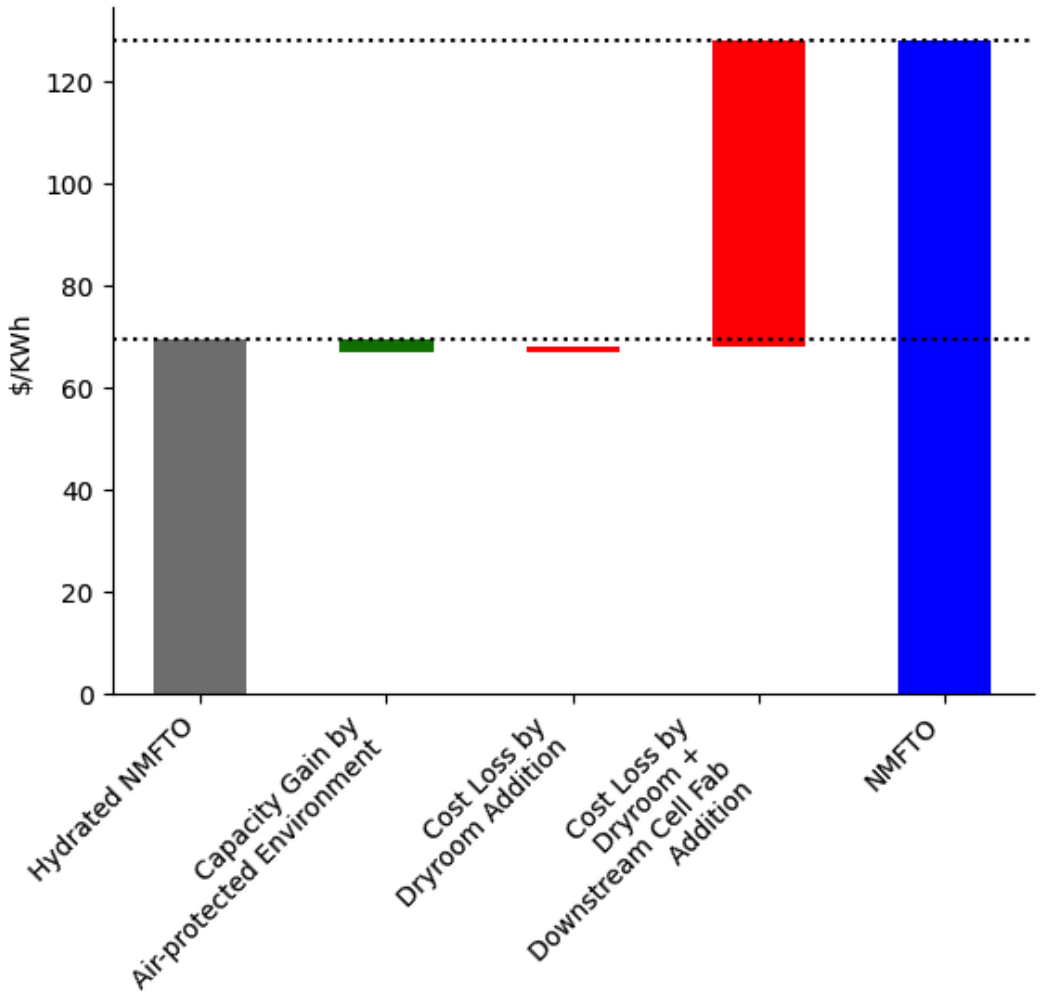

Figure 6-15: Effects of moisture control on NMFTO through waterfall plot analysis.

6.7.4 Morphology Change

Nanoparticles

Nanoparticles (NPs) can be synthesized using co-precipitation-based synthesis, which offers an advantage over solid-state synthesis because of the ability to control the particle size. The synthesis of P2-$Na_{2/3}[Fe_{1/2}Mn_{1/2}]O_2$ NPs is carried out by co-precipitation method at 25°C, as outlined by Han et al.[40]. A stoichiometric mixture of $Fe(NO_3)_3$ and $Mn(NO_3)_2$ are prepared in distilled water under a vigorous stirring. In a separate reactor, an aqueous solution of NaOH is prepared. The two solutions were mixed together in a drip-wise fashion and stirred for 6 hours. The precipitates are then filtered and dried. The dried precipitates are mixed with stoichiometric amount of $NaNO_3$. The resulting solid powder is then annealed at 900°C under a normal atmospheric condition.

	Cost ($/kg)
Material	0.23
Equipment	1.17
Building	0.02
Overhead	0.07
Maintenance	0.013
Labor	0.18
Energy	0.012
Total NFMO Cost	1.70

Table 6.16: Cost breakdown of NFMO NPs synthesized by co-precipitation.

The cost breakdown of NFMO NPs synthesized by co-precipitation is shown in Table 6.16. NFMO NPs cost $1.70/kg, which is cheaper than NFMO synthesized by solid-state synthesis that costs $1.87/kg. While more pieces of equipment are required when manufacturing using a co-precipitation method, the cost of the CAM is lower because co-precipitation synthesis involves nitrate-based precursors which are three to five times less expensive than oxide-based precursors used in solid-state synthesis. The capacity increase attributed to the morphology change to NPs further

enhances the cost-effectiveness of this approach: the overall cell cost of NFMO NPs is \$62.8/kWh, which is less than that of the NFMO base case (\$68.7/kWh). A waterfall plot analysis outlining the impact of NP morphology control is outlined in Figure 6-16.

CAM	**Capacity** (mAh/g)	**CAM** (\$/kg)	**CAM** (\$/kWh)	**Cell** (\$/kWh)
NFMO	50	1.87	14.9	68.7
NFMO Nanoparticles	75	1.70	9.1	62.8

Table 6.17: NFMO-based NIB cost with and without NP size control.

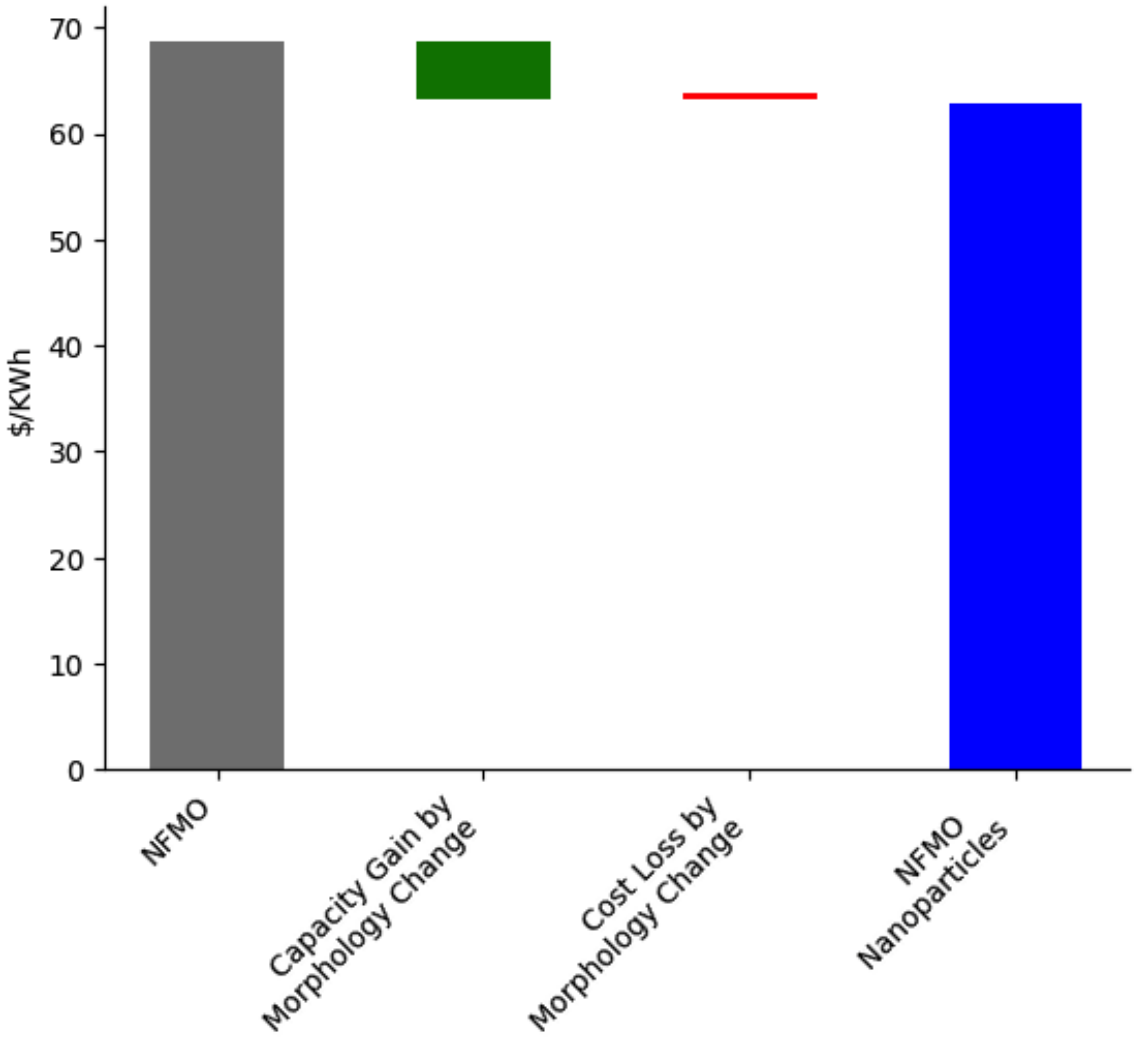

Figure 6-16: Effects of morphology change to nanoparticles on NFMO through waterfall plot analysis.

Nanofibers

NFMO nanofibers (NFs) are synthesized by a sol-gel process with an electrospinning unit added to it, as outlined by Kalluri et al.[44]. The precursor solution is prepared by dissolving stoichiometric quantities of sodium acetate, iron nitrate, and manganese acetate in a blended solvent comprising ethanol and N,N-dimethylformamide (DMF), followed by the addition of 10 wt.% polyvinylpyrrolidone (PVP). After stirring, electrospinning is carried out (through an electrospinning unit). Following the completion of electrospinning, the newly-spun nanofibrous mats are gathered and subjected to multi-step calcination. As mentioned in Section 6.3.6, the electrospinning process has a low flowrate that is limited by the physical properties of the precursor solution passing through the needles of the electrospinning unit (see Table 6.2 for flowrate comparison across equipment). Given the low flowrate capacity through electrospinning units, the overall cost of NFMO NFs is over $3,000/kg because many electrospinning units would be required to achieve the required annual production capacity of the CAM. Even if the flowrate of the electrospinning unit is increased by 100 (from 0.1L/h to 10L/h), the CAM would remain very expensive at $66.kg. Table 6.18 outlines the costs of NFMO NFs-based NIBs at different electrospinning flowrates, including hypothetical flowrates. In Figures 6-17, 6-18, and 6-19, we present a waterfall plot analysis for the NF case as well as the two hypothetical scenarios.

CAM	**Capacity** (mAh/g)	**CAM** ($/kg)	**CAM** ($/kWh)	**Cell** ($/kWh)
NFMO	50	1.87	14.9	68.7
NFMO NF (0.1L/h)	171	3038	7106	7160
NFMO NF (1L/h) (hypothetical)	171	336	790	844
NFMO NF (10L/h) (hypothetical)	171	66	155	209

Table 6.18: NFMO NFs batteries costs.

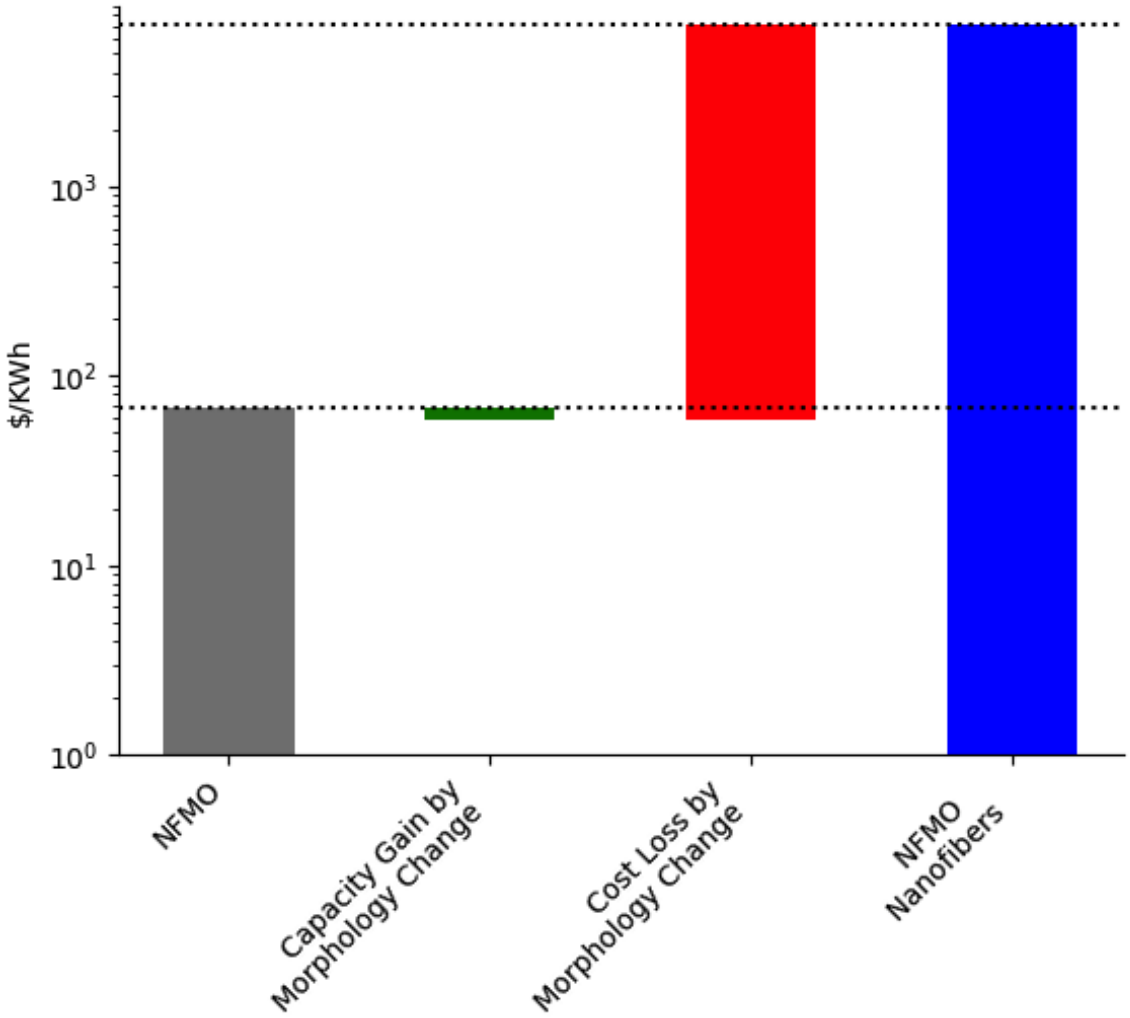

Figure 6-17: Effects of morphology change to nanofibers on NFMO through waterfall plot analysis.

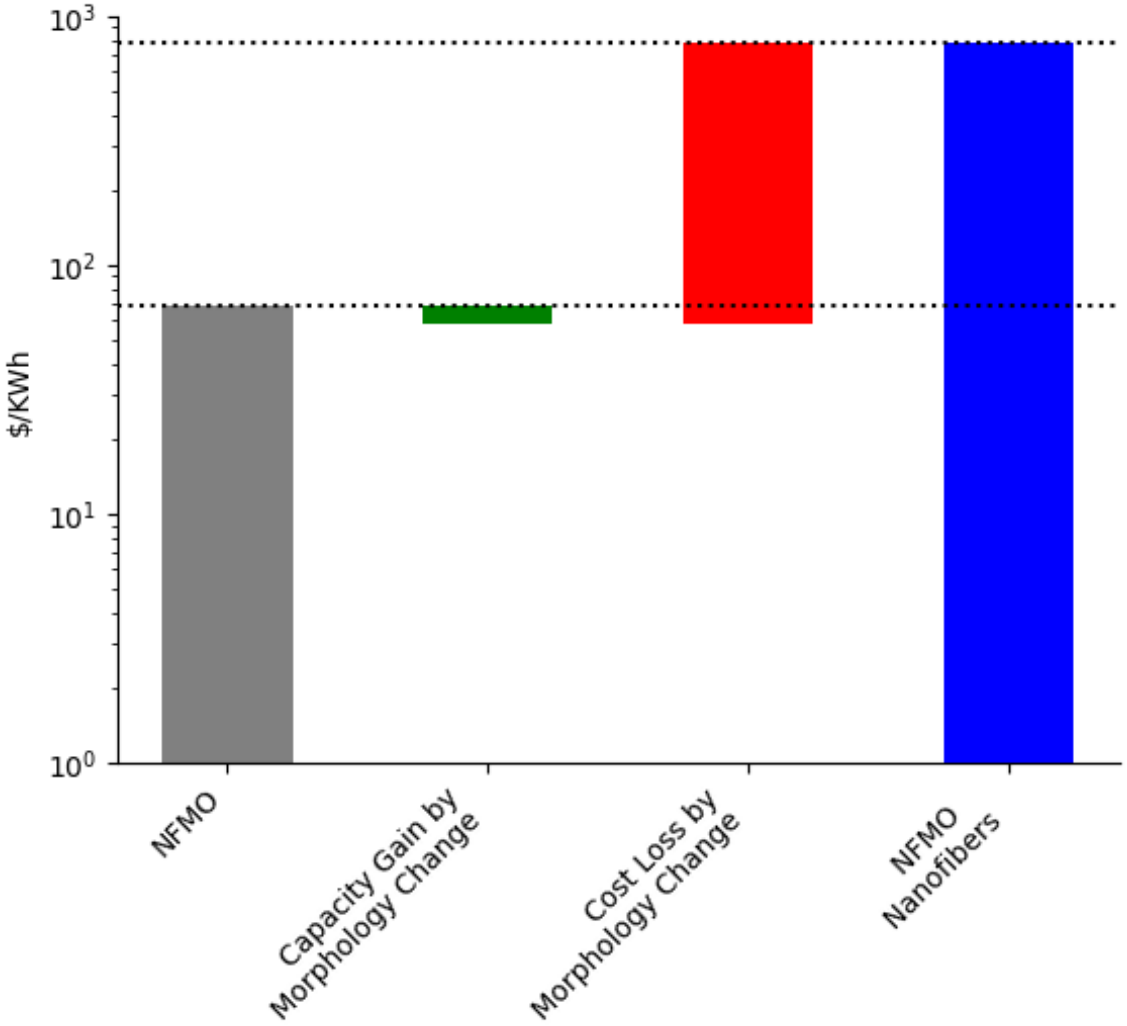

Figure 6-18: Effects of morphology change to nanofibers, with 1L/h hypothetical electrospinning unit throughput, on NFMO through waterfall plot analysis.

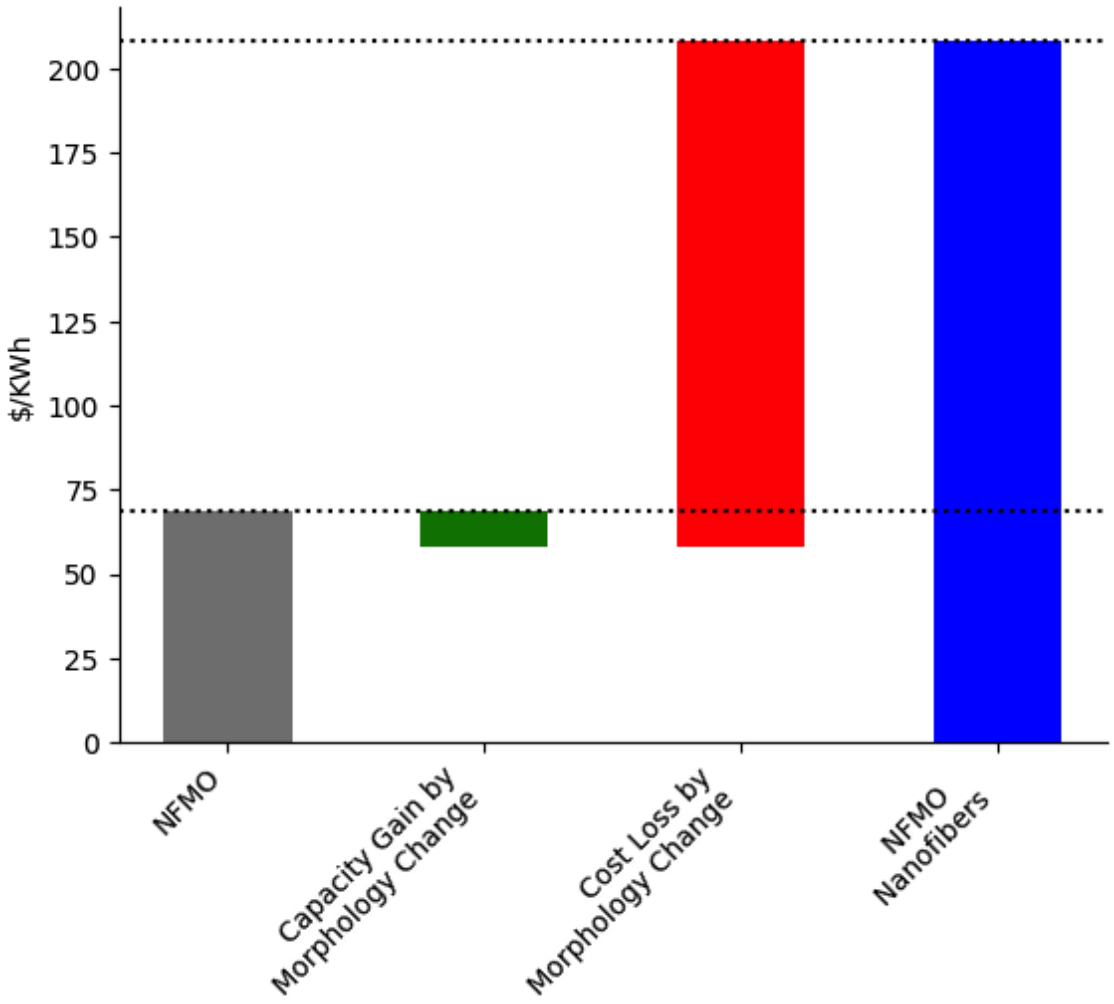

Figure 6-19: Effects of morphology change to nanofibers, with 10L/h hypothetical electrospinning unit throughput, on NFMO through waterfall plot analysis.

6.8 Summary and Discussion

We employed a PBCM, developed by combining quantitative analysis with qualitative insights gathered from expert interviews. The cost model incorporated several key factors, including raw material costs, equipment manufacturing processes costs, energy consumption, labor expenses, and maintenance requirements. To provide a measure that relates the material cost to the actual energy output of the CAM, once cost per unit mass of CAMs was determined, it was converted to cost per unit energy by incorporating the specific capacity of the CAM and the cell operating voltage. We were able to determine what cycling capacity improvement strategies were cost-effective and which ones were not. We determined that the most cost-effective cycling capacity improvement strategy was adopting NFMO with 20 wt% NaN_3 sacrificial salt, which costs \$60.5/kWh compared to the base case of \$68.7/kWh of an NFMO-based NIB. Morphology change from solid-state synthesized NFMO to NPs both decreased the cost per unit mass of CAM (as it was cheaper to synthesize NPs) and the cost per unit energy of the cell. Both adopting a moisture-insensitive NFMO-based chemistry and synthesizing the CAM in an air-protected environment increased the overall cell cost per unit energy; implying that the NFMO structure is able to perform well even when not handled in an inert environment.

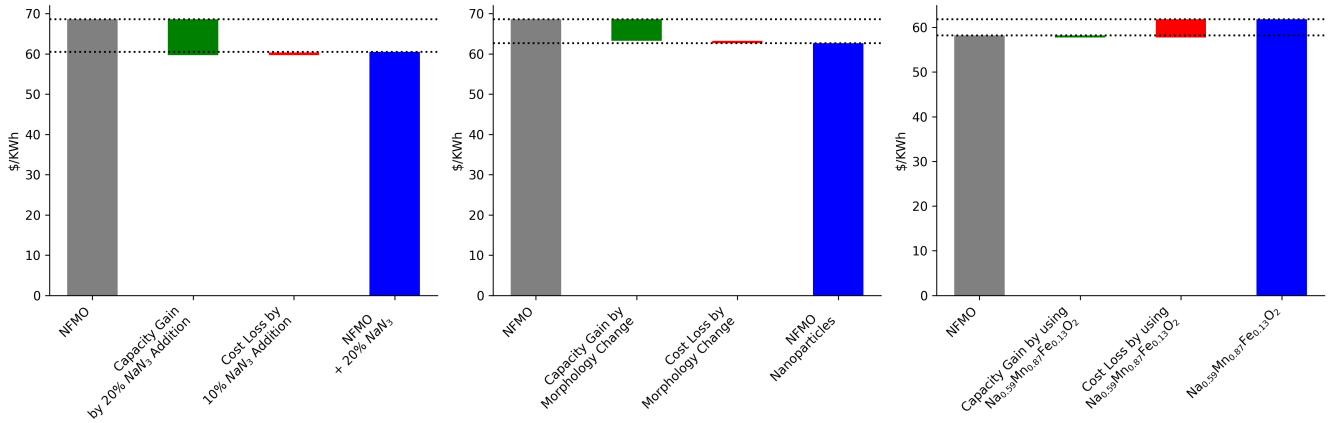

Figure 6-20: Waterfall plots of different cycling capacity improvement strategies.

A limitation of our work is that we used the 10^{th} cycle capacity of the NIBs since the NIBs are not yet commercial, in contrast to LIBs, which are well-established and evaluated based on their actual cycle capacity that includes considerations for long-term performance and efficiency. The disparity between how the capacities are measured for NIBs and LIBs creates a challenge in making direct and fair comparisons. While using the 10^{th} cycle capacity serves as a practical way to evaluate and compare the cost performance of different NIB CAMs, it does not allow for a cost comparison with LIBs. Since LIBs are mature and have undergone various iterations of optimization, comparing them to the nascent NIBs can inherently introduce biases. The potential for improvements in NIBs might be underrepresented.

As mentioned earlier, the fluctuation in chemical prices has been significant in the past three years, especially for lithium-, cobalt-, and nickel- based chemicals (see Figure 6-1). Other chemical markets have inevitably been affected, but to a lesser extent. While this is another limitation, we can argue that the costs of sodium, iron, and manganese have not increased as drastically so that does not significantly impact the findings of our study.

The calculation of the NIB non-cathode component cost per unit energy ($/kWh) contribution relies on numbers derived from the BatPac model, which is originally designed to model the costs of LIBs. In applying this model to NIBs, only the raw material costs and the anode half-cell capacity are adjusted, while other factors are left unaltered. This approach inherently assumes that the manufacturing processes for both LIBs and NIBs are identical and does not accommodate potential differences in chemical handling methods between the two types of batteries. As such, it may not fully capture the unique cost dynamics associated with NIBs, overlooking key distinctions in materials, processing techniques, and production requirements. Moreover, the method of taking the NIB non-cathode component cost per unit energy ($/kWh) contribution to be fixed assumes that different types of electrolytes which are used in different NIBs will cost the same, which is a reasonable assumption given how small the electrolyte cost is compared to other components. Our future work

will include the costs, types, and performance implications of different non-cathode components.

The category of "NIBs" encompasses a wide variety of specific chemistries, designs, and applications. In our study, we focused on LMOs. Treating them as a monolithic group may oversimplify the nuances and variability with the potential of NIBs. Prussian blue analogs (PBAs) have garnered significant attention in the field of energy storage due to their unique crystal structures and versatile electrochemical properties. These features have made PBAs promising candidates for various applications, including NIB supercapacitors. Given the unique characteristics and potential applications of NIB PBAs, conducting focused studies on their capabilities, challenges, and economic viability is imperative. This will allow for a comprehensive understanding of their role within the broader NIB landscape and highlight any distinctive advantages or constraints they might bring. As the energy storage sector continues to evolve and diversify, such in-depth explorations of specific chemistries and structures will be paramount in guiding future research, development, and commercialization efforts.

While gathering qualitative insights from experts is valuable, it's also subjective. We want to delve deeper into the differences in manufacturing processes, chemical handling methods, and production requirements between NIBs and LIBs to understand and incorporate those into future economic analyses. Developing a standardized set of evaluation metrics that can more fairly compare NIBs and LIBs, especially as NIBs mature as a technology, is important. Factors like cost, energy density, power density, cycle life, and safety should be considered in a holistic manner. Through modeling work, policy makers can develop guidelines and frameworks to promote the research, development, and deployment of the most suitable (efficient) battery technology for a given application. Policymakers can preemptively address potential challenges and harness upcoming opportunities in the realm of energy storage. Modeling serves as a foresight tool,preventing technology lock-in and enabling a proactive rather than a reactive approach to policy formation.

Appendix

	Cost ($/kg)
Material	1.56
Equipment	1.39
Building	0.03
Overhead	0.17
Maintenance	0.16
Labor	0.44
Energy	0.02
Total $Na_{0.59}Mn_{0.87}Fe_{0.13}O_2$ Cost	3.77

Table A.1: Cost breakdown of $Na_{0.59}Mn_{0.87}Fe_{0.13}O_2$.

	Cost ($/kg)
Material	1.83
Equipment	1.04
Building	0.03
Overhead	0.08
Maintenance	0.12
Labor	0.19
Energy	0.01
Total $Na_{0.67}Mn_{0.8}Fe_{0.1}Ti_{0.1}O_2$ Cost	3.77

Table A.2: Cost breakdown of $Na_{0.67}Mn_{0.8}Fe_{0.1}Ti_{0.1}O_2$.

	Cost ($/kg)
Material	28
Equipment	1328
Building	14
Overhead	606
Maintenance	142
Labor	503
Energy	417
Total NFMO NF Cost	3038

Table A.3: Cost breakdown of NFMO nanofibers.

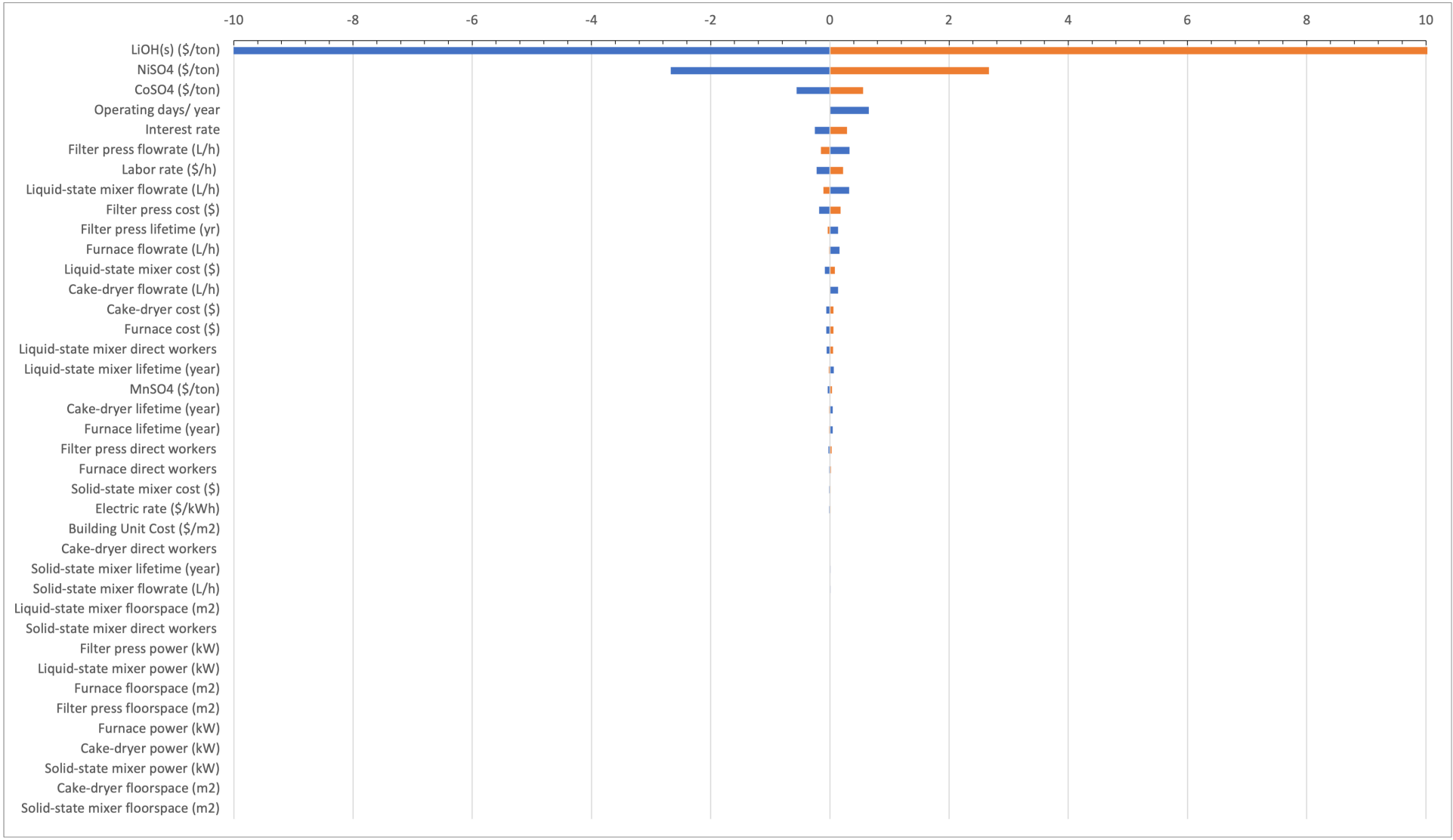

Figure A.1: Tornado plot showing the sensitivity analysis of different parameters affecting the normalized cost of the NMC cathode based on the PBCM.

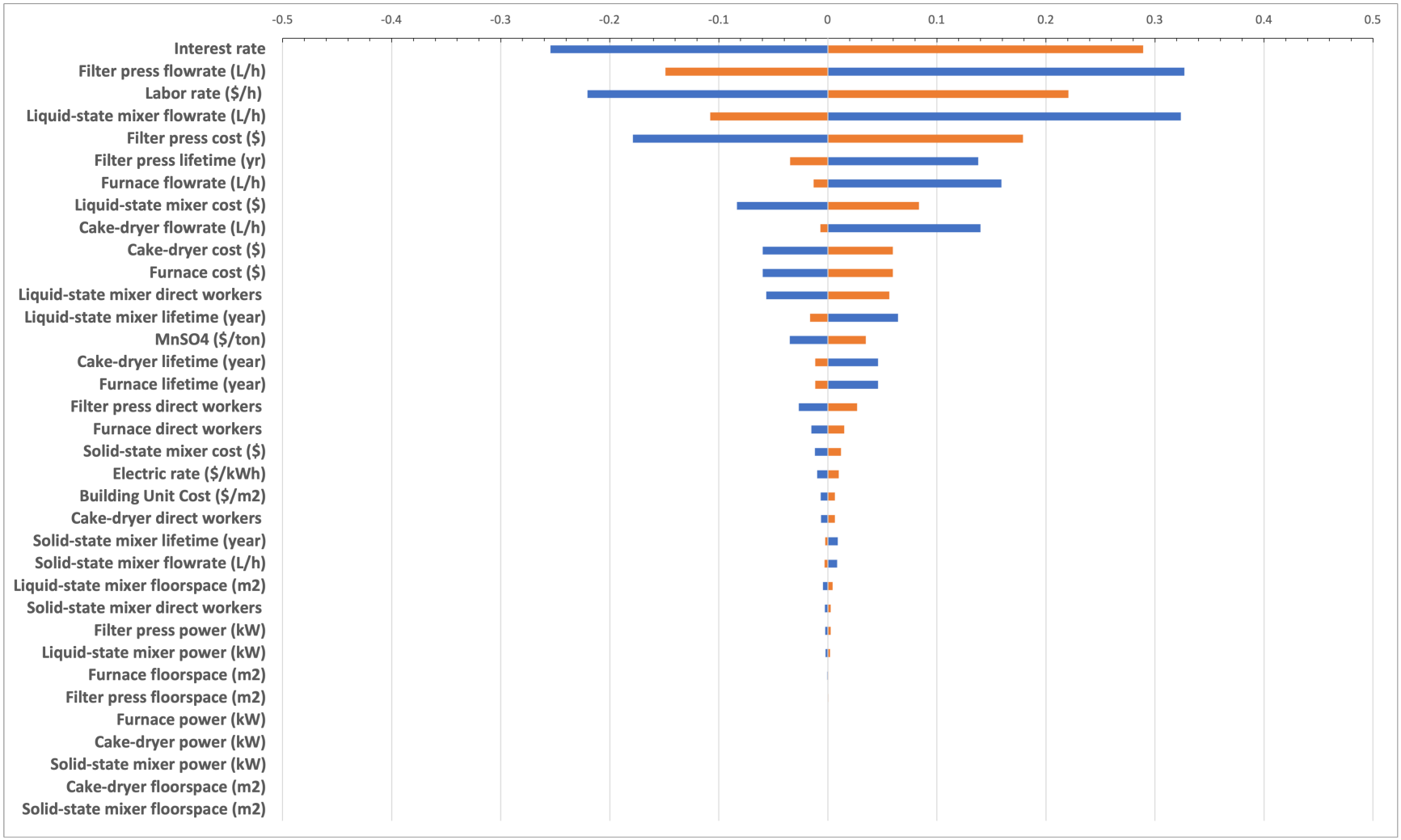

Figure A.2: Tornado plot illustrating the sensitivity analysis of various parameters, excluding chemical costs, on the normalized cost of the NMC cathode based on the PBCM.

Bibliography

[1] Accelerating Rate Calorimeter (ARC) | NETZSCH Analyzing & Testing.

[2] Battery Nail Penetration Test | ESPEC CORP.

[3] Chart: Lithium prices are through the roof this year | Canary Media.

[4] Cobalt Statistics and Information | United States Geological Survey.

[5] Graphite Statistics and Information | United States Geological Survey.

[6] How much CO2 is emitted by manufacturing batteries? | MIT Climate Portal.

[7] Lithium Battery Incidents | Federal Aviation Administration.

[8] Lithium costs up in 2021, continuing to surge in 2022 | S&P Global Market Intelligence.

[9] Lithium-ion Battery Market Size to Hit US$ 278.27 Bn by 2030 | Precedence Research.

[10] Lithium prices bounce after big plunge, but surpluses loom | Reuters.

[11] Lithium Statistics and Information | United States Geological Survey.

[12] Profitability of lithium battery energy storage products | Tycorun Energy.

[13] Reducing Reliance on Cobalt for Lithium-ion Batteries | Department of Energy.

[14] Tesla switches all standard-range vehicles to LiFePo chemistry | Roadshow.

[15] The Most Abundant Elements In The Earth's Crust | WorldAtlas.

[16] There's a Fortune to Be Made in the Obscure Metals Behind Clean Power | Bloomberg.

[17] Timeline: History of the Electric Car | Department of Energy.

[18] Wholesale Squaric Acid Batches | Alibaba.com.

[19] National Blueprint for Lithium Batteries 2021-2030 | Federal Consortium for Advanced Batteries, Department of Energy. Technical report, 2021.

[20] Global Supply Chains of EV Batteries | International Energy Agency, 2022.

[21] K. M. Abraham. How Comparable Are Sodium-Ion Batteries to Lithium-Ion Counterparts? *ACS Energy Letters*, 5(11):3544–3547, 11 2020.

[22] Shabbir Ahmed, Paul A. Nelson, and Dennis W. Dees. Study of a dry room in a battery manufacturing plant using a process model. *Journal of Power Sources*, 326:490–497, 9 2016.

[23] Burak Aktekin, Guiomar Hernández, Reza Younesi, Daniel Brandell, and Kristina Edström. Concentrated LiFSI–Ethylene Carbonate Electrolytes and Their Compatibility with High-Capacity and High-Voltage Electrodes. *ACS Applied Energy Materials*, 5(1):585–595, 1 2022.

[24] Seong Jin An, Jianlin Li, Claus Daniel, Debasish Mohanty, Shrikant Nagpure, and David L. Wood. The state of understanding of the lithium-ion-battery graphite solid electrolyte interphase (SEI) and its relationship to formation cycling. *Carbon*, 105:52–76, 8 2016.

[25] Doron Aurbach and Yair Cohen. The Application of Atomic Force Microscopy for the Study of Li Deposition Processes. *Journal of The Electrochemical Society*, 143(11):3525–3532, 11 1996.

[26] Heather M. Barkholtz, Yuliya Preger, Sergei Ivanov, Jill Langendorf, Loraine Torres-Castro, Joshua Lamb, Babu Chalamala, and Summer R. Ferreira. Multiscale thermal stability study of commercial lithium-ion batteries as a function of cathode chemistry and state-of-charge. *Journal of Power Sources*, 435:226777, 9 2019.

[27] O. V. Bushkova, T. V. Yaroslavtseva, and Yu. A. Dobrovolsky. New lithium salts in electrolytes for lithium-ion batteries (Review). *Russian Journal of Electrochemistry 2017 53:7*, 53(7):677–699, 8 2017.

[28] Zachary P. Cano, Dustin Banham, Siyu Ye, Andreas Hintennach, Jun Lu, Michael Fowler, and Zhongwei Chen. Batteries and fuel cells for emerging electric vehicle markets. *Nature Energy 2018 3:4*, 3(4):279–289, 4 2018.

[29] Xin-Bing Cheng, Rui Zhang, Chen-Zi Zhao, Fei Wei, Ji-Guang Zhang, and Qiang Zhang. A Review of Solid Electrolyte Interphases on Lithium Metal Anode. *Advanced Science*, 3(3):1500213, 3 2016.

[30] Woonghee Choi, Se-Ryen Park, and Chan Hyoung Kang. Characteristics of Ni1/3Co1/3Mn1/3(OH)2 Powders Prepared by Co-Precipitation in Air and Nitrogen Atmospheres. *Journal of Korean Powder Metallurgy Institute*, 23(2):136–142, 4 2016.

[31] Dan Doughty and E. Peter Roth. A general discussion of Li Ion battery safety. *Electrochemical Society Interface*, 21(2):37–44, 1 2012.

[32] F. Duffner, M. Wentker, M. Greenwood, and J. Leker. Battery cost modeling: A review and directions for future research. *Renewable and Sustainable Energy Reviews*, 127:109872, 7 2020.

[33] Victor Duffort, Elahe Talaie, Robert Black, and Linda F. Nazar. Uptake of CO2 in Layered P2-Na0.67Mn0.5Fe0.5O2: Insertion of carbonate anions. *Chemistry of Materials*, 27(7):2515–2524, 4 2015.

[34] Christian Ekberg and Martina Petranikova. Lithium Batteries Recycling. *Lithium Process Chemistry: Resources, Extraction, Batteries, and Recycling*, pages 233–267, 1 2015.

[35] Naoki Futamura, Takayuki Ichikawa, Nobuyuki Imanishi, Yasuo Takeda, and Osamu Yamamoto. Lithium Nitride Formation on Lithium Metal. *ECS Meeting Abstracts*, MA2012-02(11):1137, 6 2012.

[36] John B. Goodenough and Youngsik Kim. Challenges for rechargeable Li batteries. *Chemistry of Materials*, 22(3):587–603, 2 2010.

[37] M. H. Han, N. Sharma, E. Gonzalo, J. C. Pramudita, H. E.A. Brand, J. M. López Del Amo, and T. Rojo. Moisture exposed layered oxide electrodes as Na-ion battery cathodes. *Journal of Materials Chemistry A*, 4(48):18963–18975, 12 2016.

[38] Gustavo M. Hobold, Jeffrey Lopez, Rui Guo, Nicolò Minafra, Abhik Banerjee, Y. Shirley Meng, Yang Shao-Horn, and Betar M. Gallant. Moving beyond 99.9% Coulombic efficiency for lithium anodes in liquid electrolytes. *Nature Energy 2021 6:10*, 6(10):951–960, 10 2021.

[39] Junxian Hou, Languang Lu, Li Wang, Atsushi Ohma, Dongsheng Ren, Xuning Feng, Yan Li, Yalun Li, Issei Ootani, Xuebing Han, Weining Ren, Xiangming He, Yoshiaki Nitta, and Minggao Ouyang. Thermal runaway of Lithium-ion batteries employing LiN(SO2F)2-based concentrated electrolytes. *Nature Communications 2020 11:1*, 11(1):1–11, 10 2020.

[40] Man Huon Han, Begoña Acebedo, Elena Gonzalo, Paula Sánchez Fontecoba, Skye Clarke, Damien Saurel, and Teófilo Rojo. Synthesis and Electrochemistry Study of P2-and O3-phase Na 2/3 Fe 1/2 Mn 1/2 O 2 The successful phase separation of P2-and O3-phase Na. 2015.

[41] D.W. Jeppson, J.L. Ballif, W.W. Yuan, and B.E. Chou. Lithium literature review: lithium's properties and interactions. *Hanford Engineering Development Lab., Richland, WA*, 4 1978.

[42] Shipeng Jia, Jonathan Counsell, Michel Adamič, Antranik Jonderian, and Eric McCalla. High-throughput design of Na–Fe–Mn–O cathodes for Na-ion batteries. *Journal of Materials Chemistry A*, 10(1):251–265, 12 2021.

[43] M. M. Kabir and Dervis Emre Demirocak. Degradation mechanisms in Li-ion batteries: a state-of-the-art review. *International Journal of Energy Research*, 41(14):1963–1986, 11 2017.

[44] Sujith Kalluri, Kuok Hau Seng, Wei Kong Pang, Zaiping Guo, Zhixin Chen, Hua Kun Liu, and Shi Xue Dou. Electrospun P2-type Na2/3(Fe1/2Mn1/2) O2 hierarchical nanofibers as cathode material for sodium-ion batteries. *ACS Applied Materials and Interfaces*, 6(12):8953–8958, 6 2014.

[45] Knehr and Kevin W. A Manual for BatPaC v5.0 Battery Performance and Cost Modeling for Electric-Drive Vehicles.

[46] M. H. Lee, Y. J. Kang, S. T. Myung, and Y. K. Sun. Synthetic optimization of Li[Ni1/3Co1/3Mn1/3]O2 via co-precipitation. *Electrochimica Acta*, 50(4):939–948, 12 2004.

[47] Kai Liu, Yayuan Liu, Dingchang Lin, Allen Pei, and Yi Cui. Materials for lithium-ion battery safety. *Science Advances*, 4(6), 6 2018.

[48] Xiang Liu, Dongsheng Ren, Hungjen Hsu, Xuning Feng, Gui Liang Xu, Minghao Zhuang, Han Gao, Languang Lu, Xuebing Han, Zhengyu Chu, Jianqiu Li, Xiangming He, Khalil Amine, and Minggao Ouyang. Thermal Runaway of Lithium-Ion Batteries without Internal Short Circuit. *Joule*, 2(10):2047–2064, 10 2018.

[49] E. R. Logan, A. Eldesoky, E. Eastwood, H. Hebecker, C. P. Aiken, M. Metzger, and J. R. Dahn. The Use of LiFSI and LiTFSI in LiFePO4/Graphite Pouch Cells to Improve High-Temperature Lifetime. *Journal of The Electrochemical Society*, 169(4):040560, 4 2022.

[50] Jaione Martínez De Ilarduya, L. Otaegui, Montserrat Galcerán, L. Acebo, Devaraj Shanmukaraj, Teófilo Rojo, and Michel Armand. Towards high energy density, low cost and safe Na-ion full-cell using P2–Na0.67[Fe0.5Mn0.5]O2 and Na2C4O4 sacrificial salt. *Electrochimica Acta*, 321:134693, 10 2019.

[51] Jaione Martinez De Ilarduya, Laida Otaegui, Juan Miguel López del Amo, Michel Armand, and Gurpreet Singh. NaN3 addition, a strategy to overcome the problem of sodium deficiency in P2-Na0.67[Fe0.5Mn0.5]O2 cathode for sodium-ion battery. *Journal of Power Sources*, 337:197–203, 1 2017.

[52] A. Mauger, C. M. Julien, A. Paolella, M. Armand, and K. Zaghib. A comprehensive review of lithium salts and beyond for rechargeable batteries: Progress and perspectives. *Materials Science and Engineering: R: Reports*, 134:1–21, 12 2018.

[53] Joseph D. Menczel and R. Bruce Prime. Thermal Analysis of Polymers: Fundamentals and Applications. *Thermal Analysis of Polymers: Fundamentals and Applications*, pages 1–688, 7 2008.

[54] Björn Nykvist and Måns Nilsson. Rapidly falling costs of battery packs for electric vehicles. *Nature Climate Change 2014 5:4*, 5(4):329–332, 3 2015.

[55] M. N. Obrovac, Leif Christensen, Dinh Ba Le, and J. R. Dahn. Alloy Design for Lithium-Ion Battery Anodes. *Journal of The Electrochemical Society*, 154(9):A849, 2007.

[56] Myung Hyun Ryou, Je Nam Lee, Dong Jin Lee, Wan Keun Kim, You Kyeong Jeong, Jang Wook Choi, Jung Ki Park, and Yong Min Lee. Effects of lithium salts on thermal stabilities of lithium alkyl carbonates in SEI layer. *Electrochimica Acta*, 83, 2012.

[57] Richard Schmuch, Ralf Wagner, Gerhard Hörpel, Tobias Placke, and Martin Winter. Performance and cost of materials for lithium-based rechargeable automotive batteries. *Nature Energy 2018 3:4*, 3(4):267–278, 4 2018.

[58] Lei Shi, Tao Qu, Dachun Liu, Yong Deng, Bin Yang, and Yongnian Dai. Process of Thermal Decomposition of Lithium Carbonate. *Minerals, Metals and Materials Series*, pages 107–116, 2020.

[59] Gurpreet Singh, Begoña Acebedo, Montse Casas Cabanas, Devaraj Shanmukaraj, Michel Armand, and Teófilo Rojo. An approach to overcome first cycle irreversible capacity in P2-Na2/3[Fe1/2Mn1/2]O2. *Electrochemistry Communications*, 37:61–63, 12 2013.

[60] Paul Stenquist. Hurdle to Broad Adoption of E.V.s: The Misperception They're Unsafe, 2023.

[61] Christoph Vaalma, Daniel Buchholz, Marcel Weil, and Stefano Passerini. A cost and resource analysis of sodium-ion batteries. *Nature Reviews Materials 2018 3:4*, 3(4):1–11, 3 2018.

[62] Pallavi Verma, Pascal Maire, and Petr Novák. A review of the features and analyses of the solid electrolyte interphase in Li-ion batteries. *Electrochimica Acta*, 55(22):6332–6341, 9 2010.

[63] Marc Wentker, Matthew Greenwood, and Jens Leker. A Bottom-Up Approach to Lithium-Ion Battery Cost Modeling with a Focus on Cathode Active Materials. *Energies 2019, Vol. 12, Page 504*, 12(3):504, 2 2019.

[64] Naoaki Yabuuchi, Masataka Kajiyama, Junichi Iwatate, Heisuke Nishikawa, Shuji Hitomi, Ryoichi Okuyama, Ryo Usui, Yasuhiro Yamada, and Shinichi Komaba. P2-type Nax[Fe1/2Mn1/2]O2 made from earth-abundant elements for rechargeable Na batteries. *Nature Materials 2012 11:6*, 11(6):512–517, 4 2012.

[65] Shotaro Yamaguchi, Takayuki Ichikawa, Yongming Wang, Yuki Nakagawa, Shigehito Isobe, Yoshitsugu Kojima, and Hiroki Miyaoka. Nitrogen Dissociation via Reaction with Lithium Alloys. *ACS Omega*, 2(3):1081–1088, 3 2017.

[66] Hui Yang, Guorong V. Zhuang, and Philip N. Ross. Thermal stability of LiPF6 salt and Li-ion battery electrolytes containing LiPF6. *Journal of Power Sources*, 161(1), 2006.

[67] Ziqi Zeng, Vijayakumar Murugesan, Kee Sung Han, Xiaoyu Jiang, Yuliang Cao, Lifen Xiao, Xinping Ai, Hanxi Yang, Ji Guang Zhang, Maria L. Sushko, and Jun Liu. Non-flammable electrolytes with high salt-to-solvent ratios for Li-ion and Li-metal batteries. *Nature Energy 2018 3:8*, 3(8):674–681, 7 2018.

[68] Liwei Zhao, Izumi Watanabe, Takayuki Doi, Shigeto Okada, and Jun ichi Yamaki. TG-MS analysis of solid electrolyte interphase (SEI) on graphite negative-electrode in lithium-ion batteries. *Journal of Power Sources*, 161(2):1275–1280, 10 2006.

[69] Mingxian Zhou, Bang Li, Jia Li, and Zhenming Xu. Pyrometallurgical Technology in the Recycling of a Spent Lithium Ion Battery: Evolution and the Challenge. *ACS ES&T Engineering*, 1(10):1369–1382, 10 2021.

[70] Yan Zhou, David Gohlke, Luke Rush, Jarod Kelly, and Qiang Dai. Lithium-Ion Battery Supply Chain for E-Drive Vehicles in the United States: 2010–2020. 3 2021.

[71] Micah S. Ziegler, Juhyun Song, and Jessika E. Trancik. Determinants of lithium-ion battery technology cost decline. *Energy & Environmental Science*, 14(12):6074–6098, 12 2021.

[72] Micah S. Ziegler and Jessika E. Trancik. Re-examining rates of lithium-ion battery technology improvement and cost decline. *Energy & Environmental Science*, 14(4):1635–1651, 4 2021.

[73] Wenhua Zuo, Alessandro Innocenti, Maider Zarrabeitia, Dominic Bresser, Yong Yang, and Stefano Passerini. Layered Oxide Cathodes for Sodium-Ion Batteries: Storage Mechanism, Electrochemistry, and Techno-economics. *Accounts of Chemical Research*, 56(3):284–296, 2 2023.